Graphene and beyond:
Electron transport in two dimensional materials

by

Kyunghoon Lee

A dissertation submitted in partial fulfillment
of the requirements for the degree of
Doctor of Philosophy
(Electrical Engineering)
in The University of Michigan
2015

Doctoral Committee:

Associate Professor Zhaohui Zhong, Chair
Professor Jay L. Guo
Professor Cagliyan Kurdak
Associate Professor Wei Lu

To my family, friends, and above all, my Lord who works in all things for the good.

Acknowledgements

First and foremost, I would like to thank my advisor Prof. Zhaohui Zhong. During my graduate years, I have learned a lot from Prof. Zhaohui Zhong: in particular, his enthusiasm and creativity, and openness are all that I aspire to in research field. Also, thanks for the freedom to explore what I wanted by encouraging me not to give up with patience and perseverance, and to pursue the goal with focusing on relevant experiments. I also admire his ability to shape a very good group with a very informal atmosphere, which made my learning process pleasant and enjoyable.

I would also like to thank my thesis committee members, Prof. Wei Lu, Prof. Jay Guo, and in particular Prof. Cagliyan Kurdak for helpful and insightful discussions and advises. Many hours of discussions with him has largely shaped me as a scientist and engineer, and made me understand how to approach physics problems on my own, to a certain extent. I should also thank Prof. Leonid Levitov at MIT, including Justin Song. Thank you, Prof. Leonid Levitov for taking time to look at my data and giving me an insightful idea for further analysis.

My sincere appreciation is extended to past and present Zhong lab members, Dr. Nanditha Dissanayake, Dr. Chung Chiang Wu, Dr. Seunghyun Lee, Dr. Chang-Hua Liu, Dr. Girish Kulkarni, Che-Hung Liu, Kang Li, Rui Li, Amlan Nayak, and Wenzhe Zang. I also would like to extend my gratitude to those graduate students whose assistance I greatly appreciate, Yun Suk Eo, Dr. Sunghyun Jo, Dr. Junseok Heo, Dr. Hyun Kum, Dr. Jinyoung Hwang, Dr. Shinhyun Choi, Dr. Gwang Hyeon Baek, Dr. Kyusang Lee, Jihyun Cho, Dr. Seokjun Park, and Dr. Siddartha Gaba.

The work described in this thesis would not have been complete without the kind and patient support of the staff at Lurie Nanofabrication Facility. I deeply appreciate their support and help including Timothy Brock, Gregory Allion, Russ Clifford, Pilar Herrera-Fierro, Sandrine Martin, Matthew Oonk, Vishva Ray, and Nadine Wang.

There are also many people who particularly contributed to my happiness during my time here. Specifically, many thanks to KPCAA church members for the great memories we shared in Ann Arbor, including Pastor Sunmyung Lyu, Pastor Jae Joong Hwang, Dr. Woonghee Lee, Dr. Sangjo Choi, Dongil Kang, Dr. Jihun Kim, Dr. Suk-joon Hyung, Dr. MinChul Shin, and graduate and undergraduate worship members as well as Cherokee Mission team members. Especially, I would like to thank to Dr. Dae Yon Jung, Dr. Kihyuk Sohn, and the members of our football club, "A.K. United", for sharing special moments at many competitions.

Finally, I would like to thank my family for their constant support by prayer and encouragement. In addition, I gratefully acknowledge the financial support from Kwanjeong Educational Foundation for my scientific career.

TABLE OF CONTENTS

LIST OF FIGURES

LIST OF APPENDICES

Appendix

Abstract

Owing to their unique energy band structure and the ease of material synthesis, two dimensional nanomaterials, such as graphene, have become the ideal platform for observing novel electron transport phenomena in reduced dimensions. In particular, low-energy quasiparticles in monolayer graphene behave like massless Dirac fermions, which have led to observations of many interesting phenomena, including Klein tunneling, anomalous Quantum Hall effect, etc. In contrast to the monolayer graphene, quasiparticles in bilayer graphene (BLG) are massive chiral fermions due to its parabolic band structure. Thus, BLG also gives a number of intriguing properties which are very different from those of monolayer graphene, including tunable band gap opening and anti-Klein tunneling, arising from chiral characteristics of charge carriers. However, unlike SLG, experimental works on chiral electron transport in BLG have received less attention.

In addition, other two-dimensional atomic layer crystals, such as atomically thin layered transition-metal-dichalcogenides (TMDCs), are also attractive material platform with unique electronic and optical properties, including indirect to direct band gap transition, and valley polarized carrier transport. However, study of the low temperature electron transport in atomic thin layered TMDCs is still in its infancy. One of the major hurdles for electron transport study lies in the large metal/semiconductor junction barrier for carrier injection, which leads to the contact resistance dominated charge transport in short channel nanoscale devices.

In this thesis, I first demonstrated the successful synthesis of wafer scale BLG with high homogeneity by low-pressure chemical vapor deposition (CVD). The bilayer nature of the graphene films were confirmed through a series of characterizations including Raman Spectroscopy, Transmission Electron Microscope, and electrical transports showing field induced bandgap opening. Next, I proceeded to study the importance of chiral electron transport in BLG. I observed electronic cloaking effect with anti-Klein effect as a manifestation of chirality by probing phase coherent transport behavior in CVD bilayer graphene nanostructure. Finally, I studied the electron transport in few-layer TMDCs. I successfully fabricated monolayer MoS_2 single electron transistors using low work function metal for the contact electrodes, and observed Coulomb blockade phenomena attributed to single electron charging on a fairly clean quantum dot.

Chapter 1. Introduction

1.1 Introduction to carbon based nanostructure

1.1.1 Carbon – Carbon bonding

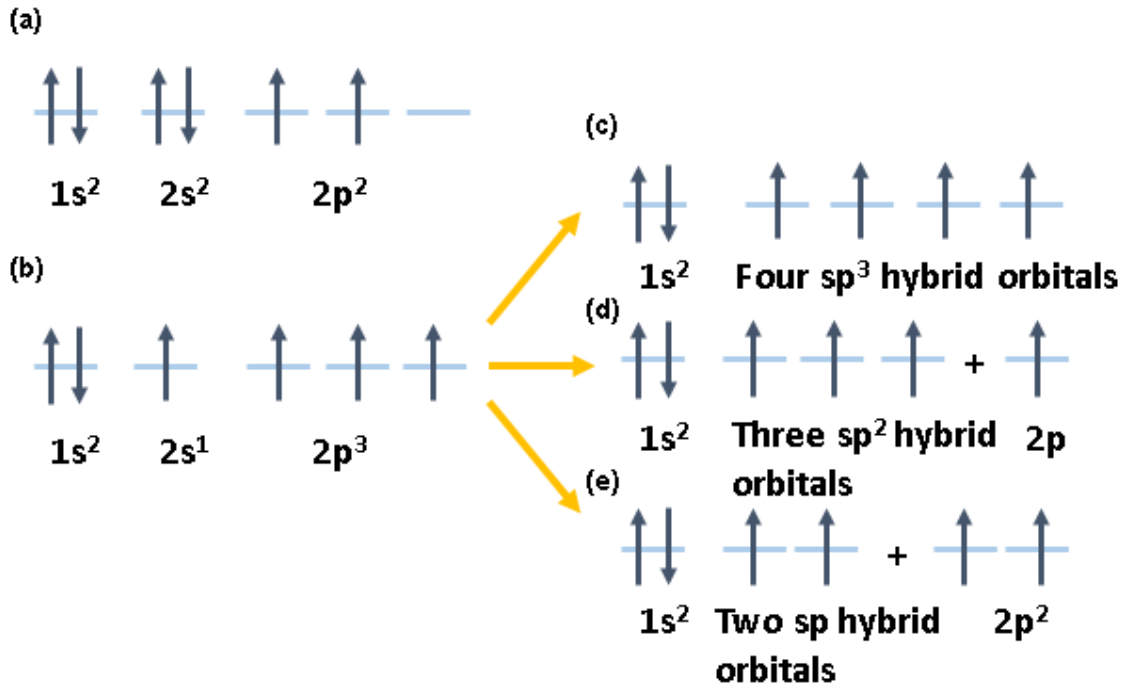

Figure 1.1 Electronic configurations of carbon (a) ground state (b) excited state (c) sp^3 hybridization (d) sp^2 hybridization (e) sp hybridization

Carbon is one of the most versatile elements in the periodic table. Carbon forms more compounds than any other material, due to the types of bonds it may form (single, double, and triple bonds) and the number of different elements it can bond with.

A Carbon atom in its ground state has a $1s^2 2s^2 2p^2$ electronic configuration, having six total electrons. The $1s^2$ orbital possesses two electrons, called core electrons, which are

not available for chemical bonding. Four valence electrons, in 2s and 2p orbitals, are weakly bounded such that they can participate in bond formation. From its ground state configuration, two unpaired electrons are present in its p orbitals. Thus, carbon should theoretically form two bonds, but that is definitely not the case (10).

Since the energy difference between the upper 2p energy level and the lower 2s level is small compared with the binding energy, carbon will rearrange its configuration of valence electrons to decrease the system energy. In this way, the wave function of four valence electrons can readily mix with each other, and such a rearrangement of electron configurations is called hybridization. In carbon, three possible hybridizations may occur: four sp^3 orbitals (one 2s orbital + three 2p orbitals), three sp^2 orbitals (one 2s orbital + two 2p orbitals), and two sp orbitals (one 2s orbital + one 2p orbital) (*9*).

Four sp^3 hybrid orbitals optimize their position in space, forming four σ bonds with neighboring carbons, with an angle of 109.5°. Methane, CH4, is a simple example of sp^3 hybridization through its tetragonal bonding to the four nearest hydrogen atoms. Diamond is a 3-dimensional carbon allotrope, with all carbon atoms in the sp^3 hybridization and connected by σ bonding.

Three sp^2 hybrid orbitals, consisting in mixing three orbitals, arrange themselves to lower the system energy, having an angle of 120° between each orbital with σ bonding. All σ bonds are in the same plane, and there is a remaining p-type orbital perpendicular to this plane. Hence, unmixed p orbitals will form π bonding between carbon atoms. An example of sp^2 hybridization is Ethylene, C_2H_4. Graphite is another 3-dimensional crystal made of stacked layers that is an example of having sp^2 hybridized carbon atoms.

Two sp hybrid orbitals is the last possible hybridization scheme. In such a configuration, σ bonds form from sp orbitals, with an angle of 180°, and π bonds from unmixed p orbitals between carbon atoms, resulting in carbon-carbon triple bond (one σ bond and two π bonds). Acetylene exemplifies such a configuration.

1.2 Graphene

1.2.1 Atomic structure of graphene

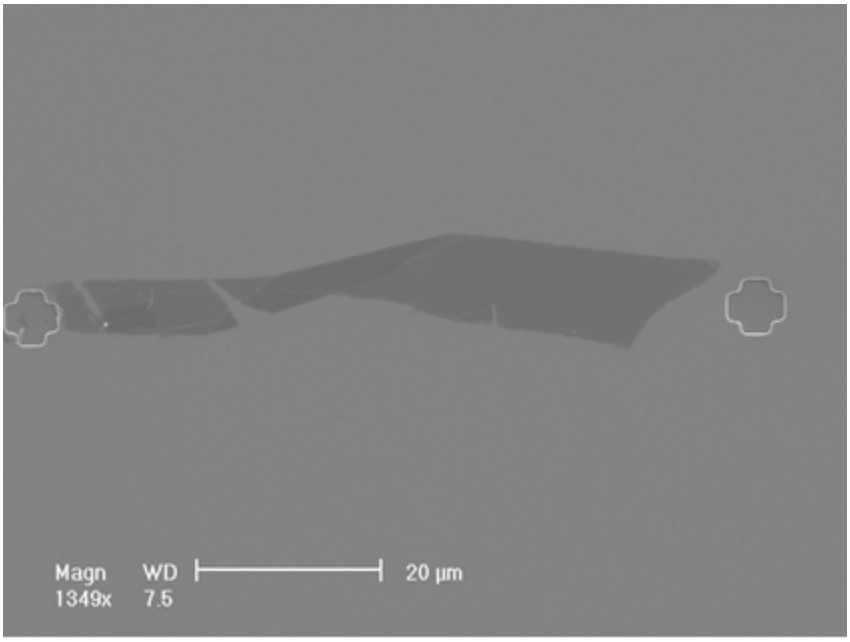

Figure 1.2 SEM image of exfoliated monolayer graphene: brighter region corresponding to monolayer, and dark region corresponding to folded monolayer graphene.

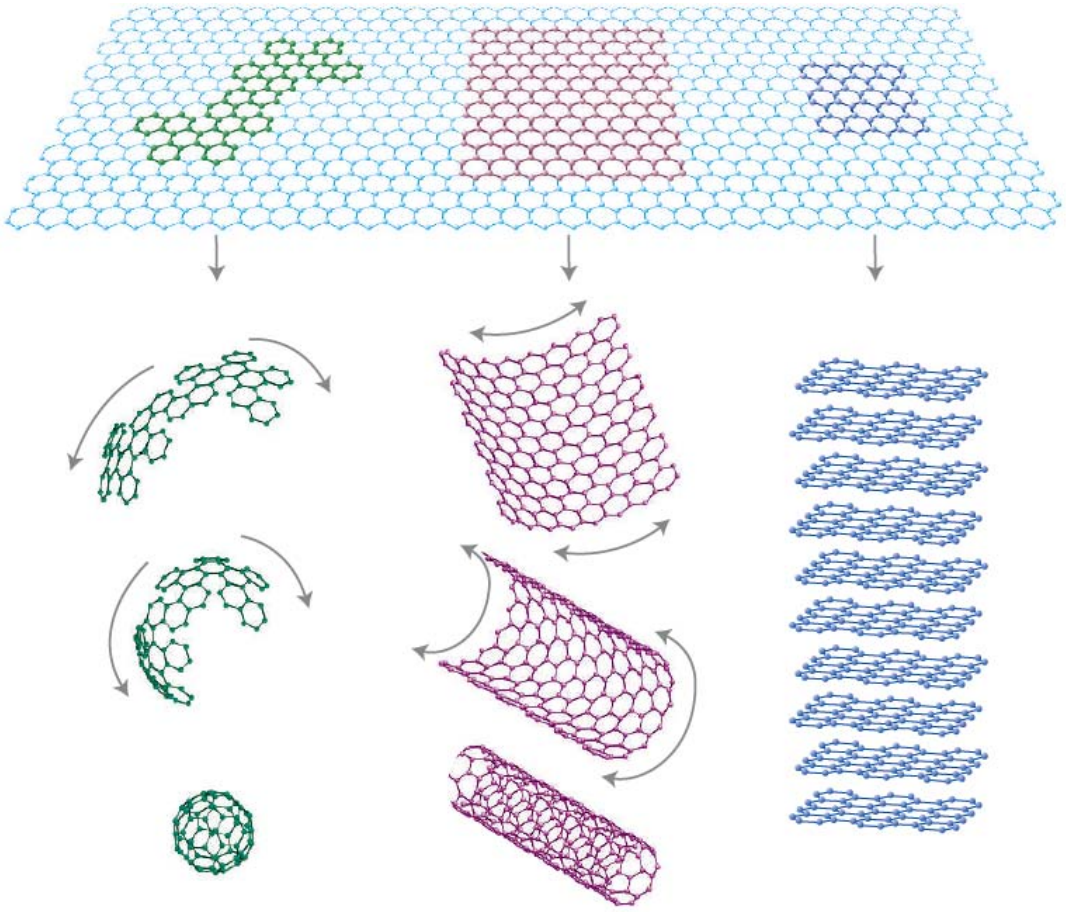

Figure 1.3 Graphene can be wrapped up into 0D-buckyball, rolled into 1D-carbon nanotube, or stacked into 3D-graphite Adopted from (1).

The sp^2 carbon-based family has a great variety of allotropes, from 0-dimensional fullerenes (C60), 1-dimensional carbon-nanotubes, and 2-dimensional graphene, to 3-dimensional stacked substantial number of layers of graphene, called graphite.

Graphene, a single, one-atom thick sheet of carbon atoms arranged in a honeycomb lattice, is a building block of all forms of carbon materials. It can be stacked into 3D graphite, rolled into 1D-carbon-nanotube, or wrapped into 0-D buckyballs (C60).

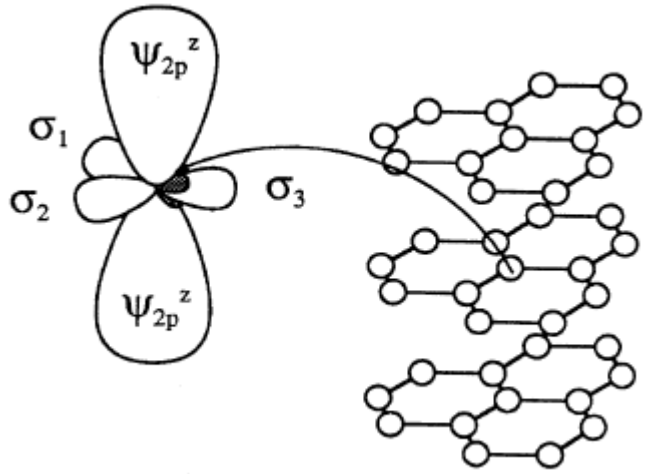

Figure 1.4 Representation of P_z orbitals: the three hybridized σ orbitals and non-hybridized π orbital. Adopted from (*2*).

The 2s orbital and two in-plane $2p_x$, $2p_y$ orbitals are tied up in graphene's strong covalent σ bond, and do not contribute to conductivity of graphene. The remaining $2p_z$ orbital, out of the plane of graphene, is odd under inversion in the plane, and hybridizes to form π (valence) and π* (conduction) bands. The sp^2 hybridized states (σ states) form occupied and unoccupied empty bands with large gap (>12eV at Γ) whereas π states form a single band, closer to Fermi energy because they participate less in bonding. In general, electrons and holes near Fermi energy level have easy access to occupied or unoccupied states. Thus, the π orbitals in graphene are responsible for electrical transport properties by forming delocalized states.

1.2.2 Monolayer graphene band structure

A tight binding calculation for the π electrons provides crucial insight into understanding the electronic structure of the sp^2 carbon-based family: carbon-nanotube, graphene, and graphite, etc.

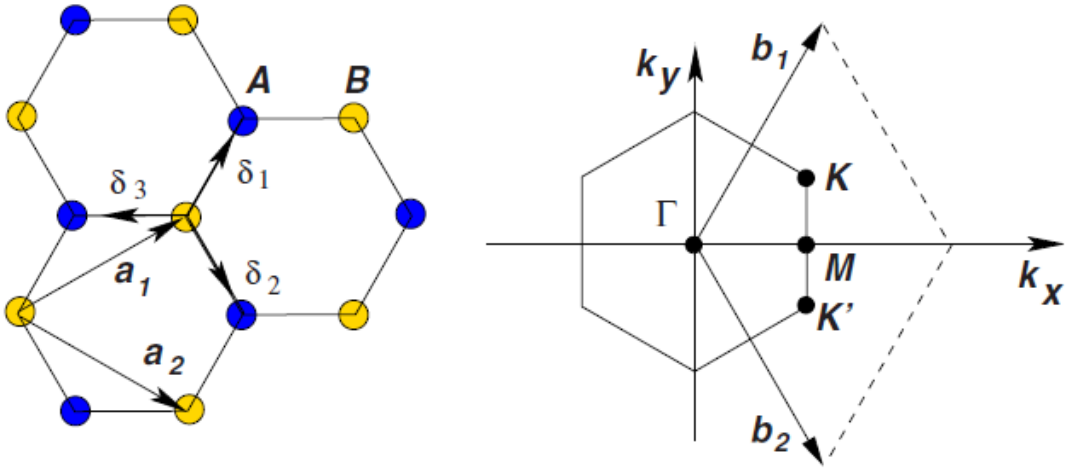

Figure 1.5 (Left) A honeycomb lattice, sublattice A and B are shown as blue and yellow color. (Right) corresponding Brillouin zone. Dirac cones are located at K and K' points. adopted from (3).

The honeycomb lattice contains two atoms per unit cell (A and B) and basis vector (a1, a2):

$$a1 = a\left(\frac{3}{2}, \frac{\sqrt{3}}{2}\right),\ a2 = a\left(\frac{3}{2}, -\frac{\sqrt{3}}{2}\right) \qquad \textit{Equation 1-1}$$

where $a \approx 1.42$Å is the nearest-neighbor distance.

The high-symmetry points K, K', M in the Brillouin zone are shown next, with wave vectors:

$$K = \left(\frac{2\pi}{3a}, \frac{2\pi}{3\sqrt{3}a}\right),\ K' = \left(\frac{2\pi}{3a}, -\frac{2\pi}{3\sqrt{3}a}\right),\ M = \left(\frac{2\pi}{3a}, 0\right). \qquad \textit{Equation 1-2}$$

As a result of two atoms in a unit cell, the tight-binding Hamiltonian can be written as a 2×2 matrix. The basis of electron states consist of two π states from two sublattice

atoms A and B. In the simplest approximation, we only consider nearest-neighbor interactions, with hopping parameter *t*; no hopping process exists within the same sublattices.

$$\mathcal{H}(\vec{k}) = \begin{pmatrix} 0 & tS(\vec{k}) \\ tS^*(\vec{k}) & 0 \end{pmatrix} \qquad \textit{Equation 1-3}$$

where $\vec{k}$ is the wave-vector and the nearest neighbor-vectors are

$$R1 = a\left(\frac{1}{2}, \frac{\sqrt{3}}{2}\right),\ R2 = a\left(\frac{1}{2}, -\frac{\sqrt{3}}{2}\right),\quad R3 = a(-1, 0) \qquad \textit{Equation 1-4}$$

$$S(\vec{k}) = \sum_{\vec{R}} e^{i\vec{k}*\vec{R}} = 2\,exp\left(\frac{ik_x a}{2}\right) cos\left(\frac{k_y a\sqrt{3}}{2}\right) + exp(-ik_x a)$$

Equation 1-5

Hence, the energy is $\mathrm{E}(\vec{k}) = \pm t|S(\vec{k})|$, where $\pm$ denotes the conduction and valence bands, respectively. The resulting band structure shows that band crossing occurs at the high-symmetry point at K, and K', such that $S(\vec{K}) = S\left(\overrightarrow{K'}\right) = 0$.

By expanding the Hamiltonian near K and K' points, the effective Hamiltonian has the form

$$\mathcal{H}_{K,K'}(\vec{k}) = \hbar v_F \begin{pmatrix} 0 & k_x \mp ik_y \\ k_x \pm ik_y & 0 \end{pmatrix} = v_F(p_x\sigma_x + p_y\sigma_y) \qquad \textit{Equation 1-6}$$

In more compact form:

$$\mathcal{H}_K(\vec{k}) = v_F\vec{\boldsymbol{\sigma}} \cdot \boldsymbol{p}; \qquad \mathcal{H}_K(\vec{k}) = \mathcal{H}^t_{K'}(\vec{k}) \qquad \textit{Equation 1-7}$$

where the Pauli matrices are defined as

$$\sigma_x = \begin{pmatrix} 0 & 1 \\ 1 & 0 \end{pmatrix},\ \sigma_y = \begin{pmatrix} 0 & -i \\ i & 0 \end{pmatrix},\ \sigma_z = \begin{pmatrix} 1 & 0 \\ 0 & -1 \end{pmatrix} \qquad \textit{Equation 1-8}$$

Therefore, at around Dirac points, the dispersion is approximately linear. Thus, graphene has a high degree of electron-hole symmetry.

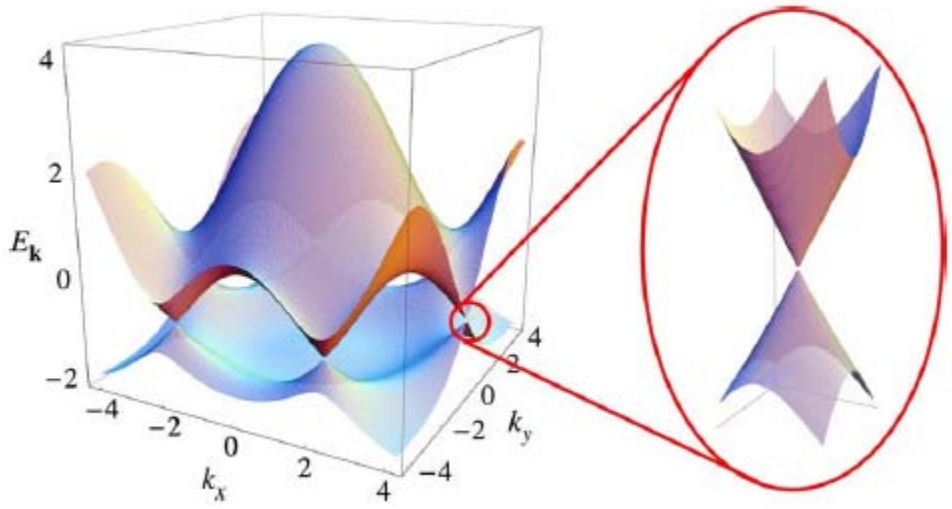

Figure 1.6 Electronic dispersion of graphene in honeycomb lattice (Right) Conical band spectrum at K point. Adopted from (3).

1.2.3 Bilayer graphene band structure

By exfoliation of graphite, one can obtain two layers of carbon atoms with bernal stacking order (*3, 11-13*). In bilayer graphene, carbon atoms are arranged in two honeycomb lattices, according to Bernal stacking order (A1-B2), where A and B refer to the sublattice within each layer shown in Fig 1.7.

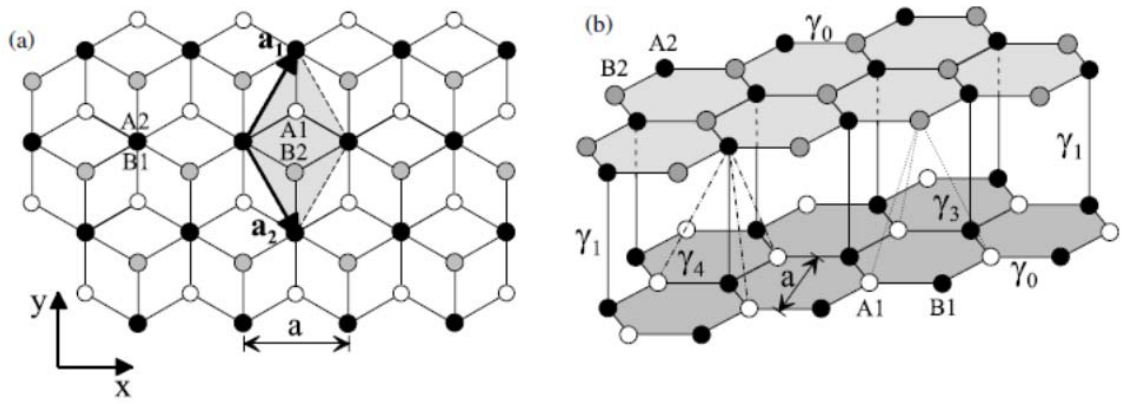

Figure 1.7 Plain and side view of bilayer graphene crystal structure. A1 and B1 atoms in bottom layer are color coded with white and black. A2and B2 in top layer are colored with black and grey, respectively. γ_0 , γ_1 , γ_3 , γ_4 are the hopping parameters. Adopted from (*4*).

The electronic structure of bilayer graphene can be understood by a tight-binding model. The set of hopping parameters are in-plane hopping parameters, $\gamma_{A1B1} = \gamma_{A2B2} \equiv \gamma_0$, which lead to the in-plane velocity v = $\left(\frac{\sqrt{3}}{2}\right) a\gamma_0/\hbar$), where a is a lattice constant, strongest inter-layer coupling, $\gamma_{A2B1} \equiv \gamma_1$, between pairs of A2-B1 orbitals. Such strong coupling produces dimers, leading to high-energy band formation. Weaker A1-B2 coupling $\gamma_{A1B2} \equiv \gamma_3$ exists also (*14*).

The simplest model described by Hamiltonian for bilayer graphene is in the vicinity of K point, to the basis of wave function, $\psi = (\varphi_{A1}, \varphi_{B2}, \varphi_{A2}, \varphi_{B1})$,

$$\mathcal{H}_K(\vec{k}) = \begin{pmatrix} 0 & 0 & 0 & v\pi^+ \\ 0 & 0 & v\pi & 0 \\ 0 & v\pi^+ & 0 & \gamma_1 \\ v\pi & 0 & \gamma_1 & 0 \end{pmatrix} \qquad \textit{Equation 1-9}$$

where $\pi = p_x + ip_y$, v is Fermi velocity.

It is possible to obtain a low-energy Hamiltonian that describes the effective hopping between non-dimer sites, A1-B2, where carbon atoms do not directly lie below

and above, and are not strongly coupled. By eliminating dimer-state component, $\varphi_{A2}, \varphi_{B1}$, we can construct an effective Hamiltonian for hopping between A1-B2 atom sites (*14*).

$$\mathcal{H}_K(\vec{k}) = \frac{-1}{2m^*}\begin{pmatrix} 0 & (\pi^+)^2 \\ \pi^2 & 0 \end{pmatrix} \qquad \textit{Equation 1-10}$$

where $m^* = \gamma_1/2v^2$, $\psi = (\varphi_{A1}, \varphi_{B2})$.

This Hamiltonian describes the ways of A1⇆B2 hopping. The hopping process consists of three steps: an intralayer hop from A1 to B1, followed by an interlayer transition from B1 to A2 via dimer states, and finally followed by an intralayer hop from A2 to B2. Two intralayer hopping processes are described by the terms, π^2 and $(\pi^+)^2$ with reflecting energetic cost γ_1 via dimer state transition in the mass term, $m^* = \gamma_1/v^2$.

Thus, the bilayer graphene Hamiltonian, written in a two-component basis, yields a parabolic energy spectrum. This is a new type of Hamiltonian, different both from Schrodinger-type (for non-relativistic carriers), and Dirac-type (for relativistic carriers) Hamiltonians. The limit of the validity for the two band model lies in the condition that two high energy bands are not occupied, with allowed energy, $\epsilon < \frac{1}{4}\gamma_1 \approx 100meV$. We will use this two band energy spectrum throughout this thesis.

1.3 Interesting electronic properties of Graphene

What makes graphene so attractive in condensed matter physics and material science field is mainly due to the similarity of Hamiltonian with that of massless, relativistic particles (*1*). The linear dispersion of graphene, described by the Dirac equation, allows many properties, anticipated in relativistic quantum mechanics (*15*). Consequently, electrons in graphene, having an effective mass of zero, behave more like a photons than electrons in conventional semiconductor materials. Charged massless particles in graphene, called Dirac fermions, move with a constant speed of v_F, 300 times slower than the speed of light. The essential feature of the Dirac spectrum is the fact that electrons and positrons, called holes in solid state physics, are intimately linked by perfect symmetry (*16*). Thus, relativistic particles (electrons) in graphene, by transforming antiparticles (holes) according to the Dirac equation, can penetrate a potential barrier, regardless of its width and height. We will explain this exotic feature, referred as a Klein paradox, in Chapter. 3 with more detailed theory and experiments.

Ever since successful isolation of graphene by an exfoliation method by Geim group, a series of ground-breaking discoveries have been reported relevant to electron transport properties: Ambipolar field effect (*17*) (such that charge carriers can be tuned continuously between electrons and holes), exceptionally high electron mobility up to 10^6 cm^2/Vs in suspended structure at 2K (*18*) and 10^5 cm^2/Vs in BN encapsulated structure at room temperature (*19*) , the long ballistic transport distance (large electronic mean free path) (*19*), the conductivity minimum (*20, 21*) and absence of Anderson localization (*22*), and the chiral quantum Hall effect (*23-25*).

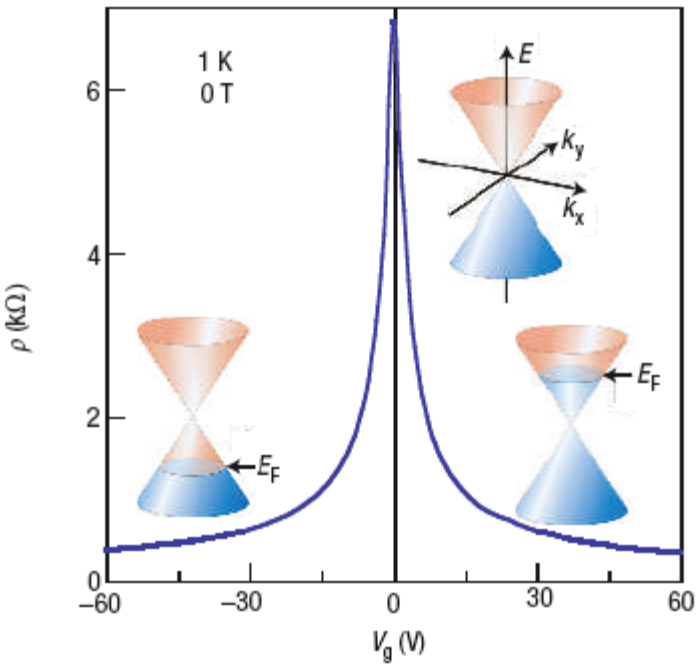

Figure 1.8 Ambipolar characteristics of graphene field effect transistor. The insets show Fermi level energy position in each conical low energy spectrum. Adopted from (1).

In the presence of a perpendicular magnetic field, electrons which experience Lorentz force travel closed circular orbits. In a 2D electron gas, according to quantum theory, those orbits must have a discrete value, an integer multiple of de Brogile wavelength. This condition leads to a discrete electron energy, the so-called Landau level. Thereby, in all clean 2D systems, the conductivity measured perpendicular to the applied current, σ_{xy} is quantized in a series of plateaus having values $\nu e^2/h$, where ν is a filling

factor, defined as the ratio of the number of electrons to the degeneracy (number of available states) of each Landau level (LL).

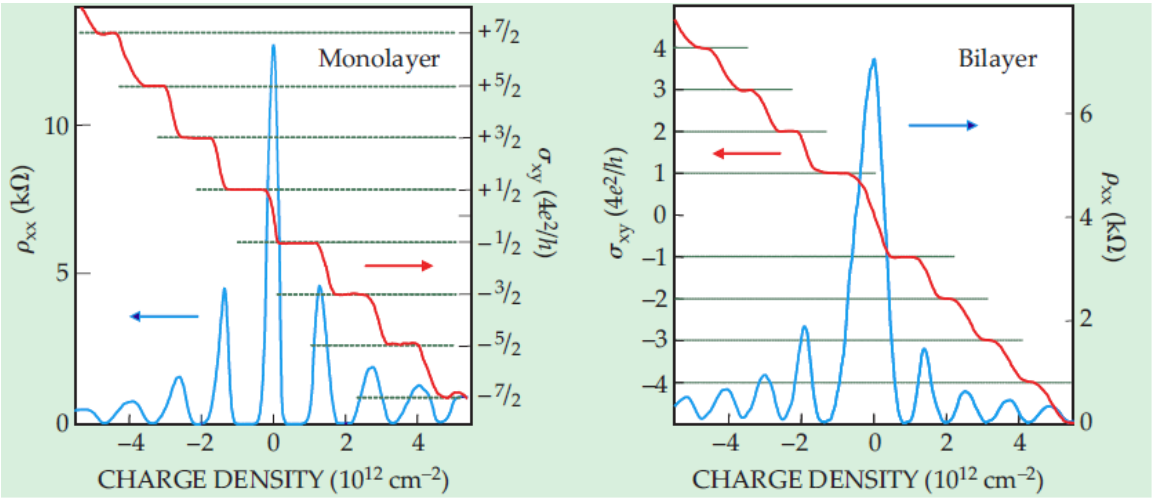

Figure 1.9 Quantum Hall effect in graphene as a function of charge density. (Left) Landau level at zero level is drawn half from the conduction and another half from valence band in single layer graphene. (Right) Double jump at σ_{xy} =0 due to pinned two Landau levels at zero energy in bilayer graphene. Adapted from (1).

The quantum hall effect (QHE) allows one to infer the electronic spectrum by magneto-transport data. The quantized sequence observed in graphene, known as the anomalous quantum hall effect, differs from what would be expected from conventional 2D systems. The quantized sequence in graphene is shifted in comparison with the standard QHE sequence by one half, such that $\sigma_{xy} = \pm 4e^2/h(N + \frac{1}{2})$, where N is LL index, and the factor 4 appears due to spin and valley degeneracies. Electrons in graphene have another internal degree of freedom, referred as a pseudospin, rather than real spin. The 'half-integer' shift arises from the fact that pseudospin rotation introduces π phase shift to the electron wave function as electrons complete an orbit in the magnetic field. This experimental result provides direct evidence of the existence of both massless Dirac fermion and its related Berry phase (*23, 24*).

An even more interesting case is the QHE for bilayer graphene. The standard sequence of Hall plateaus of $\sigma_{xy} = \pm 4e^2N/h$ are measured (*25*); however, the very first plateau at N=0 is missing. This QHE behavior differs from that of the single layer and other 2D systems. The 2π-Berry phase shift to the electrons wave function is responsible for the missing plateau, implying the existence of massive but chiral charge particles. Hence, we will indeed find that this chiral property is crucial for electron transport by probing the results in Chapter 3.

The mobility of electrons in graphene (~200,000cm^2/Vs) (*18*) is significantly higher than that of other widely used semiconductor materials, for example, mobility of silicon approximately as 1400cm^2/Vs. Exceptionally high mobility even in high carrier concentration implies a ballistic transport of electrons over the distance between two electrodes, might be possible as the device size shrinks down to sub-micrometer scale at room temperature (*19*).

Moreover, by utilizing ambipolarity of graphene, just a couple of graphene transistors are needed to perform two quaternary modulation scheme (*26*) in much more simpler circuitry than the silicon based conventional modulator circuits. Graphene transistors operational at up to 300GHz (*27*) were already demonstrated, showing significant advance towards high-frequency electronics. Up until now, graphene based electronics have been developed very rapidly, and considered as one of strong candidates for post-silicon electronics.

1.4 Band-gap of graphene

Despite its unique and extraordinary electronic properties, bandgap of graphene has to be opened to become a viable channel material for transistor applications. The zero-bandgap intrinsic to the graphene limits its potential applications in the semiconductor industry (*28*).

Several elegant approaches have been tested including quasi-one dimensional nanostructure, called graphene-nanoribbon, by inducing carrier confinement to achieve sizable transport gap (200meV) at low temperature (*29, 30*), and bilayer graphene double-gate structure by applying perpendicular electric field to break symmetry of equivalent potential of two layers with bandgap opening up to ~250meV at room temperature (*8, 13, 31, 32*).

Graphene nanoribbon (*5, 30*) sacrifices substantial degradation of mobility due to its carrier confinement structure, and edge roughness. With double gated bilayer graphene, we can tune the bandgap from 0 – 250meV by applying electric field, which is remarkable in itself and shows a potential of bilayer graphene electronics. However, size of bilayer graphene from mechanical cleavage method have been limited to μm^2 scale thus far, and synthesis of wafer scale homogeneous bilayer graphene posts tremendous challenge (*31, 33*). Thus, we will discuss on wafer scale bilayer graphene synthesis with more detailed explanations in Chapter 2.

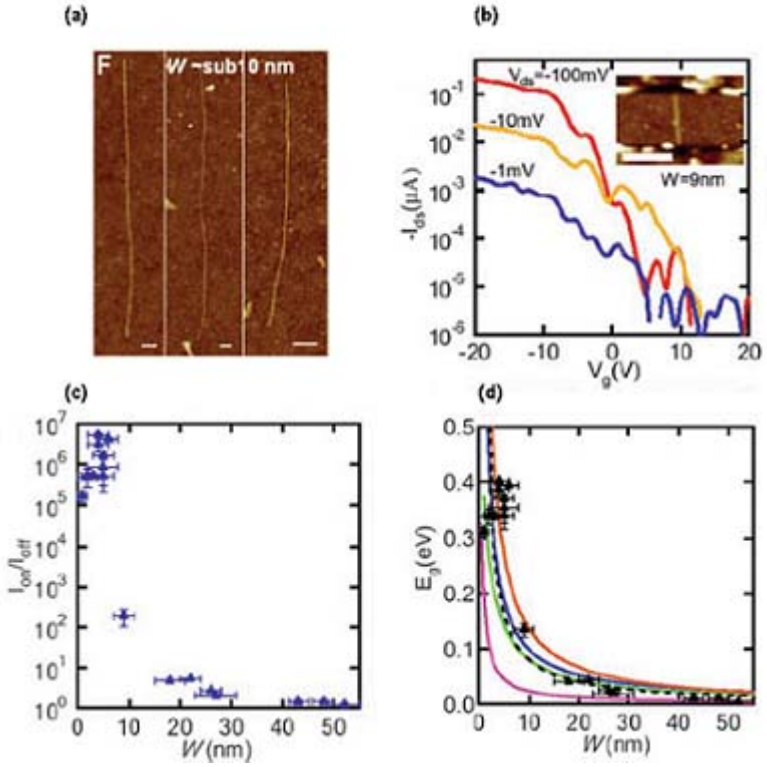

Figure 1.10 (a) sub-10nm chemically driven graphene nanoribbon(GNR) (b) Transfer characteristics of GNR with high on/off ratio (c) on/off current ratio as a function of various GNR width (d) Eg extracted from on/off experimental data for various width W. adopted from (5).

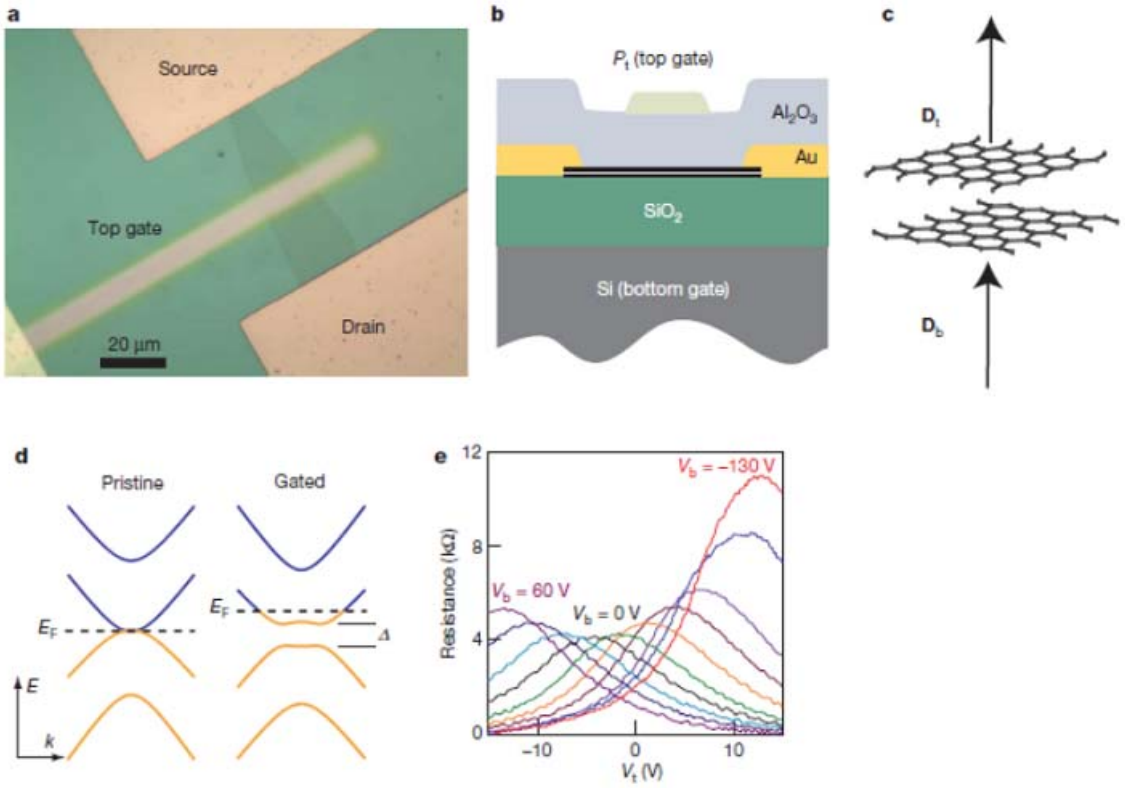

Figure 1.11 (a) Optical microscopy of double gated bilayer graphene. (b) Illustration of cross sectional view. (c)sketch of perpendicular electric field to bilayer graphene plane (d)electronic structure of pristine and bandgap induced bilayer graphene (e) bilayer graphene resistance as a function of Vtg and Vbg. Adopted from (*8*).

1.5 Beyond graphene, other 2D materials

1.5.1 Other two-dimensional materials

The fascination with two dimensional (2D) materials that has started with the discovery of graphene, prompts condensed-matter physics and material research community to search for other 2D materials because of their unique electrical, optical, and mechanical properties as well as their novel physical phenomena (*10, 34-38*).

Among the known 2D materials are such as few-layered hexagonal boron nitride (hBN) (*39-41*), transition metal oxides including titania- and perovskite-based oxides (*35*), some members of III-VI/V-VI compound families (Bi_2Se_3, Bi_2Te_3) (*42, 43*), and transition metal dichalcogenides (TMDCs) (*44*), shown in Table 1.1. For nearly decades, graphene has received almost all of the attention as a first example of truly two dimensional crystals. However, recently researchers have started to pay more attention to these other two dimensional materials, particularly in TMDCs (*34, 37, 38*). We will also examine TMDCs materials with focus on electronic properties of MoS_2 atomic crystal based devices in Chapter 4.

<table>
<tr><td>Graphene family</td><td>Graphene</td><td colspan="2">hBN
'white graphene'</td><td>BCN</td><td colspan="2">Fluorographene</td><td>Graphene oxide</td></tr>
<tr><td rowspan="2">2D chalcogenides</td><td colspan="2" rowspan="2">MoS_2, WS_2, $MoSe_2$, WSe_2</td><td colspan="3" rowspan="2">Semiconducting dichalcogenides:
$MoTe_2$, WTe_2,
ZrS_2, $ZrSe_2$ and so on</td><td colspan="2">Metallic dichalcogenides:
$NbSe_2$, NbS_2, TaS_2, TiS_2, $NiSe_2$ and so on</td></tr>
<tr><td colspan="2">Layered semiconductors:
GaSe, GaTe, InSe, Bi_2Se_3 and so on</td></tr>
<tr><td rowspan="2">2D oxides</td><td>Micas, BSCCO</td><td colspan="2">MoO_3, WO_3</td><td colspan="3" rowspan="2">Perovskite-type:
$LaNb_2O_7$, $(Ca,Sr)_2Nb_3O_{10}$,
$Bi_4Ti_3O_{12}$, $Ca_2Ta_2TiO_{10}$ and so on</td><td>Hydroxides:
$Ni(OH)_2$, $Eu(OH)_2$ and so on</td></tr>
<tr><td>Layered Cu oxides</td><td colspan="2">TiO_2, MnO_2, V_2O_5,
TaO_3, RuO_2 and so on</td><td>Others</td></tr>
</table>

Table 1.1 2D materials library, adopted from (*10*)

1.5.2 Electronic structure of TMDC materials

TMDCs are a class of materials, having the chemical structure of MX_2, where M is a transition metal from group IV(Ti, Zr), group V(V,Nb, Ta), or group VI (Mo, W, etc), and X is a chalcogen (S, Se, Te). As the name, transition metal dichalcogeniges indicates, these

materials are composed of a transition metal such as molybdenum, tungsten, or niobium linked with chalcogens such as sulfur or selenium. The layered structure of a TMDCs comprises of transition metal atoms sandwiched between two layers of chalcogen atoms (M-X-M). The atoms in these three layers have a strong covalent bond between them, whereas each adjacent layer is bound together weakly by a van der Waals force (*10, 34, 37*).

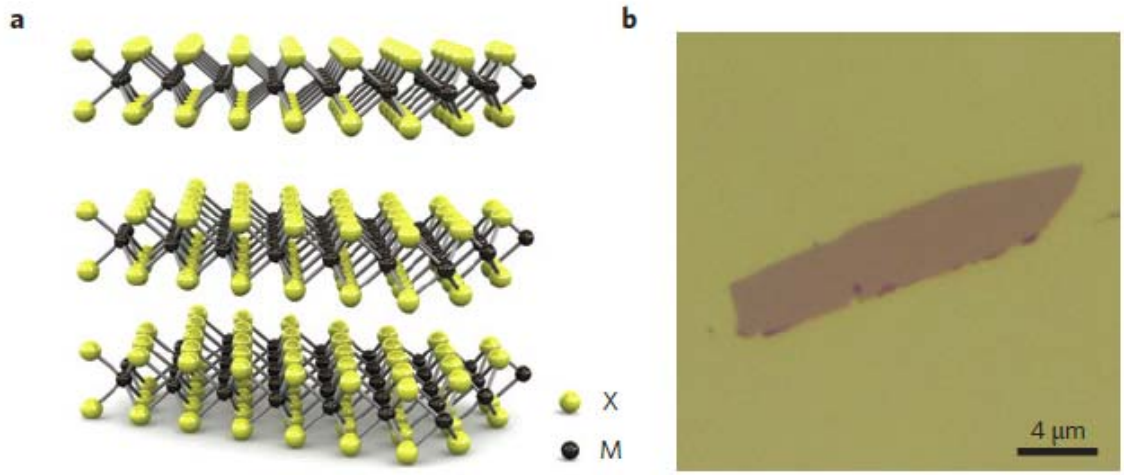

Figure 1.12 (a) 3D schematic representation of MX_2 structure with transition metal atom (M), and chalcogen atoms (X). (b) Optical micrograph of exfoliated monolayer MoS_2 flake. Adapted from (*44, 45*).

The monolayer of TMDCs has two polytypes, either a trigonal prismatic (known as 2H) or an octahedral (known as 1T), depending upon its respective position between transition metal and chalcogenides. For example, a monolayer of MoS_2, exfoliated via solution based on lithium intercalation method, is in the metallic 1T octahedral state. By annealing at 300C, the metallic 1T-MoS_2 state can be changed to the semiconducting 2H-MoS_2 state (*34, 46*).

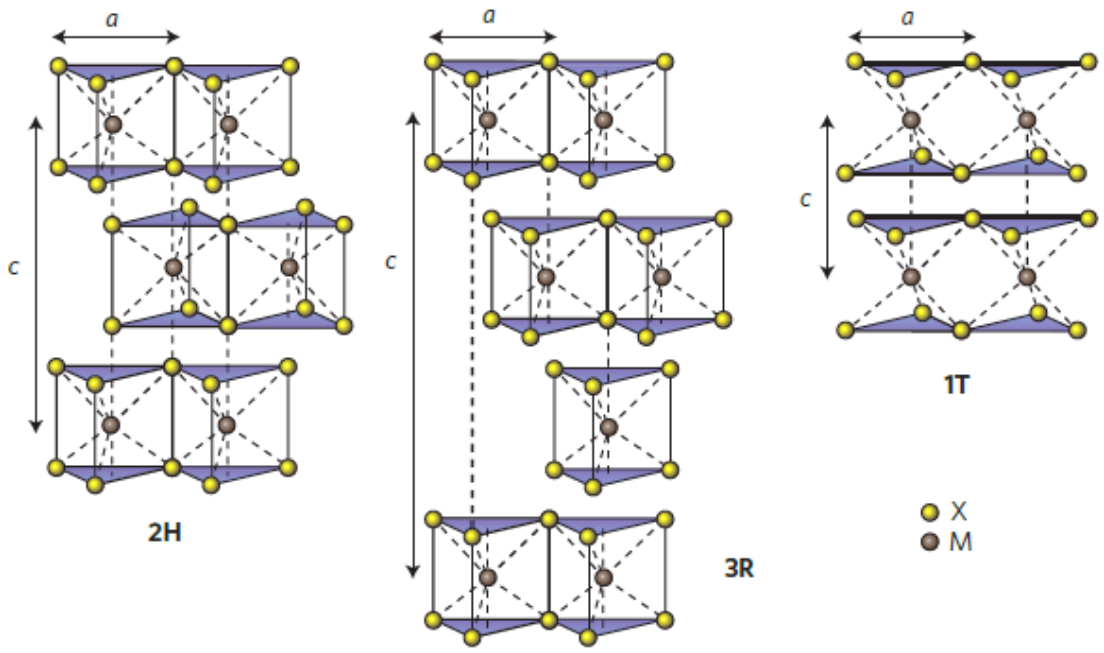

Figure 1.13 Each layer of TMDC materials is weakly held together via van der Waals force to form various bulk crystals. Schematics of structural polytypes: 2H (hexagonal symmetry, two layers per repeat unit, trigonal prismatic coordination), 3R (rhombohedral symmetry, three layers per repeat unit, trigonal prismatic coordination), and 1T (tetragonal symmetry, one layer per repeat unit, octahedral coordination). Adapted from (*34*).

The electronic properties of semiconducting TMDC change with layer number due to quantum confinement and the resulting change in hybridization between p_z orbitals on S atoms and d orbitals on Mo atoms. The band gap transition of bulk materials is indirect at Γ point, but gradually shifts to become direct for a monolayer at K point. By decreasing the thickness, experimental results shows a quantum confinement-induced shift in indirect gap from the bulk value of 1.29eV to the monolayer direct gap of 1.9eV (Fig.1.14), confirmed by absorption, photoluminescence, and photoconductivity spectroscopy. Similar behaviors of indirect to direct bandgap transition were reported for monolayer $MoSe_2$, WS_2, WSe_2 (*47, 48*) .

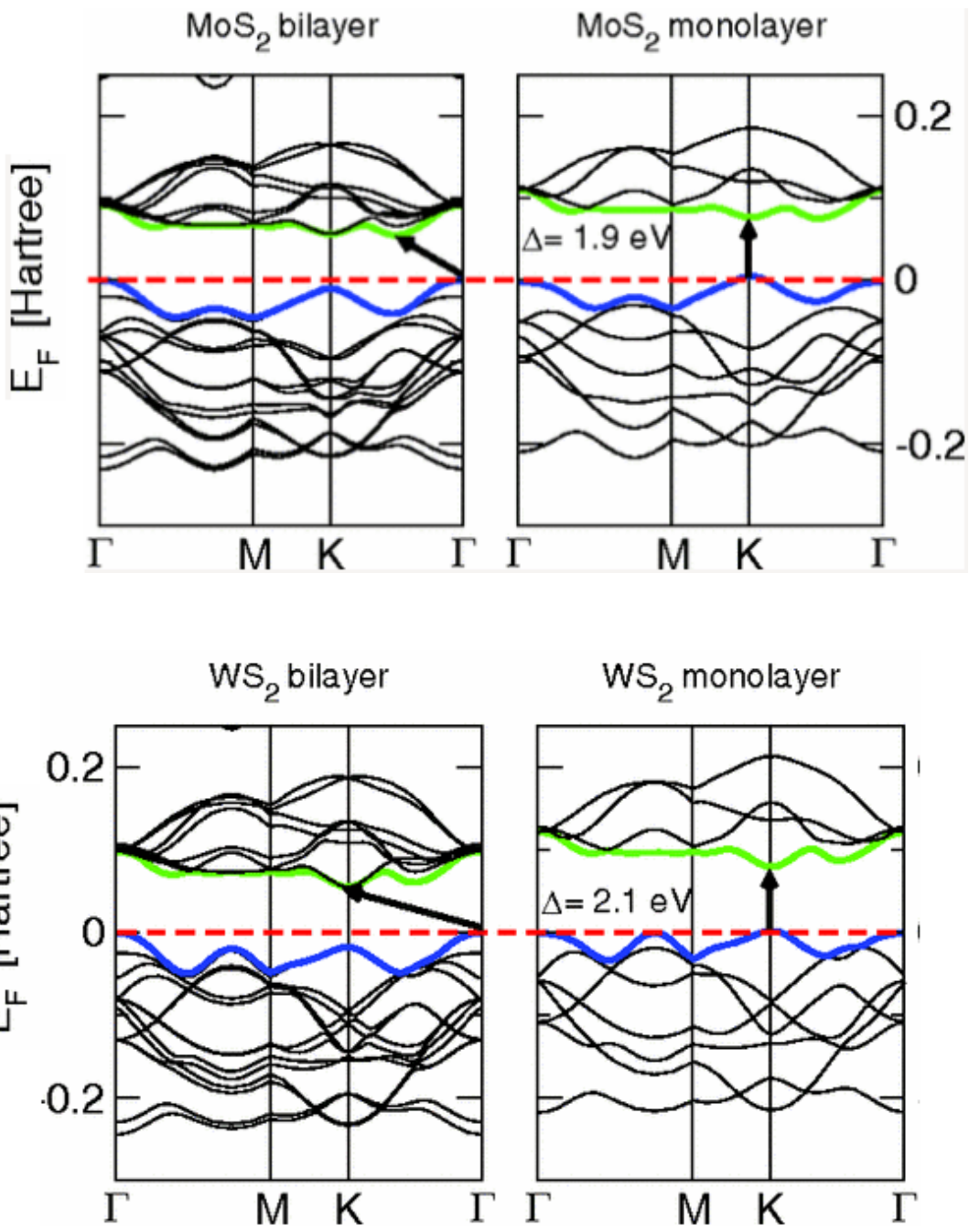

Figure 1.14 Band Structure calculated from DFT for bilayer and monolayer MoS_2 (Top), and WS_2 (Bottom). The arrow indicates fundamental bandgap. Adopted from (*7*).

	-S_2		-Se_2		-Te_2	
	Electronic characteristics	References	Electronic characteristics	References	Electronic characteristics	References
Nb	Metal; superconducting; CDW	138 (E)	Metal; superconducting; CDW	138,164 (E)	Metal	83 (T)
Ta	Metal; superconducting; CDW	138,164 (E)	Metal; superconducting; CDW	138,164 (E)	Metal	83 (T)
Mo	Semiconducting 1L: 1.8 eV Bulk: 1.2 eV	31 (E) 88 (E)	Semiconducting 1L: 1.5 eV Bulk: 1.1 eV	82 (T) 88 (E)	Semiconducting 1L: 1.1 eV Bulk: 1.0 eV	82 (T) 165 (E)
W	Semiconducting 1L: 2.1 eV 1L: 1.9 eV Bulk: 1.4 eV	25 (T) 82 (T) 88 (E)	Semiconducting 1L: 1.7 eV Bulk: 1.2 eV	83 (T) 88 (E)	Semiconducting 1L: 1.1 eV	83 (T)

Table 1.2 Band gap and electronic properties of several TMDC materials in experimental (E) and theoretical (T) values. Adopted from (*10*).

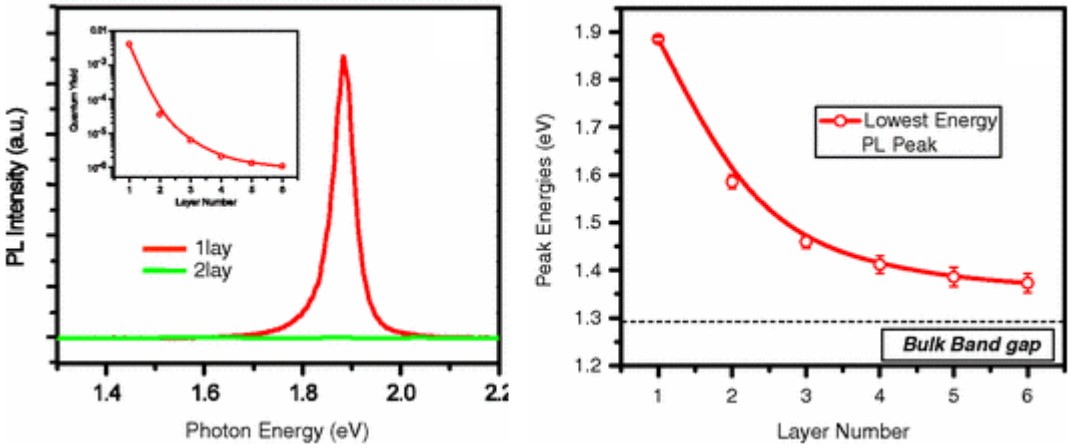

Figure 1.15 Photoluminescence spectra of monolayer and bilayer MoS2(Left): Band-gap of thin layer of MoS_2 (Right) Adopted from (*6*).

1.6 Quantum transport

1.6.1 Quantum effect in reduced dimension

In low dimensional materials like quantum dot (0D), nanotubes/nanowires (1D), and graphene/TMDs (2D), novel quantum transport phenomena can be assessed at low temperatures where thermal energy is insufficient to smear unique quantum conductance phenomena associated with discrete energy levels.

1.6.2 Quantum transport regimes

Depending on the contact junction transparency at low temperature, one can observe Coulomb blockade or Fabry-perot type oscillation in a carbon-nanotube device, as shown in Fig 1.16 (*49-51*).

Figure 1.16 shows 2D-differential conductance plot as a function of gate voltage, V_g and bias voltage, V. Coulomb blockade diamond patterns are observed at highly reflecting source-drain junction barriers, whereas Fabry-Perot interference patterns are observed at highly transmitting (transparent) junction barrier.

Coulomb blockade behavior, associated with charge quantization, is typically occurred in the weakly coupled quantum island (isolated conducting channel) to the metal electrode through tunneling barriers (*50*). And Fabry-Perot type interference of charge carriers from electronic device arises from the interference of electron waves reflected back and forth between two (source/drain metal) electrodes, giving rise to conductance oscillations (*51*), analogous to the oscillations in optical cavity between two partially reflecting parallel mirrors.

There has been a lot of research done on quantum behavior in 1-D nanostructures (*49-52*) however, quantum transport behavior in 2D materials has started attracting much attention recently. In this thesis, we will discuss novel quantum effects observed in devices made from atomically thin layered 2D materials, with focus on chirality dependent electron transport in bilayer graphene device in Chapter 3, and single electron charging behavior in MoS_2 device in Chapter 4.

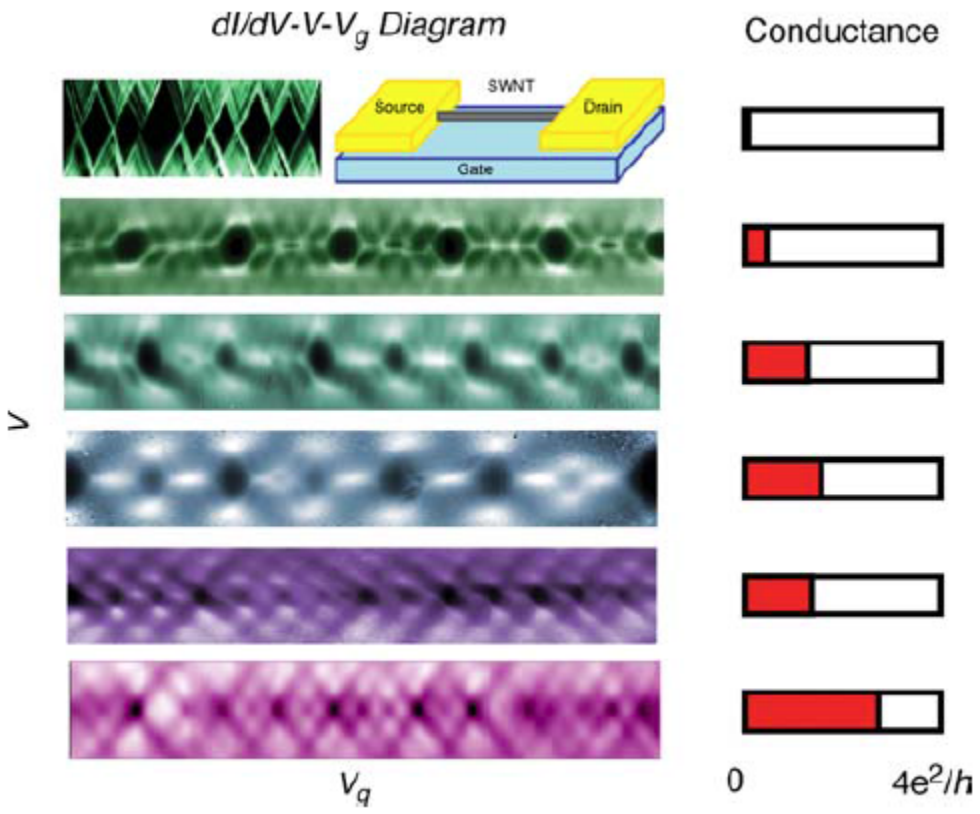

Figure 1.16 Two differential conductance plot as a function of V and Vg obtained from six representative devices at T = 1.5K.The bar graphs show averaged conductance of each device. The pattern of conductance shows the transformation from Coulomb blockade at highly opaque nanotube-metal junction, and four-fold degenerate patterns (two spin, two orbital states), to Fabry-Perot interference patterns at highly transparent nanotube-metal junction. Adopted from (*49*).

References

1. A. K. Geim, K. S. Novoselov, The rise of graphene. *Nat Mater* **6**, 183-191 (2007).
2. J. C. Charlier, J. P. Michenaud, X. Gonze, J. P. Vigneron, Tight-binding model for the electronic properties of simple hexagonal graphite. *Physical Review B* **44**, 13237-13249 (1991).
3. A. H. Castro Neto, F. Guinea, N. M. R. Peres, K. S. Novoselov, A. K. Geim, The electronic properties of graphene. *Reviews of Modern Physics* **81**, 109-162 (2009).
4. M. Edward, K. Mikito, The electronic properties of bilayer graphene. *Reports on Progress in Physics* **76**, 056503 (2013).
5. X. Li, X. Wang, L. Zhang, S. Lee, H. Dai, Chemically Derived, Ultrasmooth Graphene Nanoribbon Semiconductors. *Science* **319**, 1229-1232 (2008); published online EpubFebruary 29, 2008 (10.1126/science.1150878).
6. K. F. Mak, C. Lee, J. Hone, J. Shan, T. F. Heinz, Atomically Thin MoS2: A New Direct-Gap Semiconductor. *Physical Review Letters* **105**, 136805 (2010).
7. A. Kuc, N. Zibouche, T. Heine, Influence of quantum confinement on the electronic structure of the transition metal sulfide TS2. *Physical Review B* **83**, 245213 (2011).
8. Y. Zhang, T.-T. Tang, C. Girit, Z. Hao, M. C. Martin, A. Zettl, M. F. Crommie, Y. R. Shen, F. Wang, Direct observation of a widely tunable bandgap in bilayer graphene. *Nature* **459**, 820-823 (2009)http://www.nature.com/nature/journal/v459/n7248/suppinfo/nature08105_S1.html).
9. G. D. R Saito, M S Dresselhaus, Physical Properties of Carbon Nanotubes. *Imperial College Press*.
10. A. K. Geim, I. V. Grigorieva, Van der Waals heterostructures. *Nature* **499**, 419-425 (2013)10.1038/nature12385).
11. L. M. Malard, M. A. Pimenta, G. Dresselhaus, M. S. Dresselhaus, Raman spectroscopy in graphene. *Physics Reports* **473**, 51-87 (2009); published online Epub4// (http://dx.doi.org/10.1016/j.physrep.2009.02.003).
12. J. C. Meyer, A. K. Geim, M. I. Katsnelson, K. S. Novoselov, T. J. Booth, S. Roth, The structure of suspended graphene sheets. *Nature* **446**, 60-63 (2007); published online Epub03/01/print (http://www.nature.com/nature/journal/v446/n7131/suppinfo/nature05545_S1.html).
13. E. V. Castro, K. S. Novoselov, S. V. Morozov, N. M. R. Peres, J. M. B. L. dos Santos, J. Nilsson, F. Guinea, A. K. Geim, A. H. C. Neto, Biased Bilayer Graphene: Semiconductor with a Gap Tunable by the Electric Field Effect. *Physical Review Letters* **99**, 216802 (2007).
14. E. McCann, D. S. L. Abergel, V. I. Fal'ko, The low energy electronic band structure of bilayer graphene. *Eur. Phys. J. Spec. Top.* **148**, 91-103 (2007); published online Epub2007/09/01 (10.1140/epjst/e2007-00229-1).
15. S. Das Sarma, S. Adam, E. H. Hwang, E. Rossi, Electronic transport in two-dimensional graphene. *Reviews of Modern Physics* **83**, 407-470 (2011); published online Epub05/16/ (

16. M. I. Katsnelson, K. S. Novoselov, A. K. Geim, Chiral tunnelling and the Klein paradox in graphene. *Nat Phys* **2**, 620-625 (2006); published online Epub09//print (http://www.nature.com/nphys/journal/v2/n9/suppinfo/nphys384_S1.html).
17. K. S. Novoselov, A. K. Geim, S. V. Morozov, D. Jiang, Y. Zhang, S. V. Dubonos, I. V. Grigorieva, A. A. Firsov, Electric Field Effect in Atomically Thin Carbon Films. *Science* **306**, 666-669 (2004); published online EpubOctober 22, 2004 (10.1126/science.1102896).
18. D. C. Elias, R. V. Gorbachev, A. S. Mayorov, S. V. Morozov, A. A. Zhukov, P. Blake, L. A. Ponomarenko, I. V. Grigorieva, K. S. Novoselov, F. Guinea, A. K. Geim, Dirac cones reshaped by interaction effects in suspended graphene. *Nat Phys* **7**, 701-704 (2011)http://www.nature.com/nphys/journal/v7/n9/abs/nphys2049.html#supplementary-information).
19. A. S. Mayorov, R. V. Gorbachev, S. V. Morozov, L. Britnell, R. Jalil, L. A. Ponomarenko, P. Blake, K. S. Novoselov, K. Watanabe, T. Taniguchi, A. K. Geim, Micrometer-Scale Ballistic Transport in Encapsulated Graphene at Room Temperature. *Nano Letters* **11**, 2396-2399 (2011); published online Epub2011/06/08 (10.1021/nl200758b).
20. Y. W. Tan, Y. Zhang, K. Bolotin, Y. Zhao, S. Adam, E. H. Hwang, S. Das Sarma, H. L. Stormer, P. Kim, Measurement of Scattering Rate and Minimum Conductivity in Graphene. *Physical Review Letters* **99**, 246803 (2007); published online Epub12/14/ (
21. J. H. Chen, C. Jang, S. Adam, M. S. Fuhrer, E. D. Williams, M. Ishigami, Charged-impurity scattering in graphene. *Nat Phys* **4**, 377-381 (2008); published online Epub05//print (http://www.nature.com/nphys/journal/v4/n5/suppinfo/nphys935_S1.html).
22. V. I. Fal'ko, K. Kechedzhi, E. McCann, B. L. Altshuler, H. Suzuura, T. Ando, Weak localization in graphene. *Solid State Communications* **143**, 33-38 (2007); published online Epub7// (http://dx.doi.org/10.1016/j.ssc.2007.03.049).
23. Y. Zhang, Y.-W. Tan, H. L. Stormer, P. Kim, Experimental observation of the quantum Hall effect and Berry's phase in graphene. *Nature* **438**, 201-204 (2005); published online Epub11/10/print (http://www.nature.com/nature/journal/v438/n7065/suppinfo/nature04235_S1.html).
24. K. S. Novoselov, Z. Jiang, Y. Zhang, S. V. Morozov, H. L. Stormer, U. Zeitler, J. C. Maan, G. S. Boebinger, P. Kim, A. K. Geim, Room-Temperature Quantum Hall Effect in Graphene. *Science* **315**, 1379 (2007); published online EpubMarch 9, 2007 (10.1126/science.1137201).
25. K. S. Novoselov, E. McCann, S. V. Morozov, V. I. Fal/'ko, M. I. Katsnelson, U. Zeitler, D. Jiang, F. Schedin, A. K. Geim, Unconventional quantum Hall effect and Berry/'s phase of 2[pi] in bilayer graphene. *Nat Phys* **2**, 177-180 (2006); published online Epub03//print (http://www.nature.com/nphys/journal/v2/n3/suppinfo/nphys245_S1.html).
26. S. Lee, K. Lee, C.-H. Liu, G. S. Kulkarni, Z. Zhong, Flexible and transparent all-graphene circuits for quaternary digital modulations. *Nat Commun* **3**, 1018 (2012);

published online Epub08/21/online (http://www.nature.com/ncomms/journal/v3/n8/suppinfo/ncomms2021_S1.html).
27. L. Liao, Y.-C. Lin, M. Bao, R. Cheng, J. Bai, Y. Liu, Y. Qu, K. L. Wang, Y. Huang, X. Duan, High-speed graphene transistors with a self-aligned nanowire gate. *Nature* **467**, 305-308 (2010); published online Epub09/16/print (http://www.nature.com/nature/journal/v467/n7313/abs/nature09405.html#supplementary-information).
28. F. Schwierz, Graphene transistors. *Nat Nano* **5**, 487-496 (2010).
29. L. Liao, J. Bai, R. Cheng, Y.-C. Lin, S. Jiang, Y. Huang, X. Duan, Top-Gated Graphene Nanoribbon Transistors with Ultrathin High-k Dielectrics. *Nano Letters* **10**, 1917-1921 (2010); published online Epub2010/05/12 (10.1021/nl100840z).
30. M. Y. Han, B. Özyilmaz, Y. Zhang, P. Kim, Energy Band-Gap Engineering of Graphene Nanoribbons. *Physical Review Letters* **98**, 206805 (2007).
31. S. Lee, K. Lee, Z. Zhong, Wafer Scale Homogeneous Bilayer Graphene Films by Chemical Vapor Deposition. *Nano Letters* **10**, 4702-4707 (2010); published online Epub2010/11/10 (10.1021/nl1029978).
32. J. B. Oostinga, H. B. Heersche, X. Liu, A. F. Morpurgo, L. M. K. Vandersypen, Gate-induced insulating state in bilayer graphene devices. *Nat Mater* **7**, 151-157 (2008); published online Epub02//print (http://www.nature.com/nmat/journal/v7/n2/suppinfo/nmat2082_S1.html).
33. X. Li, W. Cai, J. An, S. Kim, J. Nah, D. Yang, R. Piner, A. Velamakanni, I. Jung, E. Tutuc, S. K. Banerjee, L. Colombo, R. S. Ruoff, Large-Area Synthesis of High-Quality and Uniform Graphene Films on Copper Foils. *Science* **324**, 1312-1314 (2009); published online EpubJune 5, 2009 (10.1126/science.1171245).
34. Q. H. Wang, K. Kalantar-Zadeh, A. Kis, J. N. Coleman, M. S. Strano, Electronics and optoelectronics of two-dimensional transition metal dichalcogenides. *Nat Nano* **7**, 699-712 (2012); published online Epub11//print (
35. M. Osada, T. Sasaki, Two-Dimensional Dielectric Nanosheets: Novel Nanoelectronics From Nanocrystal Building Blocks. *Advanced Materials* **24**, 210-228 (2012)10.1002/adma.201103241).
36. A. K. Geim, Graphene: Status and Prospects. *Science* **324**, 1530-1534 (2009); published online EpubJune 19, 2009 (10.1126/science.1158877).
37. G. Fiori, F. Bonaccorso, G. Iannaccone, T. Palacios, D. Neumaier, A. Seabaugh, S. K. Banerjee, L. Colombo, Electronics based on two-dimensional materials. *Nat Nano* **9**, 768-779 (2014); published online Epub10//print (10.1038/nnano.2014.207).
38. S. Z. Butler, S. M. Hollen, L. Cao, Y. Cui, J. A. Gupta, H. R. Gutiérrez, T. F. Heinz, S. S. Hong, J. Huang, A. F. Ismach, E. Johnston-Halperin, M. Kuno, V. V. Plashnitsa, R. D. Robinson, R. S. Ruoff, S. Salahuddin, J. Shan, L. Shi, M. G. Spencer, M. Terrones, W. Windl, J. E. Goldberger, Progress, Challenges, and Opportunities in Two-Dimensional Materials Beyond Graphene. *ACS Nano* **7**, 2898-2926 (2013); published online Epub2013/04/23 (10.1021/nn400280c).
39. C. R. Dean, A. F. Young, MericI, LeeC, WangL, SorgenfreiS, WatanabeK, TaniguchiT, KimP, K. L. Shepard, HoneJ, Boron nitride substrates for high-quality graphene electronics. *Nat Nano* **5**, 722-726 (2010); published online Epub10//print

(http://www.nature.com/nnano/journal/v5/n10/abs/nnano.2010.172.html#supplementary-information).

40. D. Pacilé, J. C. Meyer, Ç. Ö. Girit, A. Zettl, The two-dimensional phase of boron nitride: Few-atomic-layer sheets and suspended membranes. *Applied Physics Letters* **92**, 133107 (2008)doi:http://dx.doi.org/10.1063/1.2903702).
41. L. A. Ponomarenko, A. K. Geim, A. A. Zhukov, R. Jalil, S. V. Morozov, K. S. Novoselov, I. V. Grigorieva, E. H. Hill, V. V. Cheianov, V. I. Fal'ko, K. Watanabe, T. Taniguchi, R. V. Gorbachev, Tunable metal-insulator transition in double-layer graphene heterostructures. *Nat Phys* **7**, 958-961 (2011); published online Epub12//print (http://www.nature.com/nphys/journal/v7/n12/abs/nphys2114.html#supplementary-information).
42. Y. Zhang, K. He, C.-Z. Chang, C.-L. Song, L.-L. Wang, X. Chen, J.-F. Jia, Z. Fang, X. Dai, W.-Y. Shan, S.-Q. Shen, Q. Niu, X.-L. Qi, S.-C. Zhang, X.-C. Ma, Q.-K. Xue, Crossover of the three-dimensional topological insulator Bi2Se3 to the two-dimensional limit. *Nat Phys* **6**, 584-588 (2010); published online Epub08//print (
43. S. S. Hong, W. Kundhikanjana, J. J. Cha, K. Lai, D. Kong, S. Meister, M. A. Kelly, Z.-X. Shen, Y. Cui, Ultrathin Topological Insulator Bi2Se3 Nanoribbons Exfoliated by Atomic Force Microscopy. *Nano Letters* **10**, 3118-3122 (2010); published online Epub2010/08/11 (10.1021/nl101884h).
44. RadisavljevicB, RadenovicA, BrivioJ, GiacomettiV, KisA, Single-layer MoS2 transistors. *Nat Nano* **6**, 147-150 (2011)http://www.nature.com/nnano/journal/v6/n3/abs/nnano.2010.279.html#supplementary-information).
45. M. M. Benameur, B. Radisavljevic, J. S. Héron, S. Sahoo, H. Berger, A. Kis, Visibility of dichalcogenide nanolayers. *Nanotechnology* **22**, 125706 (2011).
46. R. Kappera, D. Voiry, S. E. Yalcin, B. Branch, G. Gupta, A. D. Mohite, M. Chhowalla, Phase-engineered low-resistance contacts for ultrathin MoS2 transistors. *Nat Mater* **13**, 1128-1134 (2014); published online Epub12//print (10.1038/nmat4080
http://www.nature.com/nmat/journal/v13/n12/abs/nmat4080.html#supplementary-information).
47. S. Tongay, J. Zhou, C. Ataca, K. Lo, T. S. Matthews, J. Li, J. C. Grossman, J. Wu, Thermally Driven Crossover from Indirect toward Direct Bandgap in 2D Semiconductors: MoSe2 versus MoS2. *Nano Letters* **12**, 5576-5580 (2012); published online Epub2012/11/14 (10.1021/nl302584w).
48. W. Zhao, Z. Ghorannevis, L. Chu, M. Toh, C. Kloc, P.-H. Tan, G. Eda, Evolution of Electronic Structure in Atomically Thin Sheets of WS2 and WSe2. *ACS Nano* **7**, 791-797 (2012); published online Epub2013/01/22 (10.1021/nn305275h).
49. W. Liang, M. Bockrath, H. Park, TRANSPORT SPECTROSCOPY OF CHEMICAL NANOSTRUCTURES: The Case of Metallic Single-Walled Carbon Nanotubes. *Annual Review of Physical Chemistry* **56**, 475-490 (2005)doi:10.1146/annurev.physchem.56.092503.141226).
50. L. Marty, V. Bouchiat, C. Naud, M. Chaumont, T. Fournier, A. M. Bonnot, Schottky Barriers and Coulomb Blockade in Self-Assembled Carbon Nanotube

FETs. *Nano Letters* **3**, 1115-1118 (2003); published online Epub2003/08/01 (10.1021/nl0342848).
51. W. Liang, M. Bockrath, D. Bozovic, J. H. Hafner, M. Tinkham, H. Park, Fabry - Perot interference in a nanotube electron waveguide. *Nature* **411**, 665-669 (2001); published online Epub06/07/print (
52. Z. Zhong, Y. Fang, W. Lu, C. M. Lieber, Coherent Single Charge Transport in Molecular-Scale Silicon Nanowires. *Nano Letters* **5**, 1143-1146 (2005); published online Epub2005/06/01 (10.1021/nl050783s).

Chapter 2

Wafer Scale homogeneous bilayer graphene films by Chemical Vapor Deposition

2.1 Introduction

The discovery of electric field induced bandgap opening in bilayer graphene opens new door for making semiconducting graphene without aggressive size scaling or using expensive substrates. However, bilayer graphene samples have been limited to μm^2 size scale thus far, and synthesis of wafer scale bilayer graphene posts tremendous challenge. Here we report homogeneous bilayer graphene films over at least 2 inch × 2 inch area, synthesized by chemical vapor deposition on copper foil and subsequently transferred to arbitrary substrates. The bilayer nature of graphene film is verified by Raman spectroscopy, atomic force microscopy (AFM), and transmission electron microscopy (TEM). Importantly, spatially resolved Raman spectroscopy confirms a bilayer coverage of over 99%. The homogeneity of the film is further supported by electrical transport measurements on dual-gate bilayer graphene transistors, in which bandgap opening is observed in 98% of the devices.

2.1.1 Motivation

Single and few-layer graphene (*1-5*) are promising materials for post-silicon electronics because of their potential of integrating bottom-up nanomaterial synthesis with top-down lithographic fabrication at wafer scale (*4, 6*). However, single layer graphene is intrinsically semimetal; introducing energy bandgap requires patterning nanometer-width graphene ribbons (*7-9*) or utilizing special substrates (*10-12*). Bilayer graphene, instead, has an electric field induced bandgap up to 250 meV, (*13-18*) thus eliminating the need for extreme scaling or costly substrates. Furthermore, exciton binding energies in bilayer graphene are also found to be tunable with electric field.(*19*) The unique ability of controlling the bandgap and the exciton energy can lead to new possibilities of bilayer graphene based electronics and photonics.

2.2 Synthesis of wafer scale Bilayer graphene

To date, most bilayer graphene samples are fabricated using mechanical exfoliation of graphite (*15-18*), which have limited sizes of μm^2 and are certainly not scalable. Recent developments in CVD method have allowed successful production of large scale single-layer graphene on metal substrate (*20-24*). However, the synthesis of uniform bilayer graphene film remains extremely challenging. Here we report the first synthesis of wafer scale bilayer graphene film over at least 2 inch × 2 inch area, limited only by our synthesis apparatus. Our method is based on CVD growth of bilayer graphene on copper surface, and is characterized by the depletion of hydrogen, high vacuum, and most importantly, slower cooling rate compared to previous single-layer graphene synthesis (*21, 22, 24*). The

optimal bilayer graphene film is grown at 1000 ºC for 15 minutes, with growth pressure of 0.5 Torr, CH_4 flow rate of 70 sccm, and a cooling rate of 18°C/min (0.3 °C/s)

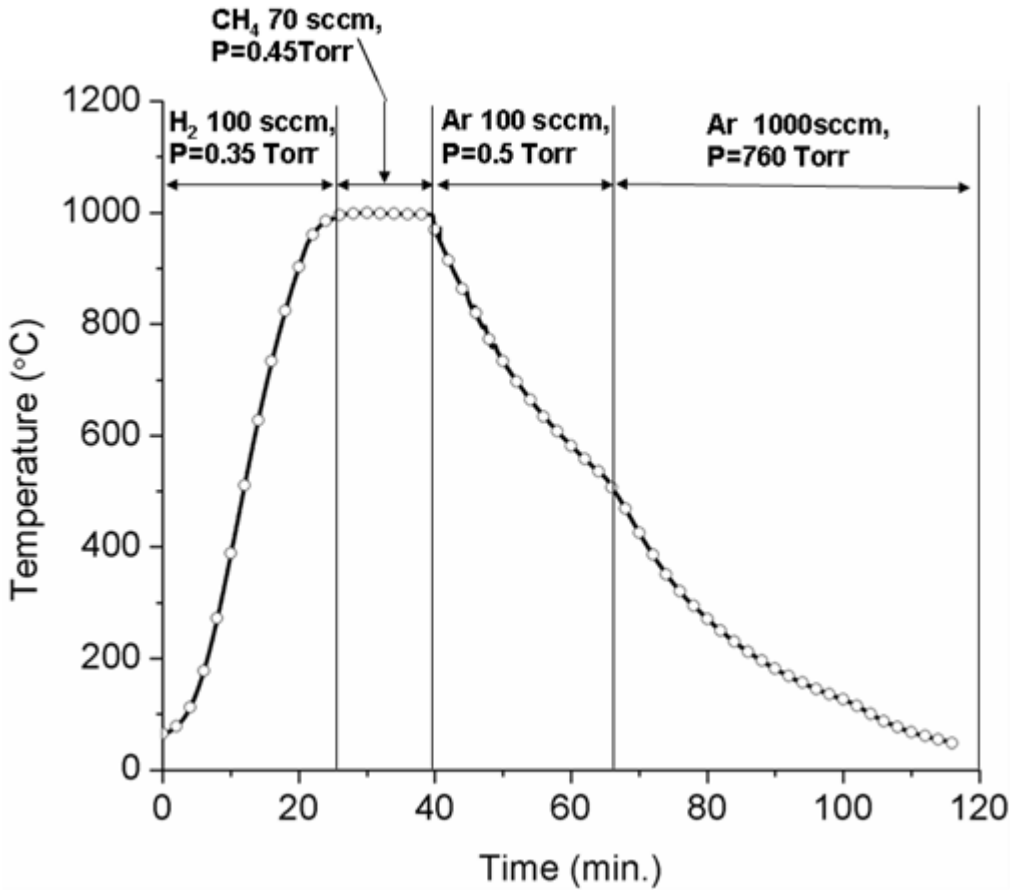

Figure 2.1 Temperature vs. time plot of bilayer graphene growth condition. Pressure value is denoted as "P".

2.3 Optical Identification of layer number of bilayer graphene film

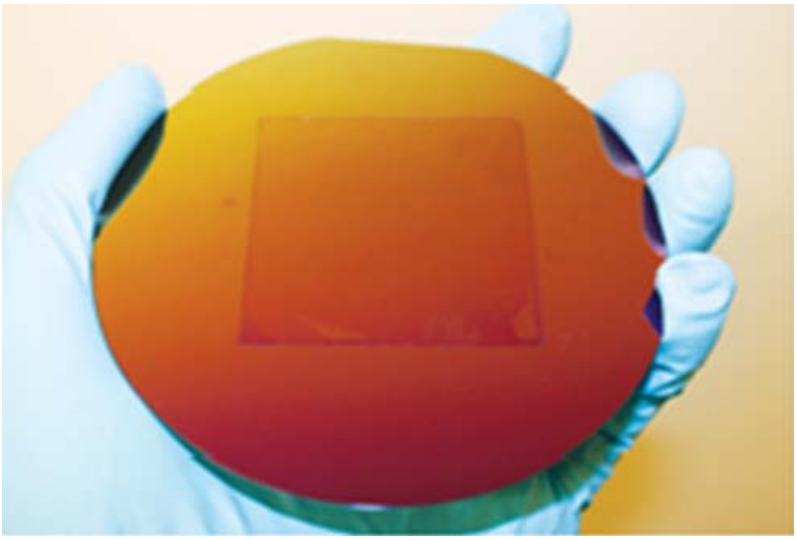

Figure 2.2 Photograph of a 2 inch × 2 inch bilayer graphene film transferred onto a 4 inch Si substrate with 280nm thermal oxide.

Figure 2.3 Optical microscopy image showing the edge of bilayer graphene film.

Figure 2.2 shows photographic image of a wafer scale (2 inch × 2 inch) bilayer graphene film transferred onto a 4 inch silicon wafer with 280 nm thick SiO_2. A typical optical microscope image (Fig. 2.3) of the transferred bilayer graphene film shows almost no color variation except for the region where the film is torn and folded.

To identify the number of layers for our graphene sample, the film thickness is first measured using AFM (Fig. 2.4). Height profiles across patterned graphene edges show that thickness of our graphene samples range from 0.9 nm to 1.3 nm, suggesting number of graphene layers below 3 (*23*).

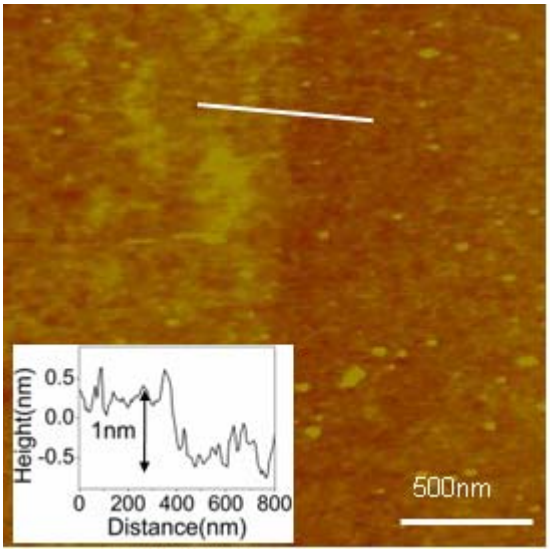

Figure 2.4 AFM image of bilayer graphene transferred onto SiO_2/Si. (Inset) Height profile obtained by taking cross section along the white line on the image was found to be 1nm.

2.3.1 Raman Spectroscopy of bilayer graphene

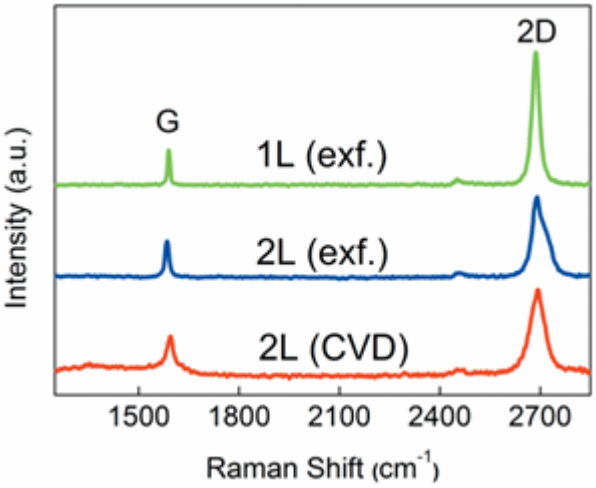

Figure 2.5 Raman spectra taken from CVD grown bilayer graphene (red solid line), exfoliated single-layer (green solid line) and bilayer graphene (blue solid line) samples. Laser excitation wavelength is 514 nm.

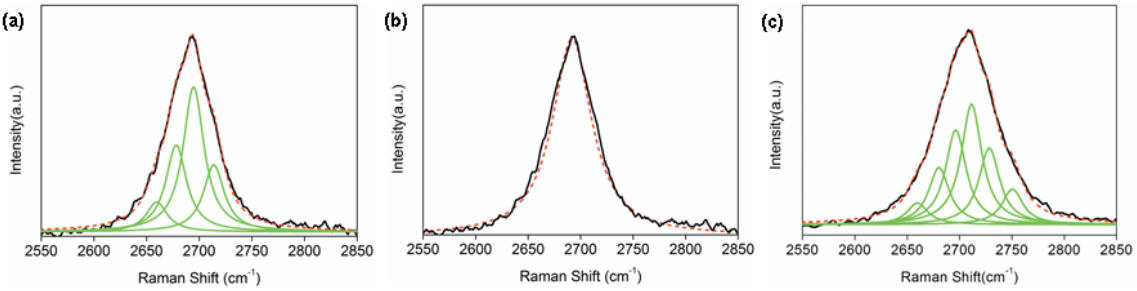

Figure 2.6 (a) The measured 2D Raman band of a bilayer with the FWHM of 45cm^{-1}. The peak can be well-fitted with the sum of four single Lorentzian (green solid line) of 24cm^{-1} FWHM. (b) Single Lorentzian fit (red dash line) of the same data in Fig. S2a clearly shows deviation from the measured 2D band. (c)**,** The measured 2D Raman band of a trilayer with the FWHM of 62cm^{-1}. 2D peak of trilayer are fitted with six single Lorentzian (green solid line)

We further performed Raman spectroscopy measurements (Renishaw spectrometer at 514nm) on ten randomly chosen spots across the film, and compared them with reference samples prepared by mechanically exfoliating Kish graphite (*17, 25, 26*). The red curve in

Fig. 2.5 represents a typical Raman spectrum from our sample. Two peaks are clearly visible between Raman shift of 1250 cm^{-1} – 2850 cm^{-1}, corresponding to the G band (~1595 cm^{-1}) and 2D band (~2691 cm^{-1}), respectively (*26-30*). Importantly, the spectrum exhibits several distinctive features. First, 2D band shows higher peak intensity than G band with the 2D-to-G intensity ratio I_{2D}/I_G ~2.31, suggesting the number of graphene layers less than 3 (*24, 27, 29*). Second, the full width at half maximum (FWHM) of 2D band peak is measured to be ~45 cm^{-1}, exceeding the cut-off of ~30 cm^{-1} for single-layer graphene (*25, 26, 28*). Third, the 2D band peak cannot be fitted with single Lorentzian (Fig. 2.5), but fitting from four Lorentzian peaks with a FWHM of 24 cm^{-1} yields excellent agreement (Fig. 2.6).(*26-28*) Raman spectra taken from the other 9 spots show similar features with the 2D band FWHM of 43~53 cm^{-1}. These observations are strong reminiscent of characteristic bilayer graphene Raman spectrum. In addition, reference Raman spectra taken under identical conditions from exfoliated single-layer (green curve) and bilayer (blue curve) graphene are also presented in Fig. 2.5. Exfoliated single-layer graphene shows a 2D band FWHM of 24 $cm^{-1}$and I_{2D}/I_G of 3.79, while exfoliated bilayer graphene shows a FWHM of 46 cm^{-1} and I_{2D}/I_G of 2.25. Together, the AFM height measurements, the Raman spectra, and the direct comparison with the exfoliated samplesclearly supports the bilayer nature of our CVD synthesized graphene film. We also measured the D band to G band intensity ratio, I_D/I_G, of our bilayer graphene sample to be around 0.11~0.3, indicating a relatively low defect density.

2.3.2 Transmission electron microscopy of bilayer graphene

TEM selected area electron diffraction pattern was measured to further characterize the graphene film (Figure 2.7). The six-fold symmetry is clearly visible and Bravais-Miller (hkil) indices are used to label the diffraction peaks. Importantly, the diffraction intensities of inner peaks from equivalent planes {1100} are always higher than outer peaks from {2100}. The intensity ratios of I_{-1010}/I_{-1-120} and I_{-1100}/I_{1-210} are close to 0.28 (Fig. 2.7b), indicating that the film is not a single layer and it retains AB stacking structure (*31-33*).

We further studied the tilt angle-dependent diffraction peak intensity for both inner and outer peaks. As shown in Fig. 2.6c, both (0-110) and (-1-120) peaks show strong intensity modulation with tilt angle, and both peaks can be suppressed completely at certain angle. It is known that monolayer graphene has only zero order Laue zone and weak intensity modulation is expected at any angle (*32, 33*). Our TEM results again agree with AFM and Raman measurements for the bilayer nature of the graphene film. We also notice additional diffraction spots, which are caused by the residues on the film due to insufficient sample cleaning.

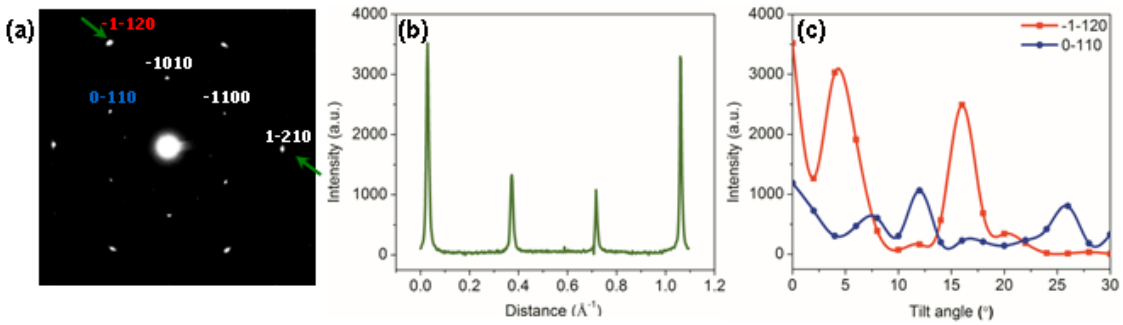

Figure 2.7 Selected area electron diffraction pattern of bilayer graphene. (a) Normal incident diffraction pattern of bilayer graphene sample. The bilayer graphene film was transferred onto copper grid with holy carbon supporting film. The diffraction image was taken by JEOL 2010F Analytical Electron Microscope with acceleration voltage of 200 kV. (b) Profile plot of diffraction peak intensities across a line cut indicated by the green arrows shown in (a). (c) Diffraction peak intensities as a function of tilt angle for (0-110) (in red) and (-1-120) (in blue).

2.3.3 Spatially resolved Raman spectroscopy of CVD bilayer graphene

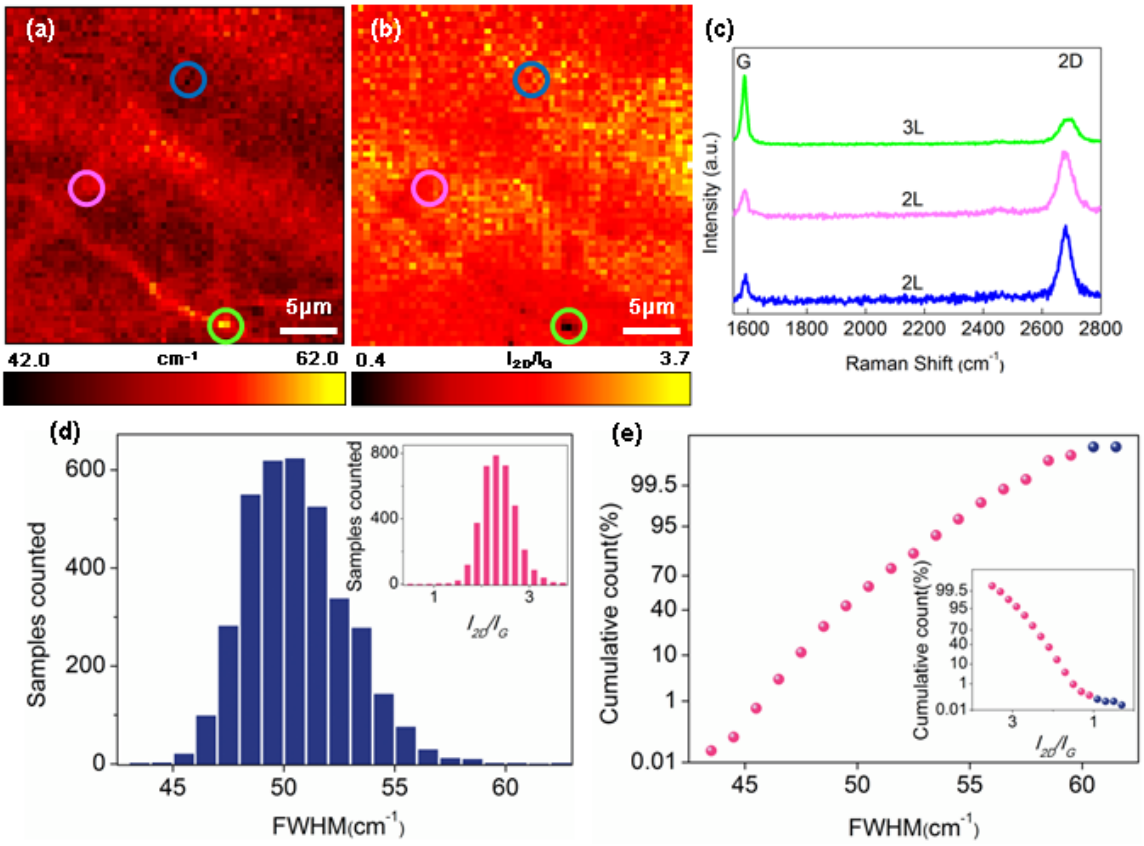

Figure 2.8 (a) and (b)**,** Two-dimensional color mapping of the FWHMs of Raman 2D band and I_{2D}/I_G ratios over 30 μm × 30 μm area, respectively. (c) Raman spectra from the marked spots corresponding colored circles showing bilayer and trilayer graphene. (d) Histogram of the FWHMs of Raman 2D band corresponding to area shown in (a)**.** (Top right Inset**)** Histogram of I_{2D}/I_G ratios for the same area. (e) Cumulative count plot of FWHMs of 2D band. Pink (blue) spheres represent the FWHM less (more) than 60 cm^{-1}. **(**Inset**)** Cumulative count plot of I_{2D}/I_G ratios. Pink (blue) spheres indicate the ratio larger (smaller) than 1. (For Raman mapping, λ_{laser}=514 nm, 500nm step size, 100x objector).

To further evaluate the uniformity of CVD grown bilayer graphene film, we performed spatially resolved Raman spectroscopy. Here, identifications of the number of graphene layers rely on combination of the FWHM of 2D band (*24, 26-28, 30*) and peak intensity ratio I_{2D}/I_G (*23, 24, 27, 29*). Figure 2.8a shows a color map of the 2D band peak width over 30 μm by 30 μm area, with FWHM values ranging from 42 cm^{-1} (dark color)

to 63cm^{-1} (bright yellow). The data show uniformly distributed red color with only a few localized yellow spots. The peak intensity ratios I_{2D}/I_G are also mapped in color (Fig. 2.8b) over the same area, with values ranging from 0.37 (dark color) to 3.77 (bright yellow). Comparisons between Fig. 2.8a and Fig. 2.8b reveal that larger peak widths are consistent with smaller I_{2D}/I_G ratios. Furthermore, Fig. 2.8c compares the Raman spectra taken from three representative spots indicated using green, pink, and blue circles. Raman spectrum taken at green-circled spot has the largest FWHM (62.9 cm^{-1}) and smallest I_{2D}/I_G (0.37), indicating trilayer graphene (Fig. 2.8b); pink-circled (blue-circled) spot shows FWHM = 55 cm^{-1} and I_{2D}/I_G = 2.2 (FWHM = 43.8 cm^{-1} and I_{2D}/I_G = 2.91), indicating bilayer graphene. These results confirm that the CVD bilayer graphene film is highly homogeneous, with only very small fraction corresponding to possibly 3 layers.

We then quantified the bilayer graphene coverage by studying the statistics of 2D band peak width and I_{2D}/I_G ratio. Figure 2.8d illustrates the histogram of the FWHMs of 2D band taken from the Raman mapping. The average peak width is determined to be 51 ± 2 cm^{-1}. Furthermore, cumulative counts plotted in Fig. 2.8e indicate that more than 99% of the FWHM values are below 60 cm^{-1} (pink spheres). In addition, the histogram of I_{2D}/I_G ratios (Fig. 2.8d, inset) shows an average value of 2.4 ± 0.4, and the corresponding cumulative count plot (Fig. 2.8e, inset) shows that more than 99% of I_{2D}/I_G ratios are larger than 1. Using FWHM = 60 cm^{-1} together with I_{2D}/I_G = 1 as the crossover values between bilayer and trilayer graphene, our data give an estimate of at least 99% coverage of bilayer graphene with less than 1% of trilayer over the entire area.

2.4 Electrical transport studies on dual-gate bilayer graphene device

2.4.1 Double gate bilayer graphene device fabrication

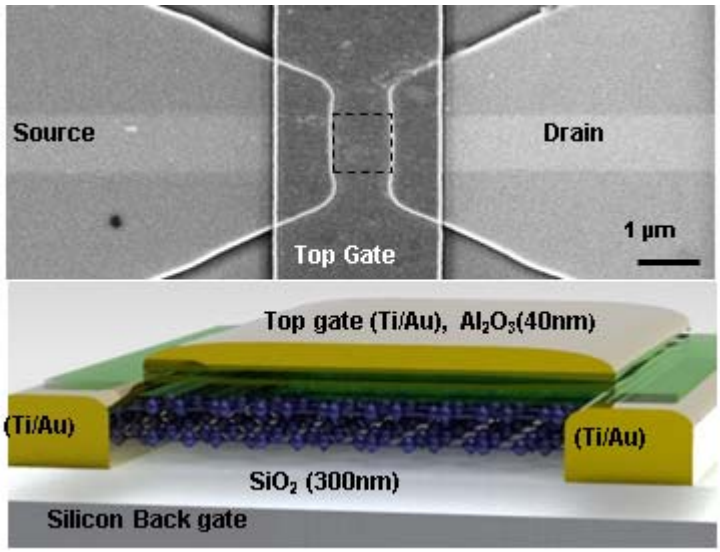

Figure 2.9 Scanning electron microscopy image (top) and illustration (bottom) of a dual-gate bilayer device. The dashed square in the SEM image indicates the 1μm × 1μm bilayer graphene piece underneath the top gate.

A direct verification of the bilayer nature of our CVD graphene film comes from electrical transport measurements. For this purpose, dual-gate bilayer graphene transistors were fabricated with three different dimensions, channel length and channel width of 1 μm×1μm, 1 μm×2μm, and 2 μm×2μm, respectively. A scanning electron microscope (SEM) image and an illustration of the fabricated device are shown in Fig. 2.9. All devices have a local top gate and a universal silicon bottom gate with Al_2O_3 (40nm) and SiO_2 (310 nm) as the respective gate dielectrics. This dual-gate structure allows simultaneous

manipulation of bilayer graphene bandgap and the carrier density by independently inducing electric fields in both directions (*15, 16*).

2.4.2 Two dimensional resistance map of double gated bilayer graphene device

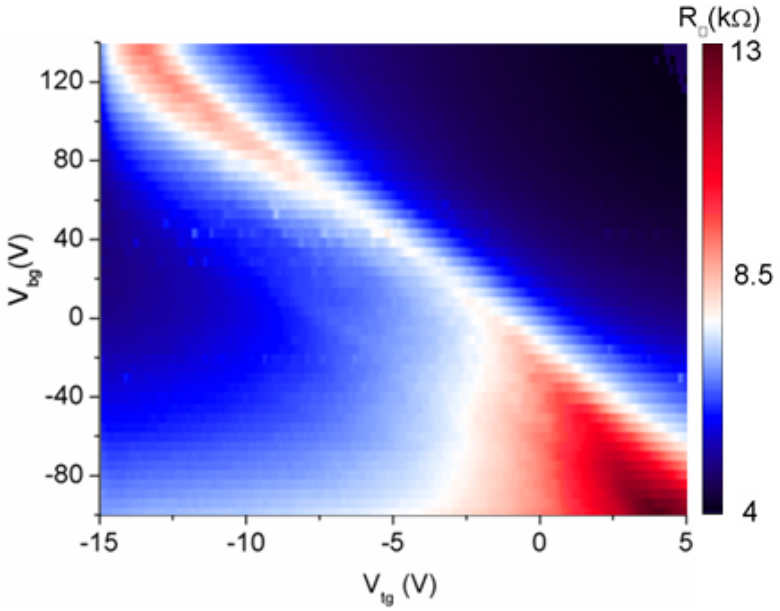

Figure 2.10 Two dimensional color plot of square resistance $R_{\square}$ vs. top gate voltage V_{tg} and back gate voltage V_{bg} at temperature of 6.5K.

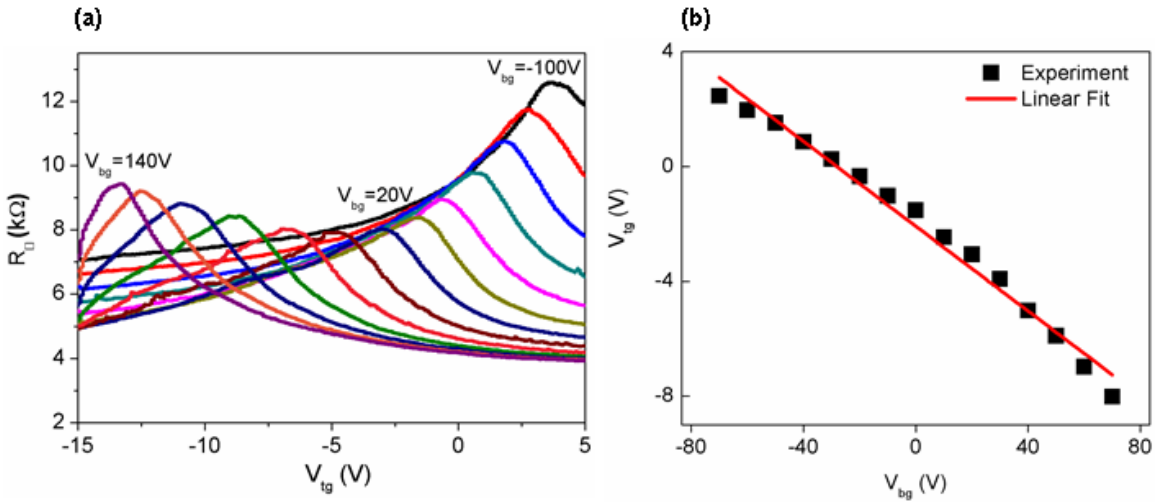

Figure 2.11 (a) $R_{\square}$ vs. V_{tg} at different value of fixed V_{bg}. The series of curves are taken from V_{bg} of -100V to 140V, with 20V increment. (b) The charge neutral points indicated as set of (V_{tg}, V_{bg}) values at the peak square resistance $R_{\square,dirac}$. The red line is the linear fit. The electrical measurements were carried out in a closed cycle cryogenic probe station (LakeShore, CRX-4K), using lock-in technique at 1kHz with AC excitation voltage of 100μV.

Figure 2.10 shows a two dimensional color plot of square resistance $R_{\square}$ vs. both top gate voltage (V_{tg}) and bottom gate voltage (V_{bg}), obtained from a typical 1×1 μm device at 6.5 K. The red and blue colors represent high and low square resistance, respectively. The data clearly show that $R_{\square}$ reach peak values along the diagonal (red color region), indicating a series of charge neutral points (Dirac points) when the top displacement fields cancel out the bottom displacement fields (*15, 16*). More importantly, the peak square resistance, $R_{\square, Dirac}$, reaches maximum at the upper left and lower right corner of the graph, where the average displacement fields from top and bottom gates are largest. Horizontal section views of the color plot in Fig. 2.10 are also shown in Fig. 2.11a, with $R_{\square}$ plotted against V_{tg} at fixed V_{bg} from -100 to 140 V. Once again, for each $R_{\square}$ vs. V_{tg} curve square resistances exhibit a peak value, and $R_{\square, Dirac}$ increases with increasing V_{bg} in both positive and negative

direction. The charge neutral points are further identified in Fig. 2.11b in terms of the (V_{tg}, V_{bg}) values at $R_{\square,\ Dirac}$. Linear relation between V_{tg} and V_{bg} is observed with a slope of -0.073, which agrees with the expected value of $-\varepsilon_{bg}d_{tg}/\varepsilon_{tg}d_{bg}$ = -0.067, where ε and d correspond to the dielectric constant and thickness of the top gate (Al_2O_3: d_{tg} = 40nm, ε_{tg}=7.5) and bottom gate (SiO_2: d_{bg} = 310nm, ε_{bg}=3.9) oxide (*15, 16*). We also notice the deviation from linear relation at high field; the origin of which is not understood currently and requires further study.

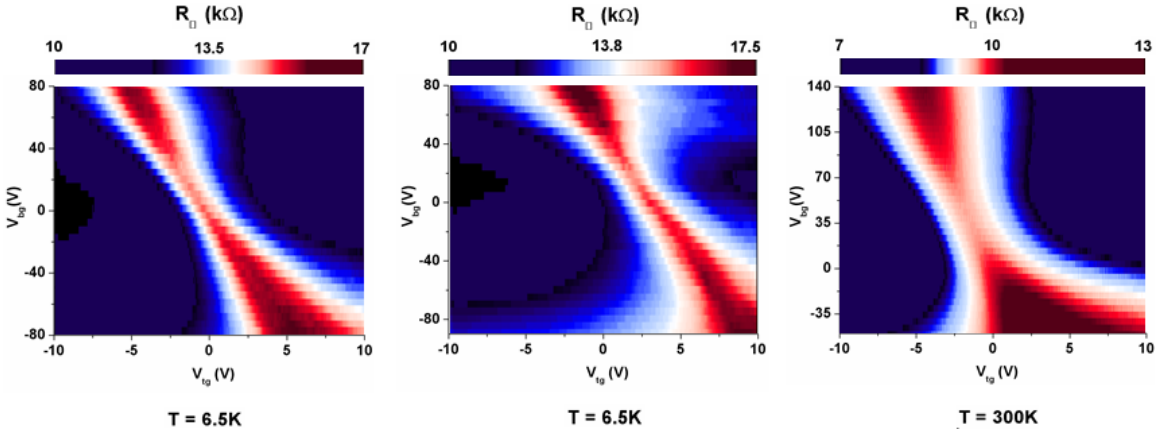

Figure 2.12 Three dual-gate graphene devices showing bilayer transport behaviour.

Similar results from three other devices are shown in Fig. 2.12, and more than 46 measured devices show qualitative agreement. These electrical characterizations yield direct evidence for the successful synthesis of bilayer graphene. The observation of increasing $R_{\square,\ Dirac}$ values at higher fields is an unmistakable sign of bandgap opening in bilayer graphene (*15, 16*). In comparisons, the peak resistance at the charge neutral point should remain roughly constant for single-layer graphene (*15*), while $R_{\square,\ Dirac}$ decreases at higher field for trilayer graphene (Fig2.13) (*5*). In addition, we also compared the temperature dependence of $R_{\square,\ Dirac}$ at $V_{bg} \sim$ 0V and $V_{bg} \sim$ -100 V (Fig. 2.14). Larger

variation of $R_{\square,\ Dirac}$ vs. temperature is observed under higher electric field, which again agrees with field-induced bandgap opening in bilayer graphene (*15, 16*). We note that the observed resistance modulation due to electric field and temperature are smaller compared to devices made by mechanical exfoliation (*15, 16*), which can be attributed to the polycrystalline nature of CVD graphene film. We also note that our devices show large fluctuations of the offset voltage (from impurity and surface doping), with some cases exceeding 140 V for the bottom gate. This could be caused by the ion residues from the etching process, and further investigations are needed.

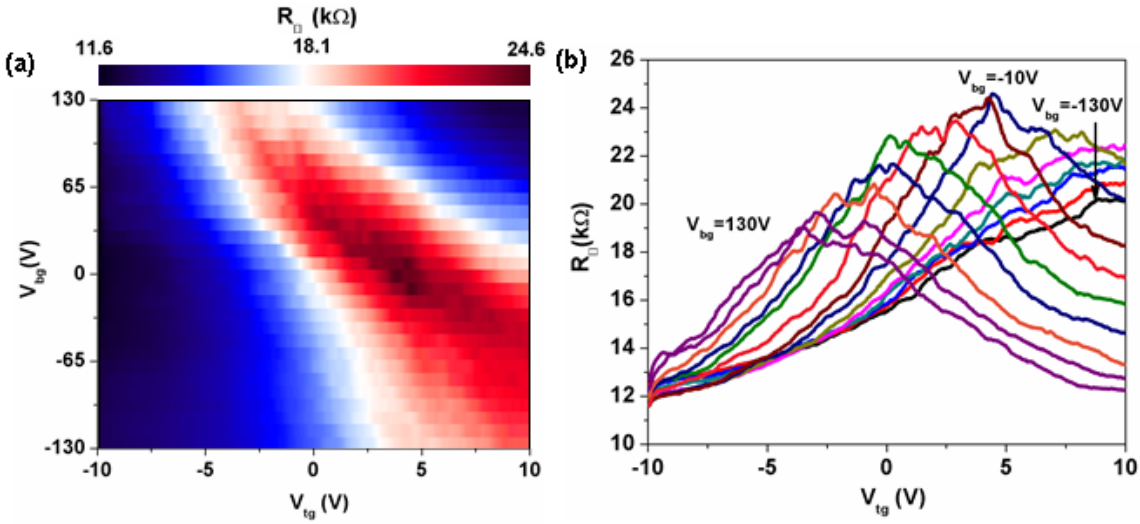

Figure 2.13 (a) A device showing trilayer transport behaviour. The observed peak square resistance decreases as increasing field. This is distinctively different from bilayer response. (b) Horizontal section views with $R_{\square}$ plotted against V_{tg} at fixed V_{bg} from -130 to 130 V with 20V increment.

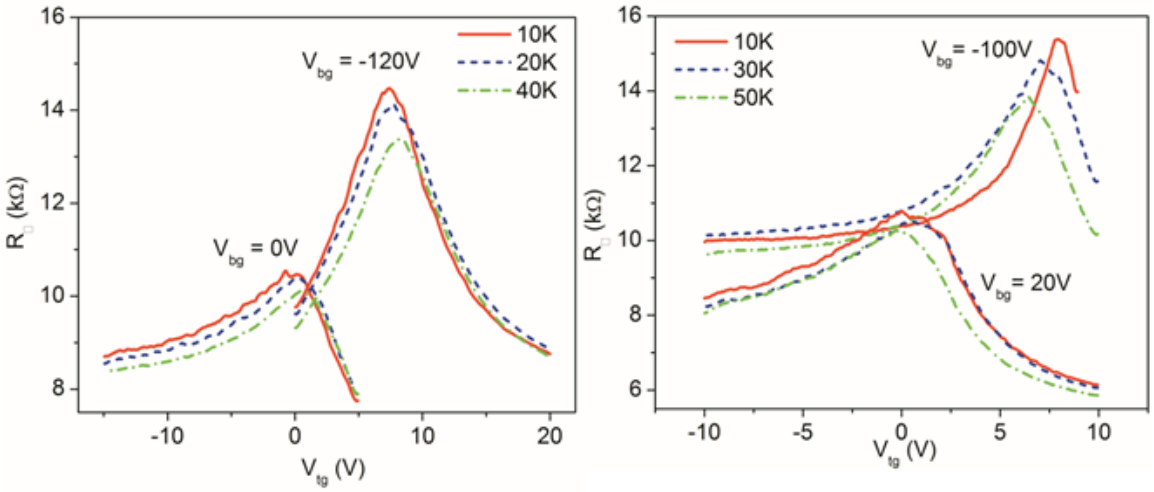

Figure 2.14 Two dual-gate graphene devices showing temperature dependent resistance versus top gate voltage sweep at two different back gate voltage.

2.4.3 Bilayer statistics from electrical transport measurement on dual-gate graphene devices

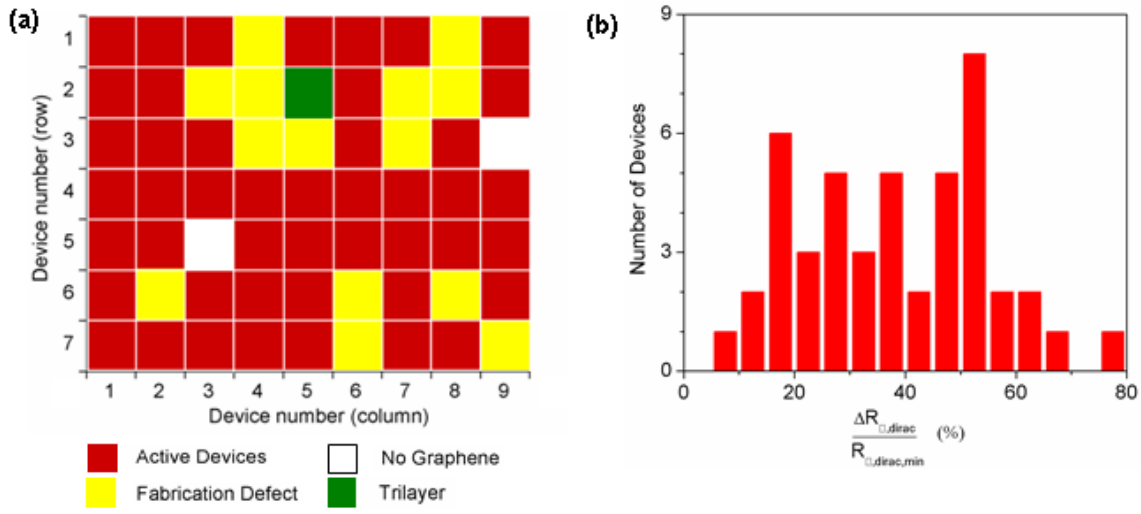

Figure 2.15 (a) A color-coded map of 63 devices (7 rows x 9 columns) fabricated across the same graphene film. The red squares indicate bilayer graphene confirmed by transport measurement; the yellow squares indicate devices which have fabrication defects; the white squares mark the region with no graphene; and the green square represents device with trilayer response from the transport measurement. (b) Histogram of $\Delta R_{\square,dirac}$ / $R_{\square,dirac,min}$ values in percentage for 46 active devices. $\Delta R_{\square,dirac}$ corresponds to the maximum difference in $R_{\square,dirac}$ within V_{tg} of ±10V and V_{bg} of ±120V. $R_{\square,dirac,min}$ is the minimum peak resistance.

We also studied the statistics of bilayer graphene occurrence for 63 (7 row x 9 columns) dual-gate devices fabricated across the same film (Fig. 2.15a). 46 out of 63 devices show bilayer graphene behaviors, characterized by increasing $R_{\square,Dirac}$ at larger fields. Of the remaining devices, 2 devices contain no graphene pieces, and 14 devices have fabrication defects. Interestingly, one device shows trilayer characteristics (*5*) with decreasing $R_{\square,Dirac}$ under both more positive and more negative fields (Supporting information Fig. S4). Hence, 46 out of 47 (98%) working devices show bilayer

characteristics. For the bilayer graphene devices, we also calculated the maximum percentage changes of peak square resistance, $\Delta R_{\square,Dirac} / R_{\square,Dirac,min}$, in which $\Delta R_{\square,Dirac}$ denotes the maximum difference in $R_{\square,Dirac}$ within V_{tg} of ±10V and V_{bg} of ±120V, and $R_{\square,dirac,min}$ is the minimum peak square resistance. The histogram of the percentile changes is shown in Fig. 2.15b, with an average peak resistance change of 38% and maximum value of 77%. In addition, the average room temperature carrier mobilities were measured to be ~580 $cm^2V^{-1}s^{-1}$, which are the lower-bond values without excluding the device contact resistance. The smaller-than-expected $R_{\square,Dirac}$ modulation is believed to be caused by defects and unintended impurity doping (*16*). High quality gate dielectrics have been shown to improve the bilayer graphene device performance dramatically (*18*). The electrical measurement results echo the finding from Raman measurements: our CVD grown bilayer graphene film is highly homogeneous.

2.5 Various synthesis conditions with different gas flow compositions and cooling rate

Sample No	Growth Pressure (mTorr)	Growth Temperature (°C)	Growth Time (min)	Ar Flow rate (sccm)	CH4 Flow rate (sccm)	H2 Flow rate (sccm)	2D Band FWHM (514nm)	I_{2D}/I_G (514nm)	I_D/I_G (514nm)	Cooling rate (°C/min)
1	500	1000	15	0	70	0	46.6	2.628	0.258	18
2	500	1000	15	0	140	0	47	2.12	0.57	18
3	Ambient	1000	15	1000	50	0	59.12	1.402	0.36	18
4	1500	1000	15		40	600	60	0.64	1.11	18

Table 2.1 Raman Spectra results of graphene samples synthesized at different gas flow composition under different pressure with same slow cooling rate

Lastly, we would like to comment on the key growth parameters for our CVD bilayer graphene films. It has been suggested that graphene growth on copper surface is self-limited to single layer(*24*), but both of our Raman and electrical characterizations clearly prove otherwise. We systematically varied the key growth conditions, and the resulting film quality was evaluated using Raman spectroscopy (Supporting Information, and Table S1). In brief, increasing CH_4 flow rate by 2 times has no noticeable effect on 2D band width and I_{2D}/I_G values, except for a larger I_D/I_G ratio corresponding to more disorders. However, increasing growth pressure to ambient condition leads to larger 2D band width and smaller I_{2D}/I_G ratio, indicating the increasing portion of trilayer graphene. This result is consistent with recent literature, that higher pressure favors multilayer graphene growth on copper surface.(*34*)[5] Based on our results, we speculate that the key parameter for the bilayer graphene film growth is the slow cooling process (~18°C/min). Cooling rate has been

found to be the critical factor for forming uniform single or bilayer graphene on Nickel (*21, 35, 36*). Our initial results should promote studies of the detailed growth mechanism for bilayer graphene.

2.6 Conclusion

The size of the homogeneous bilayer graphene films is limited only by the synthesis apparatus, which can be further scaled up. The integration with existing top-down lithography techniques should bring significant advancement for high performance, light-weight, and transparent graphene electronics and photonics. Furthermore, because the CVD grown bilayer graphene film can be transferred to arbitrary substrates, adopting high-k dielectrics for both top and bottom gates should drastically improve the device performance.(*18*) A few voltages applied to the gate electrodes will be able to open up sizeable bandgap (~250 meV).

References and Notes

1. A. K. Geim, K. S. Novoselov, *Nat Mater* 6, 183 (2007).
2. A. H. Castro Neto, F. Guinea, N. M. R. Peres, K. S. Novoselov, A. K. Geim, *Reviews of Modern Physics* 81, 109 (2009).
3. A. K. Geim, *Science* 324, 1530 (2009).
4. F. Schwierz, *Nat Nano* 5, 487 (2010).
5. M. F. Craciun *et al.*, *Nat Nano* 4, 383 (2009).
6. Y.-M. Lin *et al.*, *Science* 327, 662 (2010).
7. M. Y. Han, B. Özyilmaz, Y. Zhang, P. Kim, *Physical Review Letters* 98, 206805 (2007).
8. Z. Chen, Y.-M. Lin, M. J. Rooks, P. Avouris, *Physica E: Low-dimensional Systems and Nanostructures* 40, 228 (2007).

9. X. L. Li, X. R. Wang, L. Zhang, S. W. Lee, H. J. Dai, *Science* 319, 1229 (Feb, 2008).
10. S. Y. Zhou *et al.*, *Nat Mater* 6, 770 (2007).
11. T. Ohta, A. Bostwick, T. Seyller, K. Horn, E. Rotenberg, *Science* 313, 951 (2006).
12. P. W. Sutter, J.-I. Flege, E. A. Sutter, *Nat Mater* 7, 406 (2008).
13. E. McCann, *Physical Review B* 74, 161403 (2006).
14. E. V. Castro *et al.*, *Physical Review Letters* 99, 216802 (2007).
15. J. B. Oostinga, H. B. Heersche, X. Liu, A. F. Morpurgo, L. M. K. Vandersypen, *Nat Mater* 7, 151 (2008).
16. Y. Zhang *et al.*, *Nature* 459, 820 (2009).
17. K. F. Mak, C. H. Lui, J. Shan, T. F. Heinz, *Physical Review Letters* 102, 256405 (2009).
18. F. Xia, D. B. Farmer, Y.-m. Lin, P. Avouris, *Nano Lett.* 10, 715 (2010).
19. C.-H. Park, S. G. Louie, *Nano Lett.* 10, 426 (2010).
20. J. Coraux, A. T. N`Diaye, C. Busse, T. Michely, *Nano Lett.* 8, 565 (2008).
21. K. S. Kim *et al.*, *Nature* 457, 706 (2009).
22. Y. Lee *et al.*, *Nano Lett.* 10, 490 (2010).
23. A. Reina *et al.*, *Nano Lett.* 9, 30 (2008).
24. X. Li *et al.*, *Science* 324, 1312 (June 5, 2009, 2009).
25. S. p. Berciaud, S. Ryu, L. E. Brus, T. F. Heinz, *Nano Lett.* 9, 346 (2008).
26. L. M. Malard, M. A. Pimenta, G. Dresselhaus, M. S. Dresselhaus, *Physics Reports* 473, 51 (2009).
27. A. C. Ferrari *et al.*, *Physical Review Letters* 97, 187401 (2006).
28. D. Graf *et al.*, *Nano Lett.* 7, 238 (2007).
29. A. Gupta, G. Chen, P. Joshi, S. Tadigadapa, Eklund, *Nano Lett.* 6, 2667 (2006).
30. Y. Hao *et al.*, *Small* 6, 195 (2010).
31. S. Horiuchi *et al.*, *Jpn. J. Appl. Phys.* 42, L1073 (2003).
32. J. C. Meyer *et al.*, *Solid State Commun.* 143, 101 (2007).
33. J. C. Meyer *et al.*, *Nature* 446, 60 (2007).
34. S. Bhaviripudi, X. Jia, M. S. Dresselhaus, J. Kong, *Nano Lett.*, null (2010).
35. Q. K. Yu *et al.*, *Appl. Phys. Lett.* 93, (Sep, 2008).
36. A. Reina *et al.*, *Nano Res.* 2, 509 (2009).
37. We note that the adhesion between metal electrodes and graphene is not perfect, resulting in metal peeling off. We also observed gate leakage/breakdown at high field for some devices. These devices are regarded as fabrication defects, as shown in Fig. 2.15a.

Chapter 3

Chiral transport in CVD bilayer graphene

3.1 Pseudospin of single layer graphene

The Hamiltonian of monolayer is two-dimensional analogues of the Dirac Hamiltonian for massless fermions. As a result, charge carriers in graphene have relativistic characteristics following the Dirac equation, which non-relativistic charge carriers following the Schrodinger equation do not have in other condensed matter systems (*1, 2*). An analogy between relativistic particles and electrons in graphene makes graphene an interesting platform in which various elusive quantum relativistic effects be tested in experimentally.

$$-i\hbar v_F \boldsymbol{\sigma} \cdot \boldsymbol{\nabla \Psi}(\boldsymbol{r}) = E\boldsymbol{\Psi}(\boldsymbol{r}) \qquad \textit{Equation 3-1}$$

The fundamental feature of this Dirac spectrum is the existence of an anti-particle with the same mass and opposite charge associated with the particle. In the graphene system, the anti-particle of electron is a positively charged electron, or called positron, which is often understood as a hole in solid-state physics. The Dirac equation, therefore, leads to the fact that states at positive (electrons) and negative (positrons, or, a hole in solid state physics) energies in graphene are intimately connected, showing a property analogous

to charge-conjugation symmetry in Quantum electrodynamics (QED) (*2-4*). Non-graphene systems, however, do not have this feature, as shown by separate Schrodinger's equations of electrons and holes respectively.

The formal similarity between graphene and QED is attributed to the fact that the two-component wave function description of quasi-particles in graphene is very much the same as the spinor-wave function in QED (*4, 6, 7*). The Dirac spinors in graphene consist of the components describing the distribution of electrons in two equivalent sublattice carbon atoms A and B, whereas spinors in QED are formed of real spin components. Because the role of the spins in QED is replaced by these sublattice atoms, it is common in graphene literature to regard the sublattice degree of freedom as a pseudospin, usually referred as σ, with A sublattice being 'up' pseudospin state, and B sublattice being 'down' pseudospin state (*2, 4, 8, 9*).

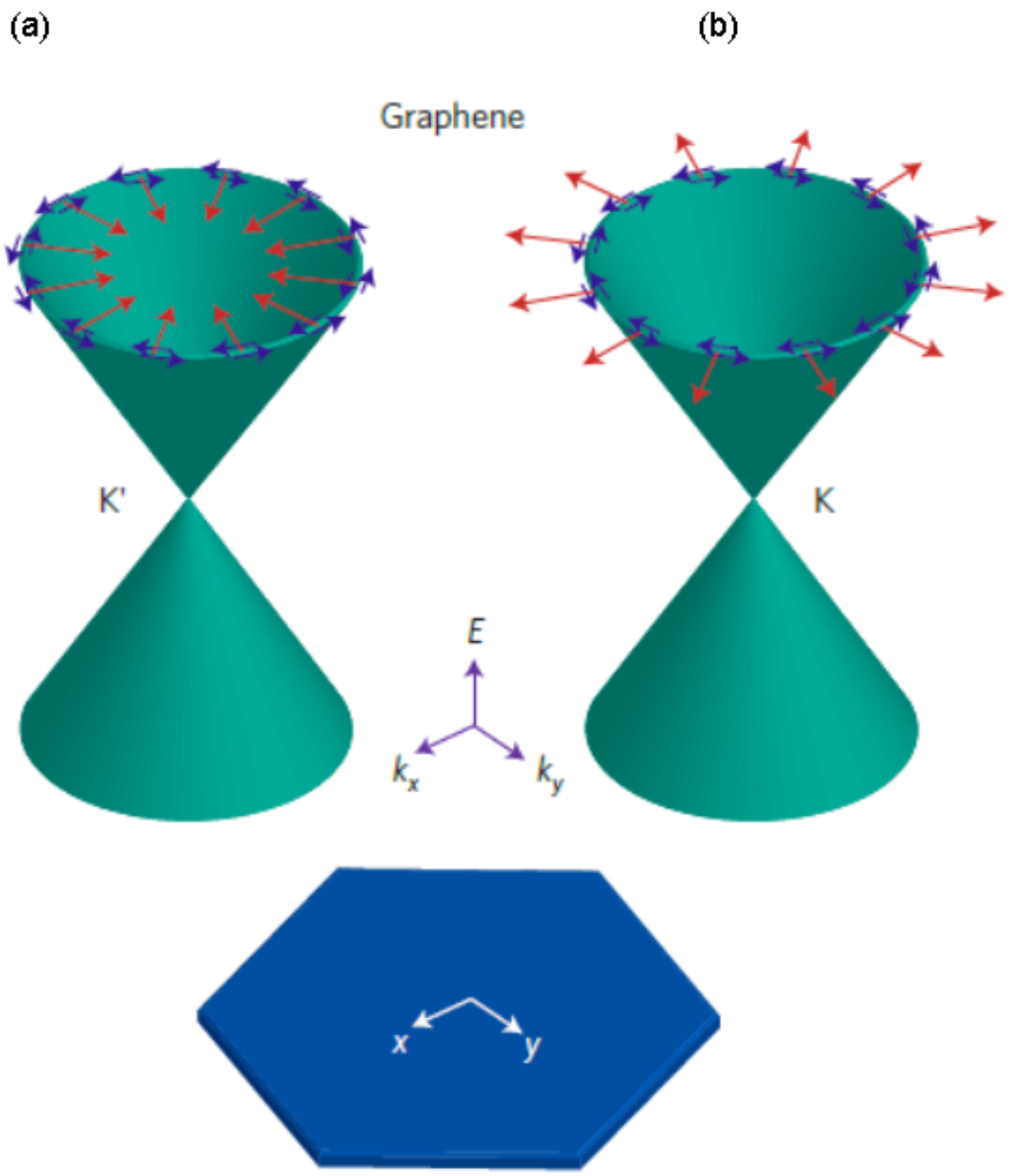

Figure 3.1 Electronic structure of graphene is represented with pseudospin and spin textures (red and blue arrows, respectively) Pseudospins of Dirac cones in (a) and in (b) are opposite correspondingly with labelled K and K'. Adapted from (*10*).

The existence of two equivalent sublattices A and B lead to the introduction of chirality in carrier dynamics in graphene. The chirality in graphene is defined as a projection of pseudospin σ on the direction of motion k, which is a quasi-particle momentum.

$$\boldsymbol{C} \equiv \frac{\boldsymbol{k}\cdot\boldsymbol{\sigma}}{k} \quad (\boldsymbol{C}\ is\ the\ chirality\ operator) \qquad \textit{Equation 3-2}$$

This chirality operator has its eigenvalues ±1, which give rise to the fact that the electron with energy E propagating positive direction has the same chirality with the hole with energy –E propagating negative direction (*2, 3, 11*).

3.2 Review of Klein tunneling in single layer graphene

3.2.1 Introduction of Klein paradox

Soon after the discovery of Dirac equation, Swedish physicist Oskar Klein obtained a surprising result when he calculated transmission probability of a relativistic electron going through a single potential barrier (*3, 12*). In non-relativistic particles, the probability of particle crossing over the potential barrier decays exponentially with the width and the height of the potential barrier. A particle can penetrate a classically forbidden region of space in the form of evanescent wave, which is referred to quantum tunneling. In sharp contrast, Klein's result showed that incident particle tunnels through the potential barrier via a propagation of its anti-particle state under the barrier, leading to the high tunneling probability regardless of barrier characteristics (*3, 11*). This Klein tunnel effect is clearly different from the usual quantum tunneling effect as the tunneling mechanism does not

depend on evanescent wave. This exotic behavior, known as a so-called Klein paradox, is now well understood, however, its experimental proof has been elusive due to the technological limitations in implementing experimental set-up for high-energy physics area (*3*).

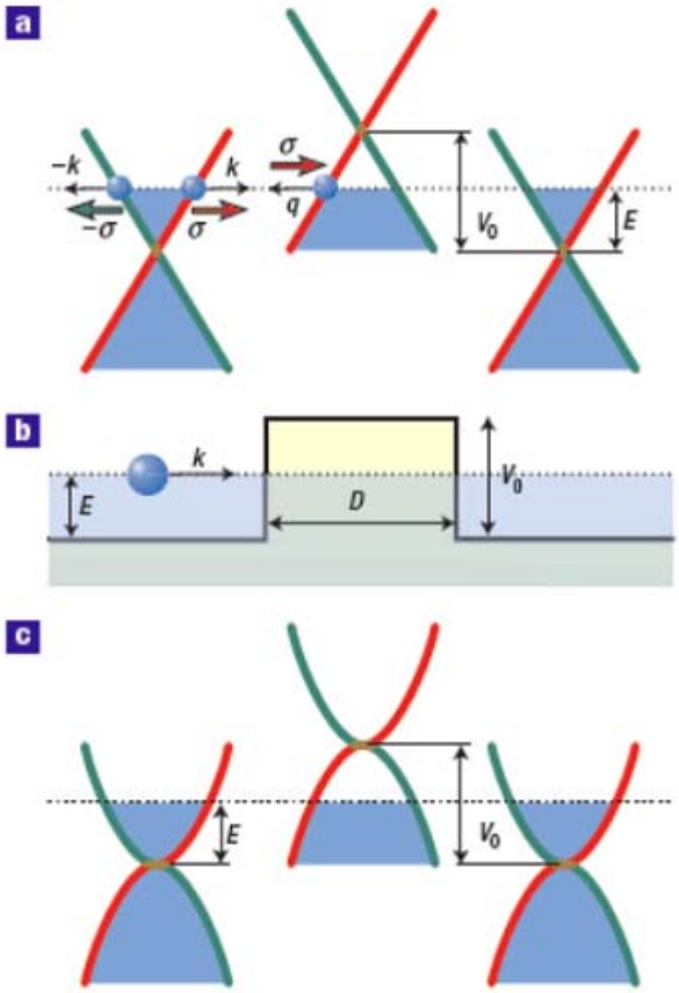

Figure 3.2 Tunneling through the potential barrier. Red and green color correspond to sublattices A and B in (a) single layer graphene, and in (c) bilayer graphene. (b) Potential barrier of height V_0 and width D. The pseudospin σ is parallel (antiparallel) to the direction of electrons (holes) motion. Adopted from (*3*).

3.2.2 Klein Tunneling in single layer graphene

The Klein paradox for massless Dirac fermions expects that low energy electron (massless Dirac fermion) injecting normal to a potential step perfectly transmits through the step regardless of its width and height. By creating potential step or potential barrier, anomalous tunneling of charge carriers could be tested experimentally exhibiting perfect transmission (*13, 14*).

Considerable experimental effort has been devoted to confirming a theoretically expected predictions (*13-16*). The observation of Klein tunneling relies heavily on sharp and clean interface between n-doped and p-doped region. Transport properties of p-n junction and n-p-n bipolar junction in early experiments showed disorder dominant transport characteristics. Electrons impinging on the p-n junction have a random distribution of incidence angle due to a scattering in diffusive graphene systems (*17*). By carefully comparing expected values of p-n junction resistance with that of experimental resistance values, experimental results from those diffusive graphene systems showed the existence of anomalous chiral tunneling indirectly (*13-15*).

More recent experiments have been successful to fabricate much cleaner graphene hetero-junction with high mobility by minimizing the influence of disorder such as using narrow bipolar junction structure (*5*). This electrostatically induced narrow potential barrier cause an interference pattern when the quantum mechanical waves of charge moves through the barrier. By applying magnetic field, the interference pattern acquires phase change associated with Berry phase, a direct evidence of Klein tunneling effect (*5, 18*).

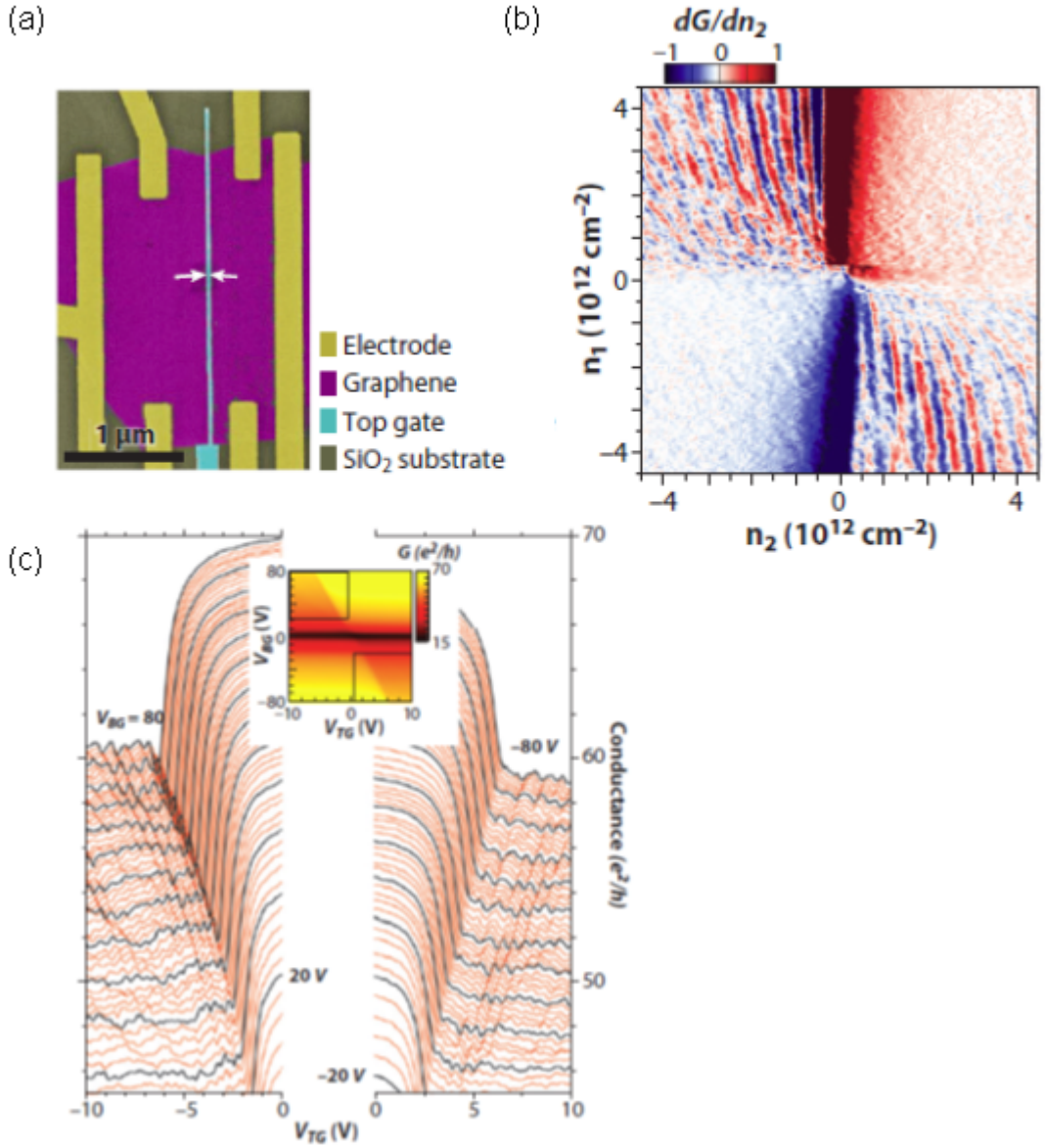

Figure 3.3 (a) SEM image of narrow top-gate graphene device (b) differential transconductance map as a function of carrier densities under the barrier (n2) and in the graphene lead (n1) (c) (Inset) Conductance map of the device. Conductance as a function of Vtg and Vbg along the line cut in Inset. Adopted from (5).

3.3 Pseudospin of Bilayer Graphene

The two dimensional charge carriers in bilayer graphene are described by massive chiral Hamiltonians (*1, 19-21*). This is a novel type of Hamiltonian, which is different both from Schrodinger Hamiltonians for a description of non-relativistic charge carriers in conventional 2-dimensional, 3-dimensional parabolic systems, and relativistic Dirac Hamiltonians for a description of relativistic charge carriers such as photons. The two-component Hamiltonian in bilayer graphene has also pseudospin degree of freedom as that of single layer graphene, meaning that charge carriers in bilayer graphene are also chiral. The solutions (spinor) of this Hamiltonian in bilayer graphene consist of the component of two contribution of electron density on sublattices A1, and B2, where A1 and B2 sublattice lie on different layers (*3*).

Quasi-particles in bilayer graphene are also chiral, but they have parabolic energy spectrum rather than linear spectrum as shown in Fig. 3.4. In other words, charge carriers in bilayer graphene are chiral, but not along the same manner as relativistic chiral carriers (in Fig. 3.5) (*22*). Indeed, bilayer graphene may provide a better opportunity to test chirality related features in comparison with monolayer graphene where chirality related and masslessness (relativistic characteristic) related effects are not clearly distinguishable (*3, 4, 20, 23, 24*).

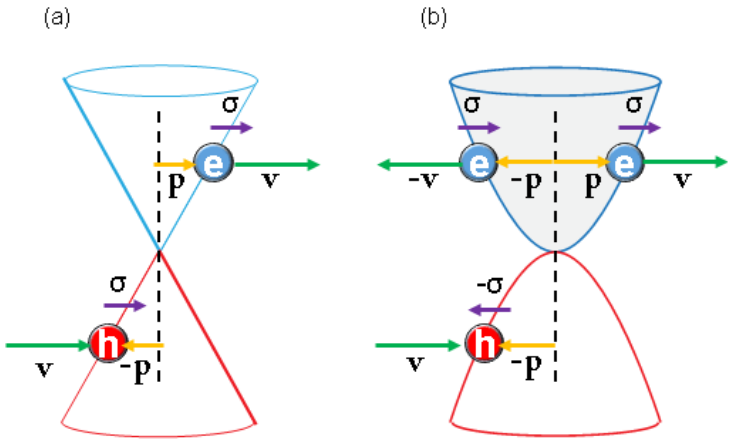

Figure 3.4 (a) The relationship between pseudospin and momentum in single layer graphene. The pseudospin points parallel (antiparallel) to the momentum of electron (hole) motion direction. v denotes velocity. (b) For a rotation of angle θ the momentum p, the pseudospin rotate 2θ in bilayer graphene. The pseudospin corresponds to band index (+1 for conduction band, -1 for valence band).

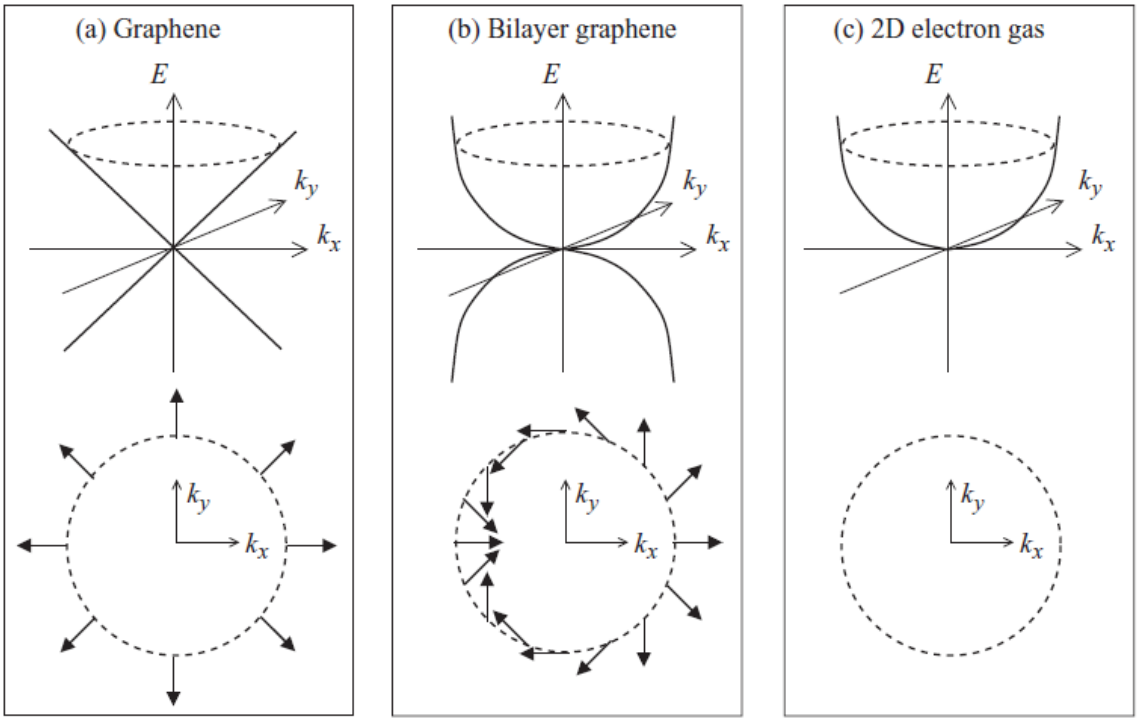

Figure 3.5 (Upper panel) Energy spectrum for (a) graphene, (b) bilayer graphene, and (c) 2D electron gas in conventional semiconductor materials. (Under panel) Solid arrow lines indicate pseudospin direction. Charge carriers in 2DEG have no pseudospin degree of freedom. Adopted from (*22*).

3.4 The electronic cloaking effect in bilayer graphene nanostructure

3.4.1 Motivation

In bilayer graphene, due to the parabolic energy spectrum, charge carriers are massive quasiparticles having a finite density of states at zero energy, like other non-relativistic charge carriers in conventional two dimensional materials. However, these quasiparticles are massive Dirac fermions that have a chiral nature similar to that of massless Dirac fermions in monolayer graphene. With the relativistic like character in monolayer graphene, coupling of motion of charge carrier and pseudospin via chirality has generated dramatic consequences such as an unusual quantum Hall effect, Klein tunneling, Veslago lens, etc (*3, 5, 19, 21, 25*). Because of non-relativistic character, massive Dirac fermions can provide an even better testbed to clarify the importance of chirality in transport measurement (*3*). However, experimental proof of their role was lacking and still remains to be demonstrated. Here we report electronic cloaking effect as a manifestation of chirality in transport by probing phase coherent transport behaviour in CVD bilayer graphene nanostructure (*23, 26*). With a Fourier analysis technique, we successfully analyse and identify the origin of each individual interference pattern in bipolar and monopolar regime. These findings may hold promise for the realization of pseudospintronics based on bilayer graphene.

Since the experimental observation of unconventional integer Hall effects was found due to Berry phase π arising from the chiral nature of electrons, chirality has been considered as holding a key role in understanding unusual transport behaviors of graphene

(*19, 21*). Combining with chirality relativistic-like character, Klein tunneling, as a surprising result of "absence of backscattering", has been theoretically predicted and experimentally tested including resistance measurements, and phase change detection from Fabry-Perot resonance (*3, 5, 13-18*). In the context of chirality, the novel integer quantum Hall effect via 2π Berry phase is undoubtedly unique because it indicates the presence of massive chiral quasiparticles with a parabolic dispersion (*20*). The case of chiral tunneling in BLG heterojunction would be even more interesting, where complete decoupling between quasiparticle states of opposite polarity has been expected theoretically at normal incidence due to chirality mismatch (*23, 27*). A striking consequence of chirality mismatch is a rendering confined states invisible via potential barrier from opposite pseudospin states – so called cloaking effect (*23*). However, experimentally proving this is still challenging.

3.4.2 Fabrication of double gated bilayer graphene transistor

The studied devices were fabricated from homogenous bilayer graphene film synthesized by CVD method. The BLG film was transferred onto a chip with 40nm Al2O3 deposited by ALD on top of a degenerately doped Si substrate, used as a global back gate. Contact to the BLG was made by standard e-beam lithography (Raith150), e-beam evaporator of a Pd/Au (5nm/25nm), and lift-off. To form the dielectric layer for the top gate, a thin layer of aluminium (2nm) was deposited and oxidized in the air three times. The top gate electrodes were defined by e-beam lithography, followed by Ti/Au (5nm/25nm). We prepared both single gated BLG device and dual gated BLG device in our experiment.

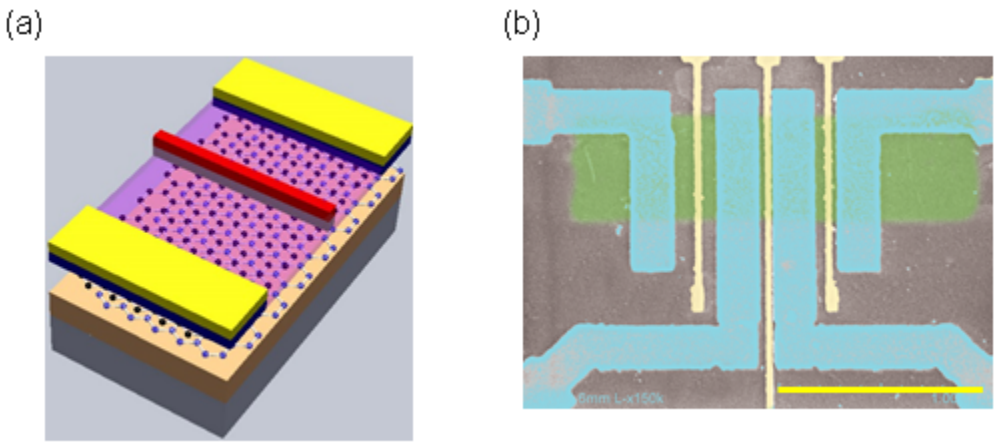

Figure 3.6 (a) Schematic diagram of bilayer graphene double gate structure. (b). False-color scanning electron microscopy image of BLG device having different channel lengths (200/100/50nm). Scale bar is 1um.

3.4.3 Cloaking effect in phase coherent transport of BLG nanostructure

Here, we resolve the chiral transport of massive Dirac fermions by probing the phase coherent transport behavior of dual gated BLG transistor. In contrast to earlier implementation of dual gated devices, which induce Fabry-Perot interference only inside of potential barrier, the dual gated BLG device described here allows a phase coherent transport regime over the full channel length by scaling down channel length to sub 200nm (Fig. 3.6) (*5, 28, 29*). This approach allows us to protect loss of phase information due to disorder when charge carriers traverse the BLG channel.

Figure 3.7 presents a schematic overview of possible chiral massive fermion trajectories contributing to the quantum oscillations. In the monopolar regime, graphene underneath metal contacts are doped by charge transfer from metals, and may have a different polarity from that of the channel region. The BLG device will then produce a

bipolar junction in the vicinity of source and drain, providing a resonance cavity (Fig. 3.7b) (*29*).

In more sophisticated way, the bipolar regime can offer an opportunity to unravel crucial role of chirality in transport through the potential barrier (Fig. 3.7a). Due to opposite chirality, hole and electron states can be localized simultaneously, as illustrated in schematics. More interestingly, chiral carriers could have additional possible route to complete a round trip between source and drain via quantum tunneling through the potential barrier. Hence, complex Fabry-Perot type interference might appear because of three different quasiparticle trajectories.

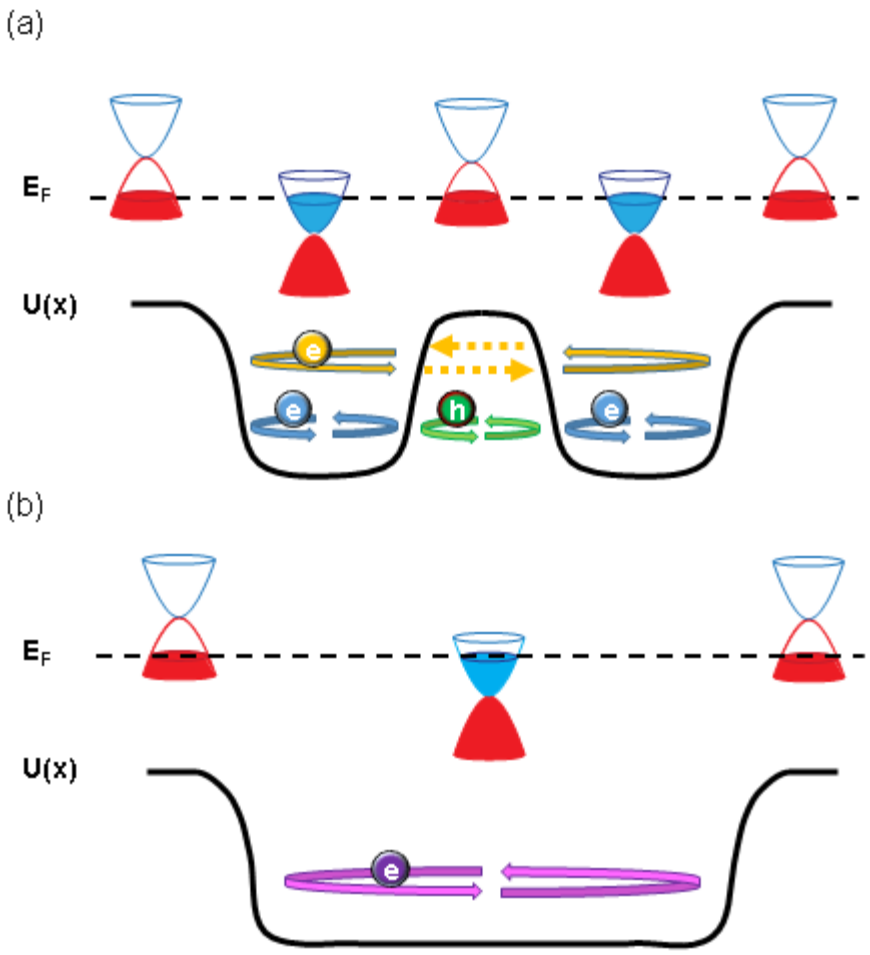

Figure 3.7 a. Schematic illustration of possible cloaking resonance conditions in bipolar npn junction due to decoupling of orthogonal pseudospins. Longest resonance cavity occur via direct tunneling through the barrier (Yellow color). Blue and green colored trajectories show resonance of confined states. b. FP resonance in monopolar regime occur due to reflection of source and drain contact.

3.4.4 Transport measurement of single gated bilayer graphene devices

We first characterize single-gated bilayer graphene devices via two terminal measurement at 6K. Figure 3.6b, c, and d show two dimensional differential conductance as a function of back-gate voltage (Vg) and bias voltage (Vc) for different channel length devices. For each images, smooth backgrounds are subtracted to enhance the quantum oscillation patterns. The channel lengths are 55nm, 118nm, 160nm respectively with fixed

width of 500nm as measured by scanning electron microscopy. The dips, marked by dark lines, in dI/dV evolves smoothly as Vg and Vc changes, showing chessboard patterns in all three maps exhibiting quasi-periodic oscillation. More importantly, Vc and Vg spacing between adjacent dark lines scales inversely with the square of the channel length (Fig. 3.6a). This behavior is quantified by bias voltage and oscillation period ΔVg : 21.08(±2)mV, 0.45(±0.02)V for the 55nm device; 5.1(±0.3)mV and 0.12(±0.02)V for the 118nm device; 3.1(±0.14)mV and 0.065(±0.02)V for the 160nm device (Fig. 3.8a). Whenever phase change obtained by round trip of an electron reaches 2π, a constructive interference pattern appears for $\Delta k_F = \pi/L$. Combining this condition with parabolic band dispersion of BLG gives,

$$E_F = \frac{\hbar^2 k^2}{2m^*} = \frac{\hbar^2 \pi C_g V}{2m^*} \qquad \text{Equation 3-3}$$

$$eV_C = \partial E_{F,peak} = \frac{\hbar^2 k \partial k}{m^*} = \frac{\hbar^2 k \pi}{m^* L} \qquad \text{Equation 3-4}$$

where m* is the effective mass having $0.03m_e$,and Cg is the gate capacitance of 175nF/cm^2 calculated from parallel plate capacitor model. With the bias voltage (21.08mV) and oscillation period (0.45V) from the differential conductance, the value of the estimated channel length can therefore be obtained approximately as 50nm, which fits well with physical length of 55nm. Testing other channel length devices also gives the values close to the actual physical lengths of themselves. This agreement leads us to the conclusion that our CVD bilayer graphene has Bernal stacking order, and that phase coherence length is larger than the 160nm of our BLG device. Note, however, that somewhat irregular

interference patterns are also shown, indicating that our BLG devices are non-ideal Fabry Perot resonators. It is mainly attributed to the fact that quasiparticle trajectories in 2D material are more complicated than that of 1D carbon nanotube wave guides.

Two dimensional $\partial I/\partial V$ plots of single gated device at 6K

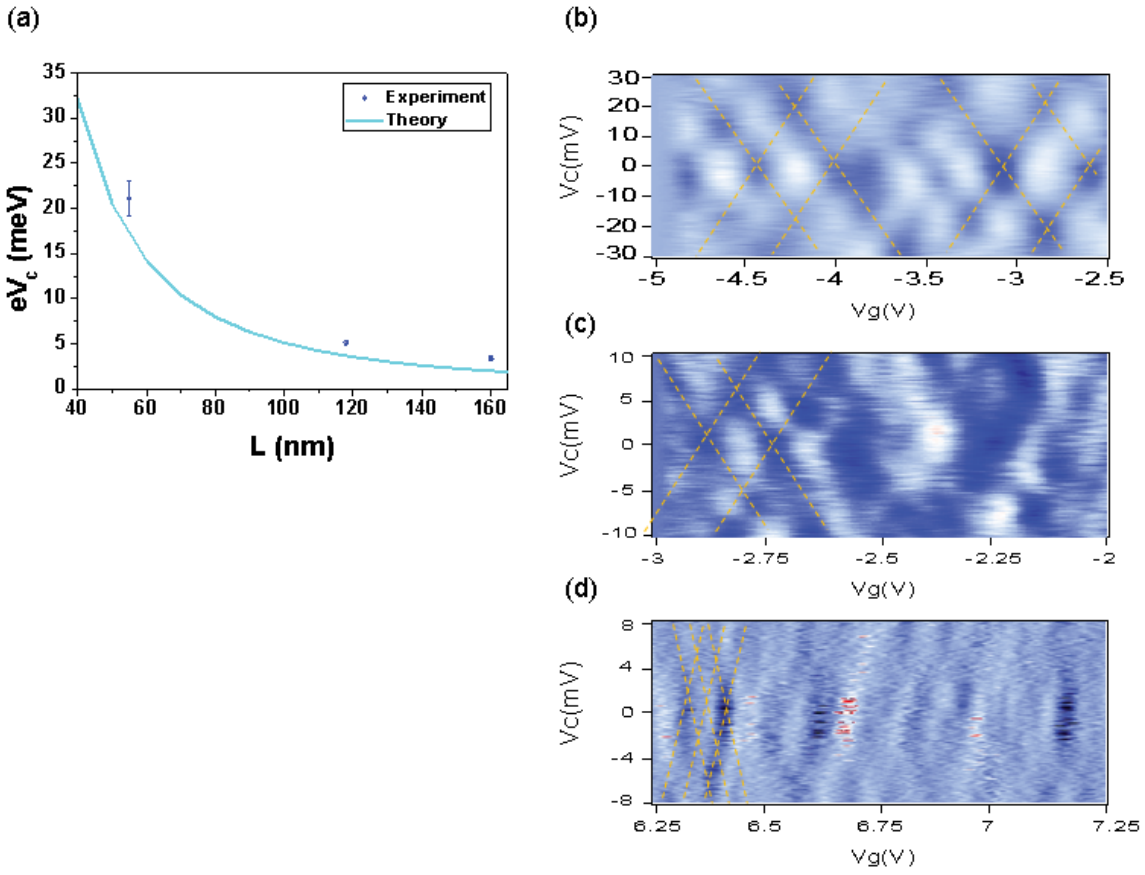

Figure 3.8 (a) Energy peak (E_F) and period (ΔV) from oscillation plotted against different channel length (55nm/118nm/160nm). (b), (c), (d). For each image, a smooth background was subtracted to highlight Fabry-Perot oscillation pattern. The dotted yellow lines in (b) guides to eyes to the bias voltage value (V_c) and oscillation periods (ΔV_g). $\boldsymbol{\partial I/\partial V}$ Conductance oscillations show peaks In (b), V_c = 21mV corresponding to 55nm. ; In(c), V_c = 5.1mV corresponding to 118nm.; In (d), Vc = 3.42mV corresponding to 160nm.

3.4.5 Transport measurement of double gated bilayer graphene devices

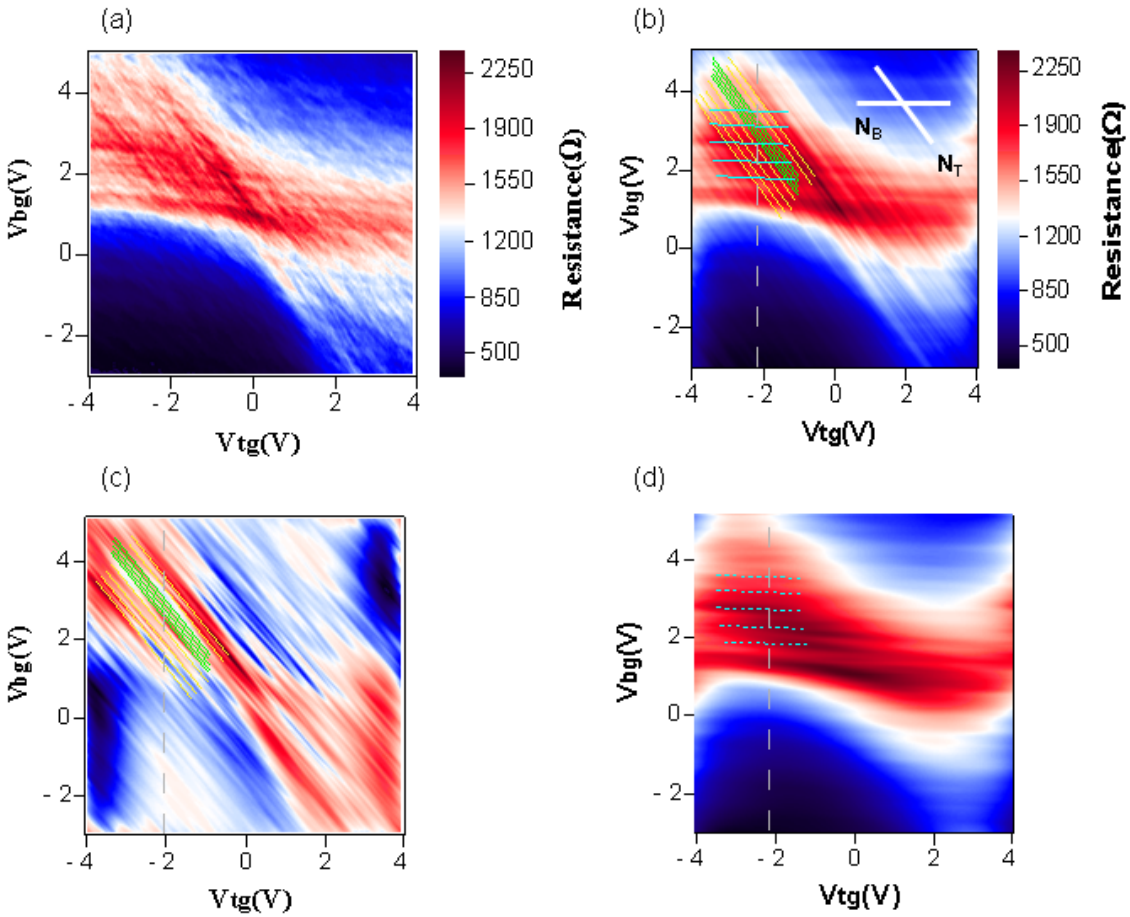

Figure 3.9 (a) Two terminal differential resistance R as a function of Vtg and Vbg for 150nm channel length device. (b). Sum of individual Fourier components of 2D resistance map. N_B and N_T label (white solid lines) represent two components of Fourier Transform masked to extract oscillations from graphene leads and the region inside of barrier respectively. 2D resistance map component masked along the direction (c) N_T, and (d) N_B. Color-coded lines along the grey dashed line link observed conductance oscillation in bipolar regime: blue lines for GL cavity, green lines for cavity defined by inside of barrier, Yellow lines for full channel length cavity in bipolar regime.

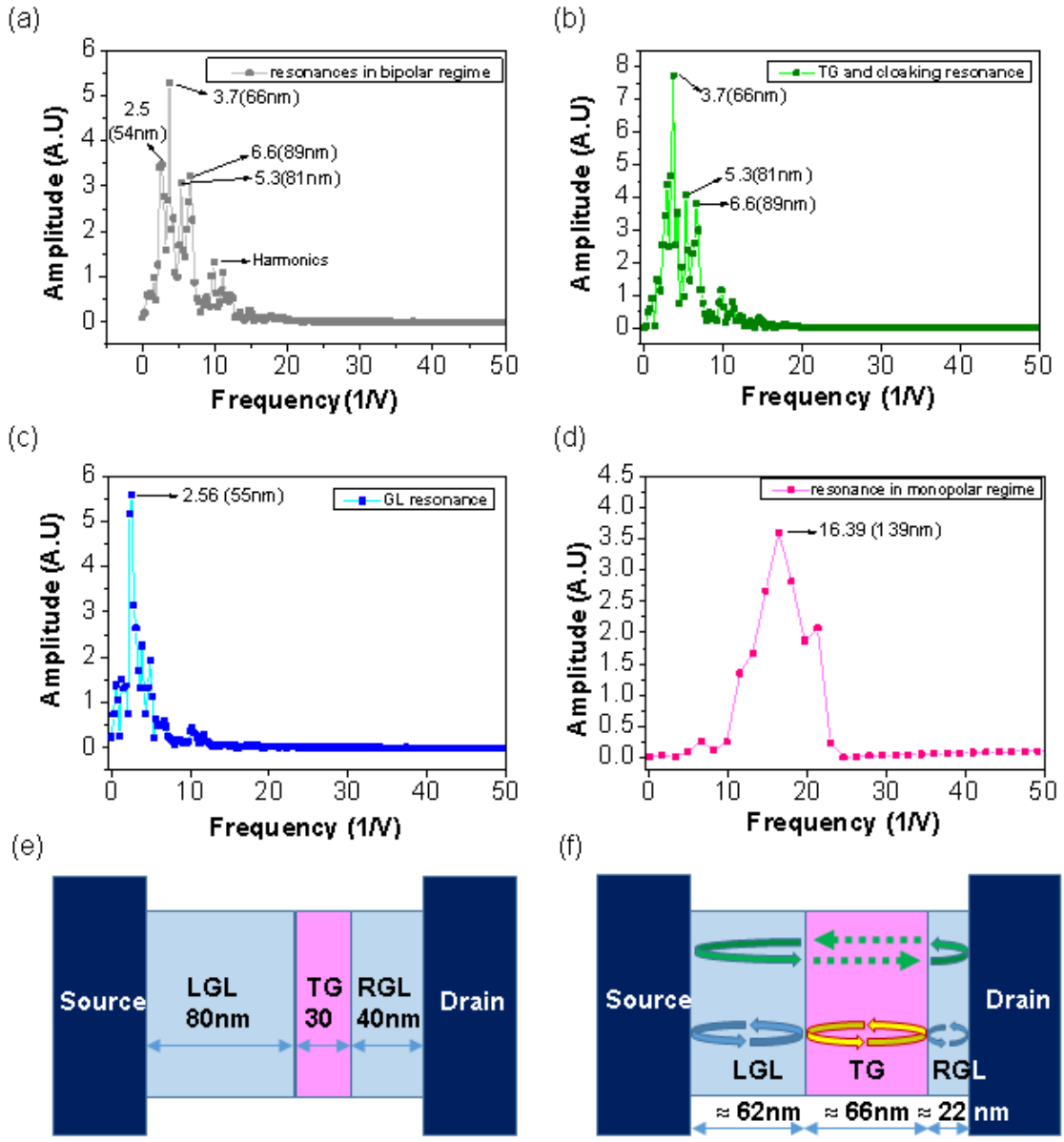

Figure 3.10 Fourier transform spectra from the 150nm channel length device data of oscillations along the gray dashed line (a) from Fig 3. (b), (b) from Fig3.(c), (c) from Fig.3(d) in the monopolar regime, (d) in the monopolar regime. (e) Schematic diagram of physical design of left graphene lead (LGL) /top-gate (TG)/ right graphe lead (RGL) along the BLG channel. (f) Schematic diagram of estamated effective resonance cavity along the BLG channel.

To experimentally test theoretically proposed anomalous tunneling behavior, we required a heterojunction in BLG under the phase coherent transport regime. To achieve this goal, we studied a BLG device integrated with global back gate and local top gate. As

the voltages applied to local top gate and global back gate are tuned independently, carrier densities underneath the top gate and in the graphene leads can be controlled to form the monopolar and the bipolar regimes, respectively. By scaling down the channel length to sub 150nm, electrons and holes remain phase coherent as confirmed by single-gated BLG devices with similar dimensions.

We now focus on the transport measurement of our dual-gate BLG devices, starting with a 150nm channel length device. Two dimensional differential resistance is plotted as a function of back-gate and top-gate voltage. Figure.3.9a exhibits four quadrants of monopolar and bipolar regimes corresponding to the polarity configuration. The slope of charge neutral line gives capacitive coupling ratio between top gate and back gate, Ctg/Cbg ~1.7. A rich set of oscillating features is observed in our differential resistance map; one interference pattern in the monopolar regime, and more than two fringes forming checkerboard like complex interference patterns in the bipolar regime, shown in Fig. 3.9a. In order to establish the origin of resonances, characterizing them quantitatively as well as qualitatively is also important. However, analyzing beating patterns caused by more than two resonating signals is highly non-trivial and challenging.

To obtain a better insight into the transport mechanism, we employ a 2D Fourier analysis technique for complicated interference patterns (*30*). The main role of FFT is to separate fringes patterns affected by different combinations of top and back gate voltage along the horizontal (N_B) and diagonal (N_T) orientations (see Appendix A). By masking one fringe pattern and performing inverse FFT on the other fringe patterns, we can clarify the presence of two different fringe components along each orientation (Fig. 3.9c, 3.9d).

The summation of these separated fringe patterns recovers the original 2D differential resistance map with more pronounced interference patterns (Fig. 3.9b).

The FFT processed data sets enable us to better understand observed interference patterns. Resonances attributed to the effect of both double gates are clearly seen along the N_T orientation in Fig. 3.9c. On closer inspection, sequences of periodic oscillations are observed at Vtg = -2.1V along the dashed line in the monopolar regime. The FFT determines a quantitative verification of the dominant period, showing a peak frequency at 16.39(1/V), corresponding to oscillation period of ΔVbg~0.06V in monopolar regime. Using equation 3 - 4, this value gives the BLG resonator a cavity length of~ 138nm which matches physical length of the cavity between two electrodes (150nm).

With oscillations in the bipolar regime, our system enters a phase-coherent regime where the condition for Fabry-Perot type of quantum interference can be realized and conductance across the potential barrier exhibits the characteristic set of oscillations associated with Klein effect in BLG. This checker-board pattern visible along the dashed grey line in Fig. 3.9a is a manifestation of interferences from resonant cavities formed by the potential barrier and two electrodes; an observation confirmed by the Fourier Transform which shows three peak values corresponding to an oscillation periods of 0.27V, 0.39V, and 0.168V.

To identify the origin of these oscillations, we now concentrate on the nature of conductance oscillations tuned by both top- and back-gate by applying the FFT technique with masking horizontal streaks shown in Fig. 3.9c. The fast Fourier transform analysis of the beating oscillation trace along the grey dashed line yields three primary oscillation periods of 0.27V, and 0.152V, 0.188V, which correspond to effective cavity length of

66nm, and 81nm, 89nm, respectively. The cavity length of 66nm is in reasonable agreement with the fabricated top-gate width of 33nm, taking into account of smooth potential profile due to the distance to the top-gate from the BLG by a thin dielectric layer of approximately 10nm (Fig. 3.10e and Fig 3.10f). This indicates the existence of localized state confined by a potential barrier. The second and third peaks of the Fourier transform spectra, corresponding cavity sizes of 81nm, 89nm, show a more interesting behavior of massive quasiparticles. The resonant condition for these cavities immediately invites one to consider electrons bouncing back and forth between top-gate and metal electrodes: confined states either from the left or right BLG lead region. However, we rule out this possibility both because density of carriers localized in BLG lead can only be tuned by back-gate voltage, and because the size of the effective cavity (81~89nm) is also larger than the averaged the left and right BLG leads length (~60nm).

Our proposed scheme for a more plausible explanation is the fact that plane waves, either on left and right side of potential barriers, are coupled through the evanescent waves inside the barrier, as if there are no available states under the barrier, owing to a pseudospin mismatch of opposite polarity, referred as an electronic cloaking effect, visualized in Fig.3.9a with yellow color-coded lines.

Thus, the distance over which quasiparticles propagate without any loss of phase information via quantum tunneling consists of two segments: both left and right BLG lead regions, whose size are equal to full-channel length other than potential barrier width (in Fig 3.10f). Indeed, the value of full channel length (~150nm) approximately equals the summation of the effective length of the top-gate (~66nm) and the quasiparticle

propagation distance (81~89nm), as obtained from the Fourier transform analysis of conductance oscillations parallel to N_T orientation (shown in Fig. 3.9c).

To investigate oscillations along N_B direction, we follow the FFT procedure with masking diagonal streaks such that oscillation affected only by back-gate should be shown to originate from Fabry-Perot interference due to the resonance cavity defined by the BLG lead. The Fourier transform spectra taken from the data along the dashed line in Fig.3 c show a measured oscillation period of 0.39V, corresponding to an effective cavity length of 55nm. Considering our physical length of left BLG lead as approximately 62nm due to the effective top gate cavity size of 66nm, this value indicates that a significant fraction of incident waves are reflected at the interface of the p-n junction due to chirality mismatch, which is associated with the anti-Klein tunneling effect in BLG. However, quantum interference expected to be occurred in approximately 22nm size of right BLG lead is not observed because oscillation period seems to be beyond our detection limit, ~ 2V, in terms of back-gate voltage.

These clearly distinct set of oscillations (arising from confined states under potential barrier and from the round trip of carriers across full-channel length via quantum tunneling, together with localized states in BLG lead), could be understood in the context of pseudospin conservation in BLG. In accordance with proposed all possible resonance scenario in the bipolar regime, we may interpret an anomalous interference of coupled states via evanescent waves to indicate an electronic cloaking effect. However, we should verify this conclusion by testing a few more BLG devices with different channel length to rule out other possible explanations. The two similar cavity lengths of 81nm and 89nm, originating from a cloaking effect, may attribute their small discrepancy again to the change of the smooth potential barrier profile.

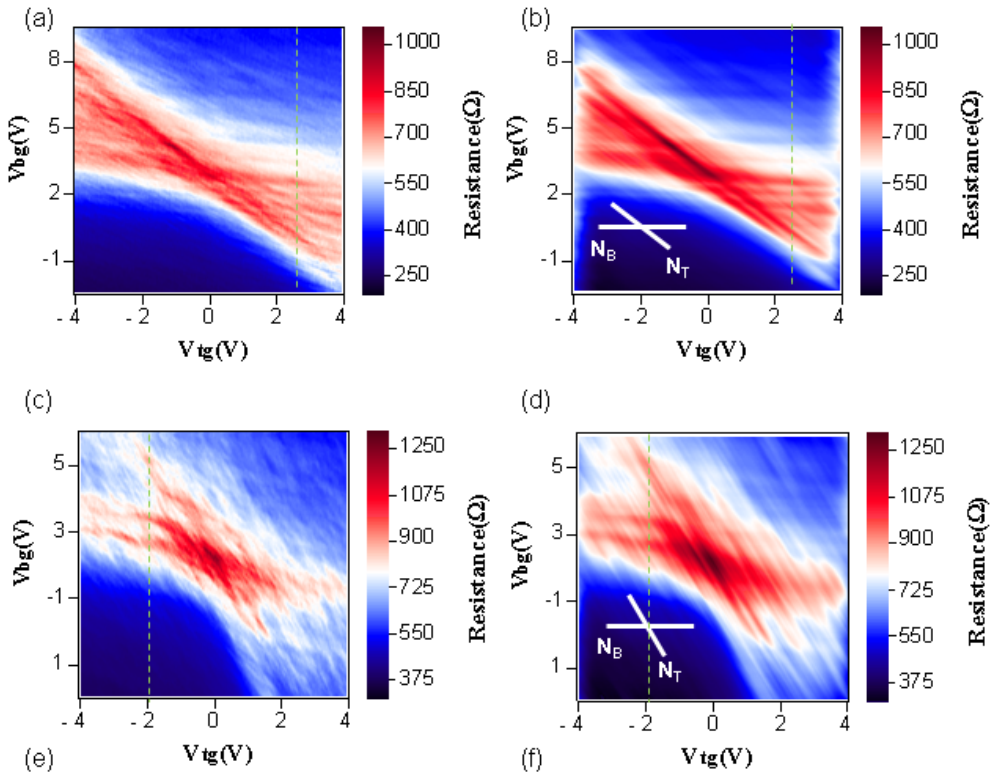

Region 100nm	ΔVbg(V) (measured)	Frequency (FFT)	Length(nm) (Calculated)
TG	0.5	1.99	48nm
GL	0.73	1.365	40nm
cloaking	0.3	3.24	63nm
Full cavity	0.10	9.29	105nm

Region 120nm	ΔVbg(V) (measured)	Frequency (FFT)	Length(nm) (Calculated)
TG	0.427	2.34	52.6nm
GL	0.49	2.05	49nm
cloaking	0.197	5.13	78nm
Full cavity	0.091	10.97	114nm

Figure 3.11 (a) Two dimensional Resistance map of 120nm. (b) FFT processed resistance map of 120nm (c) Two dimensional Resistance map of 100nm (b) FFT processed resistance map of 100nm (e) Fourier spectra results from the oscillation along Vtg=2.6V in 120nm channel device (f) Fourier spectra results from the oscillation along Vtg=-1.9V in 100nm channel device.

Figure 3.11b shows FFT processed two dimensional dI/dV maps for channel length of 120nm device with top gate width (~27nm). When we examine the Fourier transform spectra along the dashed line trace at Vtg=2.6V after masking horizontal streaks and diagonal streaks, we observe one peak in monopolar regime, and three distinct set of peaks in the bipolar regime, corresponding to superimposed quantum oscillations linked with color-coded solid lines in two dimensional resistance map. The oscillation period (0.09V) of the peak value(10.97 [1/V]) in the monopolar regime gives the effective cavity length of 114nm, consistent with length of full-channel length. With masking diagonal streaks in the bipolar regime, the principal peak corresponding an oscillation period of 0.49V reveals localized states in the BLG lead with resonant cavity length of 49nm, in good agreement with averaged physical length of BLG leads as approximately 56nm. The physical length of right BLG lead is 20nm, and thereby resonance occurred in this region is beyond what can be detected by oscillation period in terms of back-gate voltage. After masking horizontal streaks, the peaks of frequency spectra of Fourier transform on oscillatory feature along Vtg=2.6V, 2.05[1/V] and 5.13[1/V], are used to extract resonant cavity sizes of conductance oscillations as approximately 53nm, 78nm, respectively. Remarkably, the addition of two cavity lengths, 131nm is close to the full-channel length of 120nm, as shown in 150nm length BLG device. We ascribe these observations to the cloaking effect of confined states by potential barrier, which makes them invisible for near normally incident waves outside the barrier to transmit through the barrier due to decoupling of opposite chirality. This possible interpretation of our data are further confirmed by FFT

processed resistance map of 100nm channel length device, and the results from Fourier analysis on oscillatory features are summarized in the table (Fig. 3.11e, 3.11f). This signifies that interference of quantum mechanical paths depends on the chirality and momentum parallel to the barrier in BLG. After analysis of three different devices, the proposed scenario of chiral transport in our BLG devices can be considered a routine.

Energy of carriers confined in various cavities in bipolar and monopolar regime

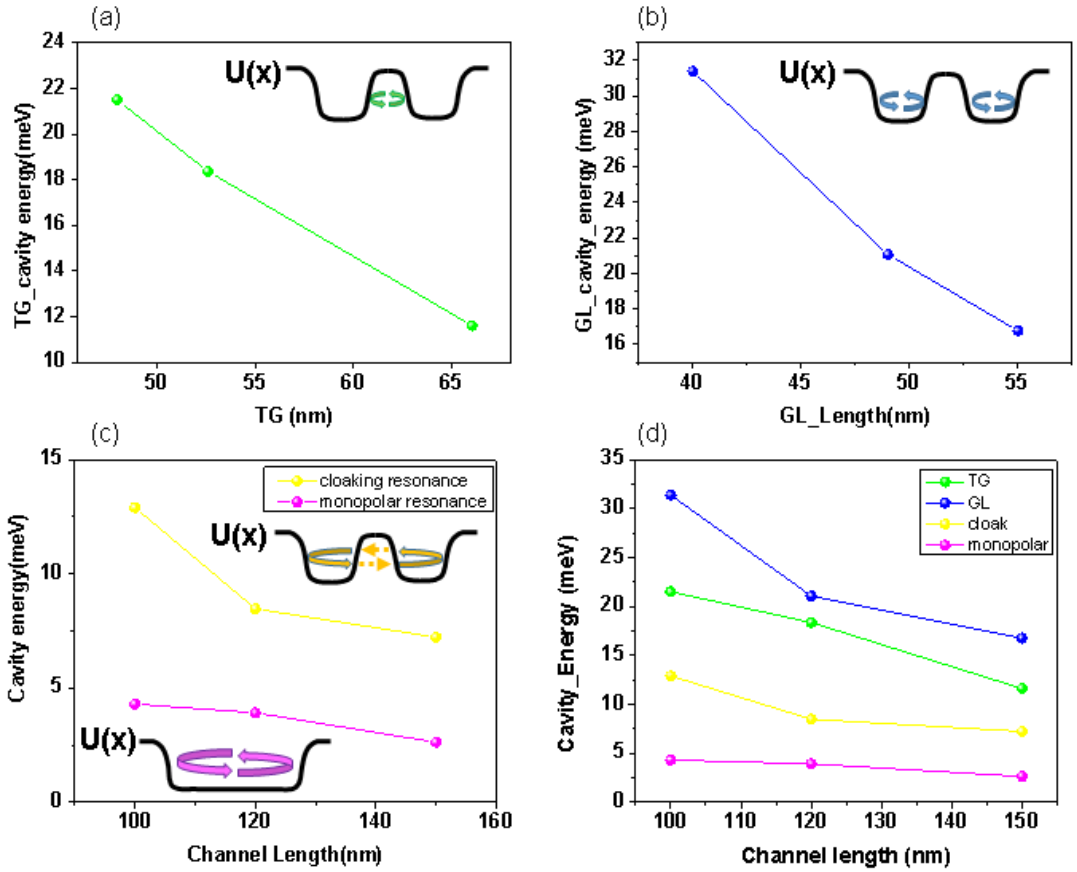

Figure 3.12 Energy of carrier confined in (a) inside and (b) outside of potential barrier in bipolar regime with schematic diagrams (inset). c. Resonance of yellow and pink lines are corresponding to cloaking cavity in bipolar and full channel length monopolar regime, respectively. These results give hint of observation of cloaking effect in bipolar regime due to pseudospin mismatch in BLG device.

3.4.6 Conclusion

We also discuss measured effective cavity length versus physically designed length in three possible resonant spaces. After physical dimension of top-gate and BLG channel were measured by SEM, the length of BLG lead was obtained by an averaged value of parts of BLG channel, which are uncovered by top-gate. As is evident from a comparison of Fig.3.12a and Fig.3.12b, scaling of effective cavity lengths are well pronounced for localized states in BLG lead, and coupled electron states across a tunneling barrier. These experimental results strongly supports our scenario shown in Fig.3.7a, which describes quasiparticle trajectories, showing an important role of chirality in transport. Even though there should be no distinct difference in cavity sizes for localized states under the barrier because of similar dimension ~30nm, we observe that the cavity length gets smaller as the distance between source and drain gets short (Fig.3.12a). Strong source of this phenomena may be an increased charge screening effect from electrodes by aggressive scaling down to 100nm, which is also responsible for lack of appreciable band-gap opening in our device. Here, we demonstrate electronic cloaking effect by virtue of complete decoupling of states in opposite polarity, by probing phase-coherent transport behavior in our CVD BLG devices. Based on this findings, we may utilize chiral dependent transport properties to encode the information using pseudospins of massive fermions in BLG device. This may pave the way for future applications for pseudo-spintronics with bilayer graphene.

References

1. K. S. Novoselov, A. K. Geim, S. V. Morozov, D. Jiang, M. I. Katsnelson, I. V. Grigorieva, S. V. Dubonos, A. A. Firsov, Two-dimensional gas of massless Dirac fermions in graphene. *Nature* **438**, 197-200 (2005).
2. T. Ando, T. Nakanishi, R. Saito, Berry's Phase and Absence of Back Scattering in Carbon Nanotubes. *Journal of the Physical Society of Japan* **67**, 2857-2862 (1998); published online Epub1998/08/15 (10.1143/JPSJ.67.2857).
3. M. I. Katsnelson, K. S. Novoselov, A. K. Geim, Chiral tunnelling and the Klein paradox in graphene. *Nat Phys* **2**, 620-625 (2006); published online Epub09//print (http://www.nature.com/nphys/journal/v2/n9/suppinfo/nphys384_S1.html).
4. A. K. Geim, K. S. Novoselov, The rise of graphene. *Nat Mater* **6**, 183-191 (2007).
5. A. F. Young, P. Kim, Quantum interference and Klein tunnelling in graphene heterojunctions. *Nat Phys* **5**, 222-226 (2009); published online Epub03//print (http://www.nature.com/nphys/journal/v5/n3/suppinfo/nphys1198_S1.html).
6. S. Das Sarma, S. Adam, E. H. Hwang, E. Rossi, Electronic transport in two-dimensional graphene. *Reviews of Modern Physics* **83**, 407-470 (2011); published online Epub05/16/ (
7. T. Tudorovskiy, K. J. A. Reijnders, M. I. Katsnelson, Chiral tunneling in single-layer and bilayer graphene. *Physica Scripta* **2012**, 014010 (2012).
8. D. Pesin, A. H. MacDonald, Spintronics and pseudospintronics in graphene and topological insulators. *Nat Mater* **11**, 409-416 (2012); published online Epub05//print (
9. A. H. Castro Neto, F. Guinea, N. M. R. Peres, K. S. Novoselov, A. K. Geim, The electronic properties of graphene. *Reviews of Modern Physics* **81**, 109-162 (2009); published online Epub01/14/ (
10. E. Rotenberg, Topological insulators: The dirt on topology. *Nat Phys* **7**, 8-10 (2011); published online Epub01//print (
11. P. E. Allain, J. N. Fuchs, Klein tunneling in graphene: optics with massless electrons. *Eur. Phys. J. B* **83**, 301-317 (2011); published online Epub2011/10/01 (10.1140/epjb/e2011-20351-3).
12. A. F. Young, P. Kim, Electronic Transport in Graphene Heterostructures. *Annual Review of Condensed Matter Physics* **2**, 101-120 (2011)doi:10.1146/annurev-conmatphys-062910-140458).
13. B. Huard, J. A. Sulpizio, N. Stander, K. Todd, B. Yang, D. Goldhaber-Gordon, Transport Measurements Across a Tunable Potential Barrier in Graphene. *Physical Review Letters* **98**, 236803 (2007).
14. R. V. Gorbachev, A. S. Mayorov, A. K. Savchenko, D. W. Horsell, F. Guinea, Conductance of p-n-p Graphene Structures with “Air-Bridge” Top Gates. *Nano*

Letters **8**, 1995-1999 (2008); published online Epub2008/07/01 (10.1021/nl801059v).
15. N. Stander, B. Huard, D. Goldhaber-Gordon, Evidence for Klein Tunneling in Graphene p-n Junctions. *Physical Review Letters* **102**, 026807 (2009).
16. P. Rickhaus, R. Maurand, M.-H. Liu, M. Weiss, K. Richter, C. Schönenberger, Ballistic interferences in suspended graphene. *Nat Commun* **4**, (2013)10.1038/ncomms3342).
17. V. V. Cheianov, V. I. Fal'ko, Selective transmission of Dirac electrons and ballistic magnetoresistance of n-p junctions in graphene. *Physical Review B* **74**, 041403 (2006).
18. A. V. Shytov, M. S. Rudner, L. S. Levitov, Klein Backscattering and Fabry-Pérot Interference in Graphene Heterojunctions. *Physical Review Letters* **101**, 156804 (2008).
19. Y. Zhang, Y.-W. Tan, H. L. Stormer, P. Kim, Experimental observation of the quantum Hall effect and Berry's phase in graphene. *Nature* **438**, 201-204 (2005)http://www.nature.com/nature/journal/v438/n7065/suppinfo/nature04235_S1.html).
20. K. S. Novoselov, E. McCann, S. V. Morozov, V. I. Fal/'ko, M. I. Katsnelson, U. Zeitler, D. Jiang, F. Schedin, A. K. Geim, Unconventional quantum Hall effect and Berry/'s phase of 2[pi] in bilayer graphene. *Nat Phys* **2**, 177-180 (2006); published online Epub03//print (http://www.nature.com/nphys/journal/v2/n3/suppinfo/nphys245_S1.html).
21. K. S. Novoselov, Z. Jiang, Y. Zhang, S. V. Morozov, H. L. Stormer, U. Zeitler, J. C. Maan, G. S. Boebinger, P. Kim, A. K. Geim, Room-Temperature Quantum Hall Effect in Graphene. *Science* **315**, 1379 (2007); published online EpubMarch 9, 2007 (10.1126/science.1137201).
22. C.-H. Park, N. Marzari, Berry phase and pseudospin winding number in bilayer graphene. *Physical Review B* **84**, 205440 (2011); published online Epub11/18/ (
23. N. Gu, M. Rudner, L. Levitov, Chirality-Assisted Electronic Cloaking of Confined States in Bilayer Graphene. *Physical Review Letters* **107**, 156603 (2011).
24. S. Park, H. S. Sim, Bilayer Graphene Interferometry: Phase Jump and Wave Collimation. *Physical Review Letters* **103**, 196802 (2009).
25. V. V. Cheianov, V. Fal'ko, B. L. Altshuler, The Focusing of Electron Flow and a Veselago Lens in Graphene p-n Junctions. *Science* **315**, 1252-1255 (2007); published online EpubMarch 2, 2007 (10.1126/science.1138020).
26. S. Lee, K. Lee, Z. Zhong, Wafer Scale Homogeneous Bilayer Graphene Films by Chemical Vapor Deposition. *Nano Letters* **10**, 4702-4707 (2010); published online Epub2010/11/10 (10.1021/nl1029978).
27. S. Park, H. S. Sim, π Berry phase and Veselago lens in a bilayer graphene np junction. *Physical Review B* **84**, 235432 (2011).
28. L. C. Campos, A. F. Young, K. Surakitbovorn, K. Watanabe, T. Taniguchi, P. Jarillo-Herrero, Quantum and classical confinement of resonant states in a trilayer graphene Fabry-Pérot interferometer. *Nat Commun* **3**, 1239 (2012)http://www.nature.com/ncomms/journal/v3/n12/suppinfo/ncomms2243_S1.html).

29. Y. Wu, V. Perebeinos, Y.-m. Lin, T. Low, F. Xia, P. Avouris, Quantum Behavior of Graphene Transistors near the Scaling Limit. *Nano Letters* **12**, 1417-1423 (2012); published online Epub2012/03/14 (10.1021/nl204088b).
30. N. M. Gabor, J. C. W. Song, Q. Ma, N. L. Nair, T. Taychatanapat, K. Watanabe, T. Taniguchi, L. S. Levitov, P. Jarillo-Herrero, Hot Carrier–Assisted Intrinsic Photoresponse in Graphene. *Science* **334**, 648-652 (2011); published online EpubNovember 4, 2011 (10.1126/science.1211384).

Chapter 4

Coulomb blockade in monolayer MoS_2 single electron transistor

4.1 Introduction

4.1.1 Promising potential of 2D TMDC materials

Atomically thin 2D semiconducting TMDC materials have garnered much interest recently because of their unique optical and electronic properties. For example, these materials show a transition from indirect bandgap in multilayers to direct bandgap in a monolayer (*1, 2*), which opens up many possibilities in optoelectronics. Similarly, the manipulation of valley degrees of freedom was demonstrated in 2D materials by optical pumping through valley-selective circularly polarized light, thus exploiting the valley as carrying information (*3-6*). The lack of inversion symmetry in monolayer MoS_2 and other TMDC materials leads to a very strong spin-orbit coupling (*7*), making these materials promising for realizing spintronic device. These remarkable features may open a whole new field of rich physics in electron transport of 2D TMDCs such as coupling of spin and valley physics (*8, 9*), valleytronics (*6*), and quantum-spin-hall (QSH) effect based devices (*8, 10*).

Moreover, planar 2D nanomaterials have also great potential for ultra-small sized electronic components due to large surface-to-volume ratio and compatibility with existing CMOS technology. Graphene, the first example of a truly two dimensional materials, has been considered as a strong candidate for post-silicon electronics due to its interesting properties e.g. exceptionally high charge carrier mobility, up to $10^6 cm^2/Vs$ (*11*), and the long ballistic transport distance, ~ 1μm, even at room temperature (*12*). However, the absence of bandgap in graphene limits its possible applications in digital logic electronics (*13-16*). Hence, the focus has been shifted from studying graphene as a viable channel materials to the use of other promising 2D materials over the last few years (*17, 18*). In contrast, thin layer transition metal dichalcogenides (TMDCs) are semiconductors with a sizeable bandgap energy, around 1~2eV, which enables field effect transistors (FETs) with a high on/off ratio of $\sim 10^8$, and low subthreshold swings (74mV/dec) (*18*), and hence, are much better suited for applications in conventional electronics.

4.1.2 Efforts towards enhancement of carrier mobility in MoS_2 FET

Consequently, significant efforts have been devoted to electron transport studies at room temperature, but mostly limited to the electrical performance of field-effect-transistors based on 2D TMDCs (*18-21*). The mobility of the device made out of monolayer molybdenum disulphide (MoS_2) with a back-gate configuration was reported in the range of 0.1~1 $cm^2V^{-1}s^{-1}$ at room temperature (*18*), which is too low for practical applications despite its high on/off ratio and low subthreshold swing. However, earlier reports of low mobility values were underestimated from a two-terminal measurement scheme due to inclusion of contact resistance. Experimental studies towards the improvement of carrier

mobility in mono- or bilayer- MoS_2 FETs have been successfully done by encapsulating the device with high-k dielectrics (>200 $cm^2V^{-1}s^{-1}$) (*18*), and by vacuum annealing of the device with four terminal measurement configuration, showing μ ~1000 $cm^2V^{-1}s^{-1}$ at 4K close to intrinsic mobility value (*14, 22, 23*).

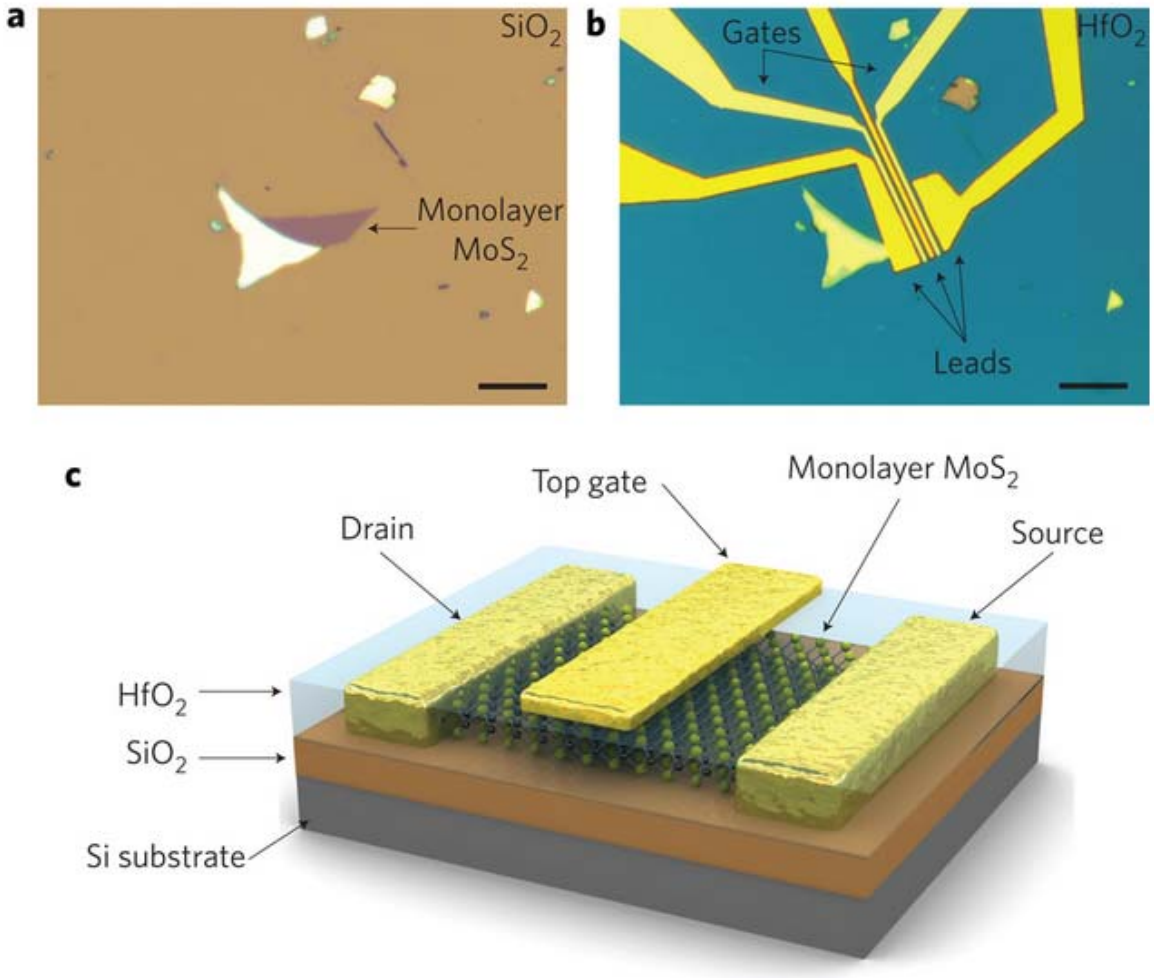

Figure 4.1 Monolayer MoS_2 double gated transistor (a) optical image of single layer MoS_2 deposited onto 270nm thick SiO_2. (b) Top view of MoS_2 transistor using 30nm HfO_2 as a gate dielectric for top-gates (c) Schematic diagram of MoS_2 transistor. Adopted from (*18*).

4.1.3 Effort towards optimization of metal/semiconductor junction in MoS_2 transistor

Despite substantial enhancement of carrier mobility, the understanding of intrinsic electronic transport in thin layered MoS_2 is still in its infancy. One of the major hurdles to electron transport study lies in the large metal/semiconductor junction barrier for carrier injection, leading to a contact resistance dominant charge transport which limits access to intrinsic transport behavior in MoS_2 based devices (*19, 20, 24, 25*), especially in devices with nanoscale dimensions.

For high performance operations, contact between MoS_2 and metals needs to be Ohmic with low resistance as low as 130 Ω μm, required by the International Technology Roadmap for Semiconductors (ITRS), as a high parasitic resistance will limit the overall device performances (*14*). To meet the requirement suggested by ITRS, metal with a proper work function must be used as a contact metal to avoid Schottky barrier formation. Investigations of various contact electrodes having different work functions have been reported for few layered MoS_2 FETs in Figure 4.2 (*20*). Experimental results reveal the evidence of Fermi level pinning close to the conduction band of MoS_2, which impacts strongly electrical characteristics. Metals with low work function such as scandium (Φ_M = 3.5eV) and titanium (Φ_M = 4.3eV) show enhanced performances by allowing more efficient charge carrier injection, in comparison with the results from the high work function metals such as Nickle (Φ_M = 5.0 eV) and Platinum (Φ_M = 5.9eV). Gold is commonly used to yield a reasonably good device performance for the MoS_2 transistor, and was known as a right choice of metal to form Ohmic contact (*18*). As perceived "Ohmic contact formation" judging from seemingly linear I-V characteristics, Schottky barrier still exist at Au/MoS_2

interface, and a misunderstanding of this interpretation is mainly due to the thermally assisted tunneling current component from a very short tunneling distance in ultra-thin 2D layered materials (*18, 20*). Although the performance of the device was enhanced using low work function metals owing to efficient carrier injection, a good Ohmic contact has not been achieved yet.

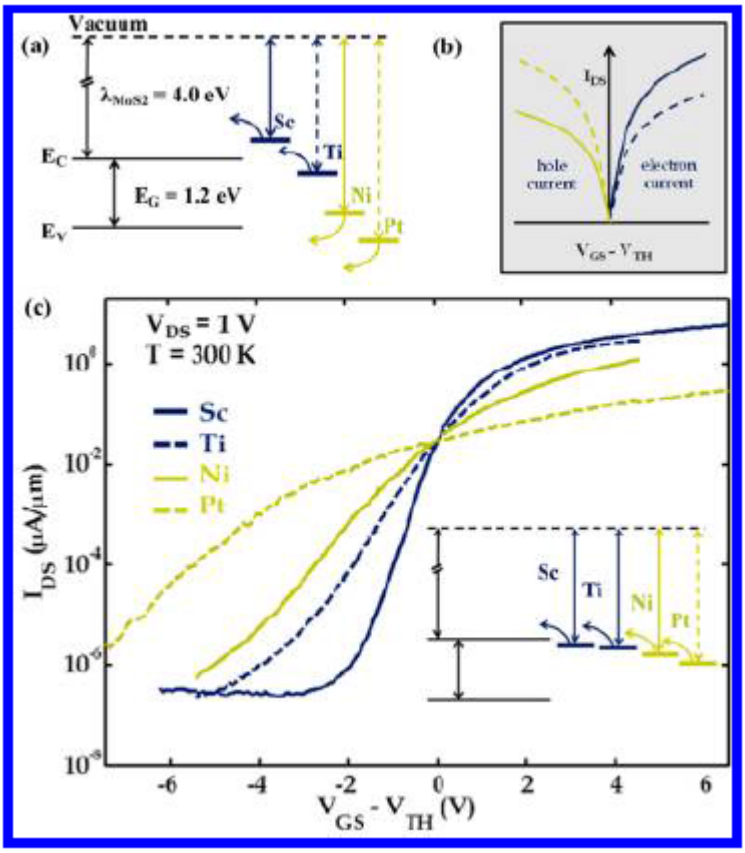

Figure 4.2 (a) expected line-up of metal Fermi level with conduction band of MoS_2. (b) The cartoon of expected transfer characteristics. (c) Transfer characteristics of 6nm-thick MoS_2 transistor s with Sc, Ti, Ni, and Pt metal contacts. Adopted from (*20*).

4.2 Monolayer MoS_2 single electron transistor

4.2.1 Importance of junction barrier for an access to the intrinsic electronic properties of MoS_2

With the right choice of contact metal the junction transparency can be controlled at low temperatures, leading to observation of various fundamental quantum transport behavior like Coulomb blockade at opaque junctions, and Fabry-Perot interference at highly transparent junctions (*26-28*). Here, we report the fabrication of a monolayer MoS_2 single electron transistor using low work function zinc metal contact electrodes, formed with a thermal annealing induced metal migration step. We observe Coulomb blockade phenomena at low temperatures, and ascribe this transport behavior to the single electron tunneling through an isolated clean quantum dot. Our observation serves as a stepping stone for advancing our understanding of intrinsic electronic properties of MoS_2, and providing the new directions from a quantum electronics perspective.

4.2.2 Fabrication of monolayer MoS_2 transistor

The devices discussed in this work were fabricated on monolayer MoS_2 flakes obtained from mechanical exfoliation (*18*) of bulk MoS_2. These flakes were deposited on a highly n-doped silicon substrate covered with 280nm thermally grown silicon dioxide, which serves as a back-gate. Standard electron beam lithography was employed to pattern the source/drain contact of field-effect-transistor devices on the selected flakes. The contact metal consisting of 5nm Zn, and 25nm Au was deposited by e-beam evaporation. Zinc was chosen as an adhesion layer for gold contact on the flakes because the work function of

Zinc is ~ 4.28 ± 0.02 eV(*29*), which is close to the electron affinity of bulk MoS_2 ~ 4eV (*20*), thereby leading to a small Schottky barrier at the metal/semiconductor junction(*20*). A device schematic is shown in Figure 1a. Our monolayer MoS_2 FETs have channel width, W = 1um with source-drain separation ranging from 100nm to 300nm as shown in scanning microscopy image in Figure 1c. Monolayer MoS_2 flakes were identified by color contrast from optical image as shown in Figure 4.3b, and confirmed by AFM measurement (Figure 4.3d).

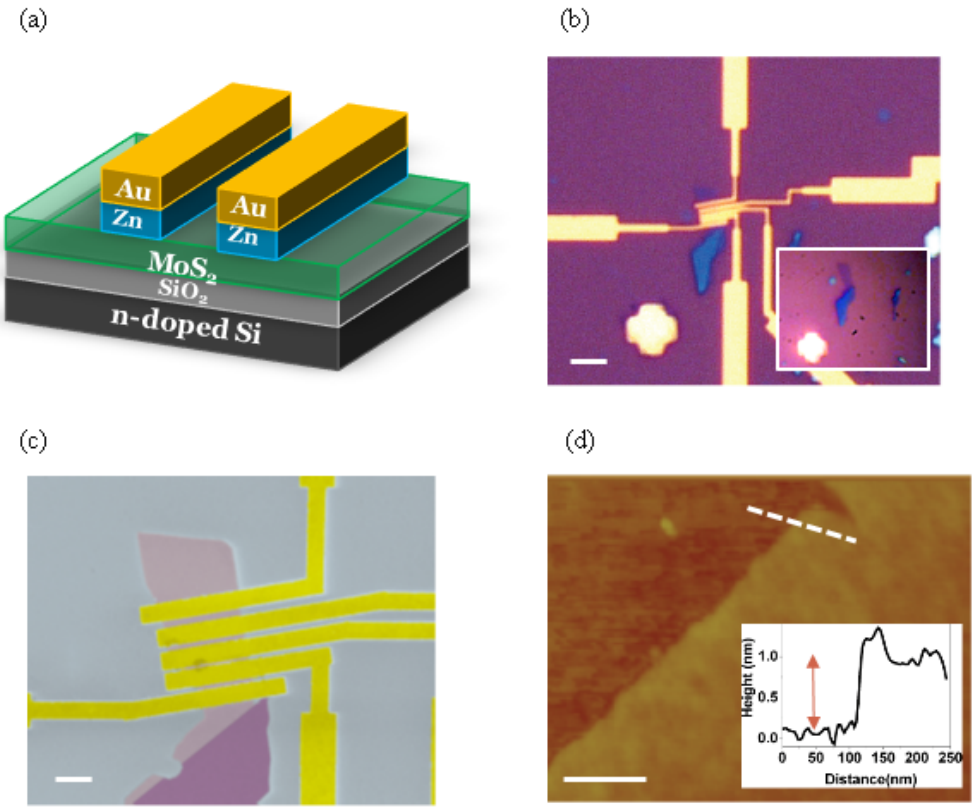

Figure 4.3 (a) Schematic representation of back-gated MoS_2 field effect transistor. (b) Optical microscopy image of MoS_2 device. Inset: Optical micrograph of exfoliated MoS_2 flakes. Scale bar is 5μm. (c) SEM image of monolayer MoS_2 FET. Scale bar is 1μm. (d) AFM image of monolayer MoS_2. (Inset) Height profile obtained by taking cross section along the white line on the image was found to be 1nm. Scale bar is 200nm.

4.2.3 Electrical characterization of MoS_2 transistor

We first studied electronic transport on as fabricated pristine devices in ambient condition at room temperature via two terminal configuration. The drain current versus source bias characteristics shows Schottky barrier dominant electron transport behavior in Figure 4.4a by comparing with earlier reported output characteristics of monolayer MoS_2 transistors (*18*). Even though the curve looks linear, it is mainly attributed to thermally assisted-tunneling current through the atomically thin MoS_2 layer, and not to the ohmic contact formation (*20*). To improve the device performance we performed rapid thermal annealing of fabricated MoS_2 transistors in a Rapid Thermal Processing (RTP) furnace under forming gas at high temperature (~250°C) for 5 minutes. Thermal annealing process has been commonly used to restore clean surface of channel materials by eliminating oxygen and water adsorbents, leading to substantial enhancement in mobility (*22*). Figure 4.4a, b show output characteristics and transfer characteristics of a typical monolayer MoS_2 field-effect-transistor, respectively, before and after thermal annealing. The conductivity increases four fold with shifting the threshold voltage by at least -15V after annealing process. In spite of substantial enhancement of a two-terminal conductivity, the slope of I_{ds}-V_{ds} gets more steeper as higher absolute V_{ds} applied, providing the evidence that monolayer MoS_2 channel is weekly coupled to metallic leads by tunnel barriers (*27*). This opaque contact junction provides us a suitable platform to study Coulomb blockade phenomena at low temperatures, which has not been possible till date due to lack of control on the metal/MoS_2 barrier.

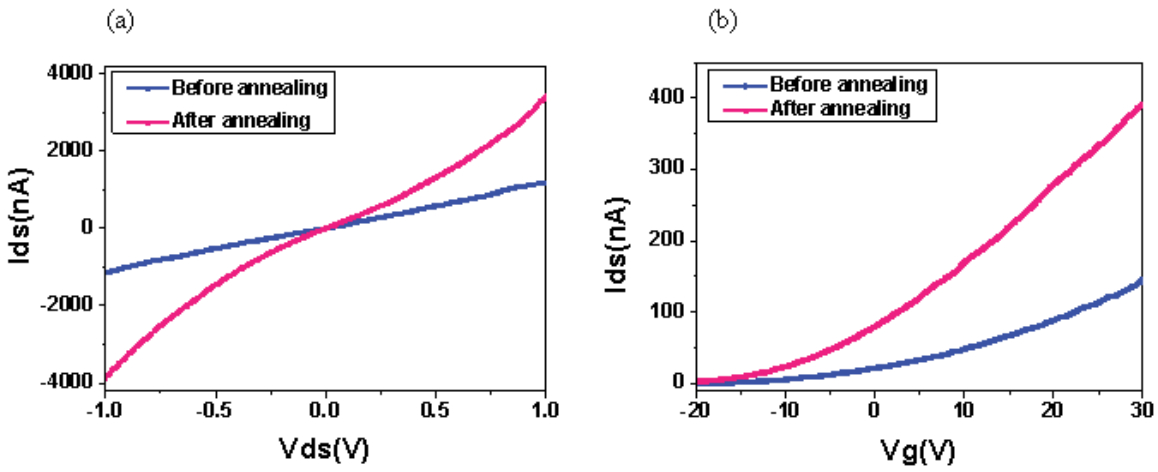

Figure 4.4 (a) Output characteristics and (b) transfer characteristics of two-terminal measurement of MoS_2 device at Vds =10mV before and after thermal annealing for 5mins at 250°C.

4.2.4 Observation of Coulomb blockade in MoS_2 transistor

Next, we investigated the intrinsic properties of our MoS_2 device by two terminal measurement at low-temperatures down to 6K. The anneal step was conducted on this device prior to the electrical characterization. In Figure 4.5a, we plotted the conductance versus back-gate voltage (V_{bg}) for a device with 200nm channel length with 1um width. Surprisingly, we observed periodic conductance oscillations as a function of gate voltage (V_{bg}). The conductance peaks are separated by suppressed conductance regions by an average peak-to-peak distance of 15V. This periodic oscillation is associated with single electron charging phenomena, revealing the nature of Coulomb blockade when $k_BT << E_C$, where k_B is Boltzmann constant, T is the temperature, E_C is the dot charging energy. The differential conductance measurements were performed by applying a small ac bias voltage,

$V_{ds,ac}$ = 100μV, superimposed upon dc bias voltage V_{ds}, with a standard lock-in amplifier method. In figure 4.5b, we plot differential conductance versus bias voltage (V_{ds}). This measurement of Coulomb oscillation along the bias voltage exhibits a Coulomb staircase behavior for different gate voltages. A corresponding two-dimensional differential conductance map of Coulomb blockade oscillation is plotted as a function of bias voltage (V_{ds}) and back-gate voltage (V_{bg}) in Figure 4.5c. From Figure 4.5c, the charging energy of the device is extracted from the extent of Coulomb diamond in a bias direction (V_{ds}), and is almost constant with a charging energy, $E_C \approx 22$meV. This charging energy corresponds to a total capacitance of MoS_2 single-electron transistor (SET), $C_\Sigma = e^2/E_C \approx 7.27$aF. By considering the oscillation period, we estimate a back-gate capacitance, $C_{bg} = e/\Delta V_{ds,period} \approx 0.0107$aF. Thus, the lever arm of back-gate, associated with the capacitance coupling to the back-gate, gives us $\alpha = C_{bg}/C_\Sigma \approx 0.00147$. This value allows the conversion of back-gate voltage into a charging energy scale, which is important for a quantitative understanding of transport spectroscopy of our MoS_2 device. The calculated small lever arm value of back-gate can be attributed to the charge screening effect from source/drain electrodes where the channel length is much smaller than the thickness of gate dielectric ~280nm.

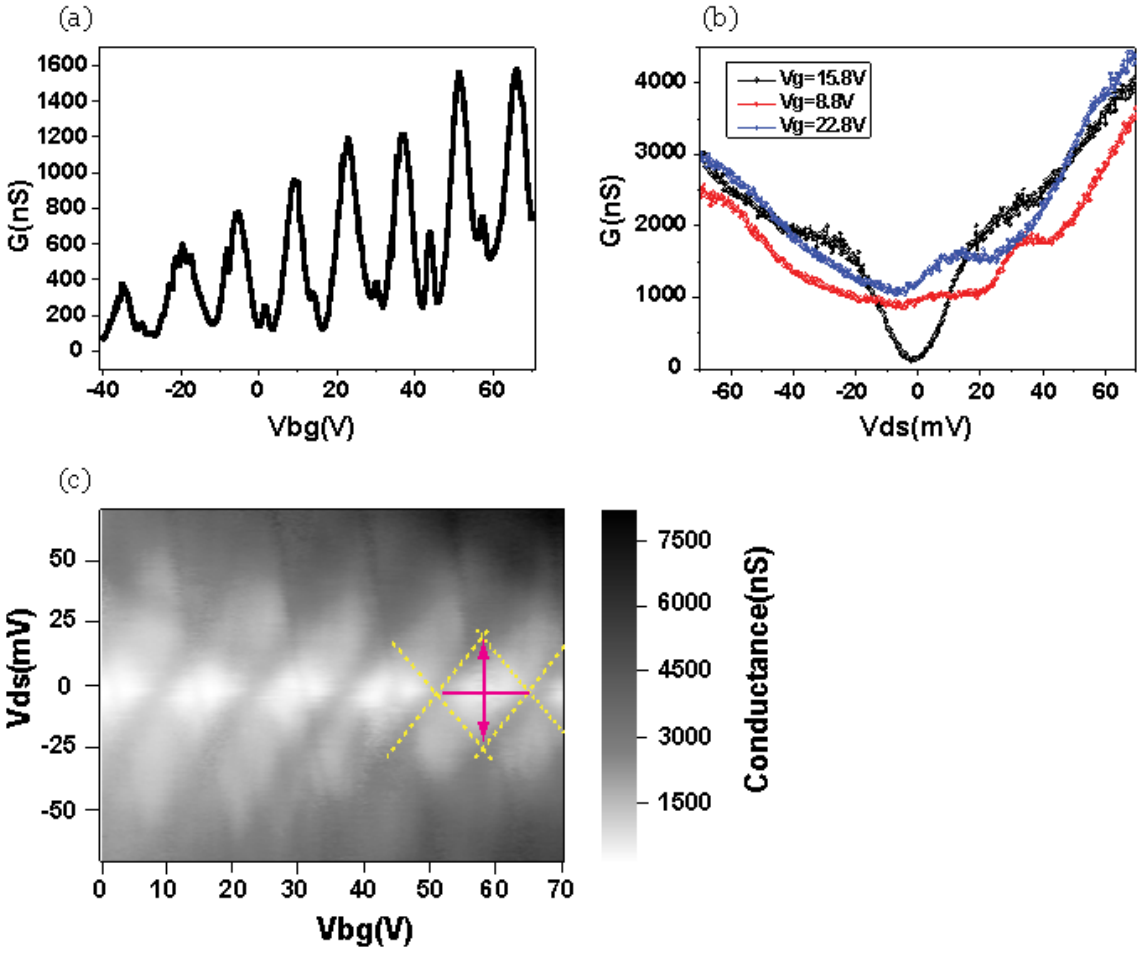

Figure 4.5 Electron transport measurement of monolayer MoS_2 SET at T=6K. (a) Conductance G versus back-gate voltage Vbg and (b) versus bias voltage Vds at Vbg = 8.8V, 15.8V, 22.8V respectively. (c) Corresponding Coulomb diamond in two-dimensional differential conductance as a function of back-gate voltage and bias voltage. The dotted yellow lines in (c) guides to the eyes to the Coulomb diamond. The solid pink arrow and line guide eyes to the bias voltage (Vds), and oscillation period (Vbg). Extracted charging energy is 22meV.

4.2.5 Possible reasons for the observation of Coulomb blockade

4.2.5.1 Charge screening effect

The observation of single charging effect on monolayer MoS_2 channel could possibly be due to the strong charge screening effect as this effect will lead into the formation of fairly small effective dot area. To gain further insight into the origin of Coulomb blockade behavior in MoS_2 SET, we prepared a thinner gate dielectric device using 70nm high-k material, Al_2O_3 as a back-gate dielectric as shown in Figure 4.6a. The thickness of exfoliated MoS_2 flake was confirmed as a monolayer by AFM. We first characterize our device with a channel length of 100nm, and width of 1um at room temperature by electrical transport measurement before and after annealing process. The improvement of the device performance was observed as the I_{ds}-V_{ds} curve becoming more linear and symmetric after annealing. The increased two-terminal conductance is again attributed to the reduction in contact resistance, similar to what is observed in thicker dielectric devices with 280nm SiO_2.

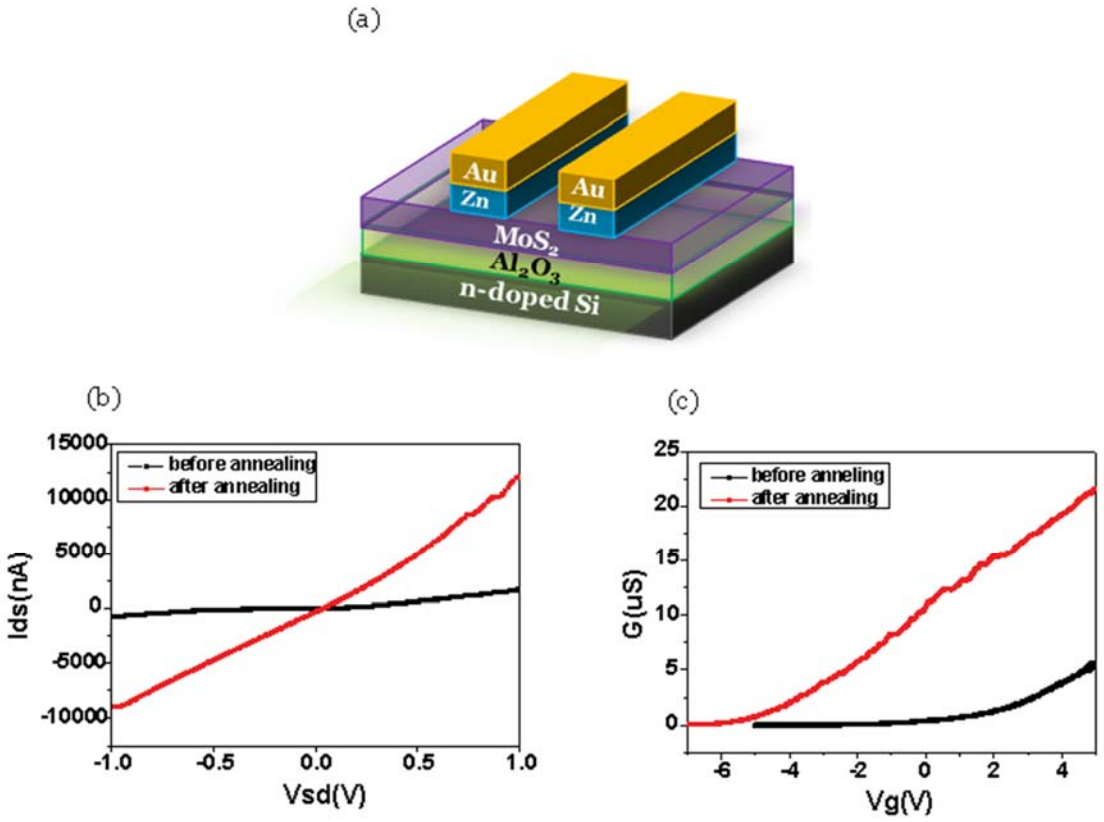

Figure 4.6 (a) Schematic representation of back-gated MoS_2 SET having 70nm Al_2O_3 as a gate dielectric. (b) Output characteristics and (c) transfer characteristics of two-terminal measurement of MoS_2 device before and after thermal annealing for 5mins at 250°C.

We now focus on the transport characteristics of MoS_2 FET device with Al_2O_3 as a gate dielectric at low temperature to identify the origin of Coulomb blockade. Markedly, the current (I_{ds}) versus gate voltage (V_{bg}) measured at small V_{ds} = 100μV shows clear Coulomb oscillations for a device with channel length of 100nm and width of 1μm in linear-response regime (in Figure 4.7a). Oscillation peaks in V_{bg} are reasonably periodic and evenly spaced with a period of $\Delta V_{bg} \approx 0.6V$. The differential conductance dI/dV of a MoS_2 FET device in Figure 4.7b is similar to the Coulomb blockade transport feature of thicker dielectric MoS_2 SET device with 280nm SiO_2. From the Coulomb diamond

measurement, regular closed diamond patterns provide an evidence that only a single quantum dot exists in our device (*30*). A charging energy is estimated to be $E_C \approx 17.6$meV from this measurement. This value corresponds to a total capacitance, $C_\Sigma \approx 9.37$aF. Analysis of these results give us lever arm of back-gate, $\alpha \approx 0.0285$, with back-gate capacitance, $C_{bg} \approx 0.267$aF, extracted from oscillation period. Thus, by adopting high-k Al_2O_3 as a gate dielectric material, we observe significant improvement in electrostatic coupling to the back-gate in MoS_2 device by ~ 20 times, as expected. We note that Coulomb blockade phenomena from thinner gate dielectric device strongly supports the idea that metal diffusion, rather than screening effect, could be responsible for this single electron charging behaviour due to scaling down of the channel area during the annealing process.

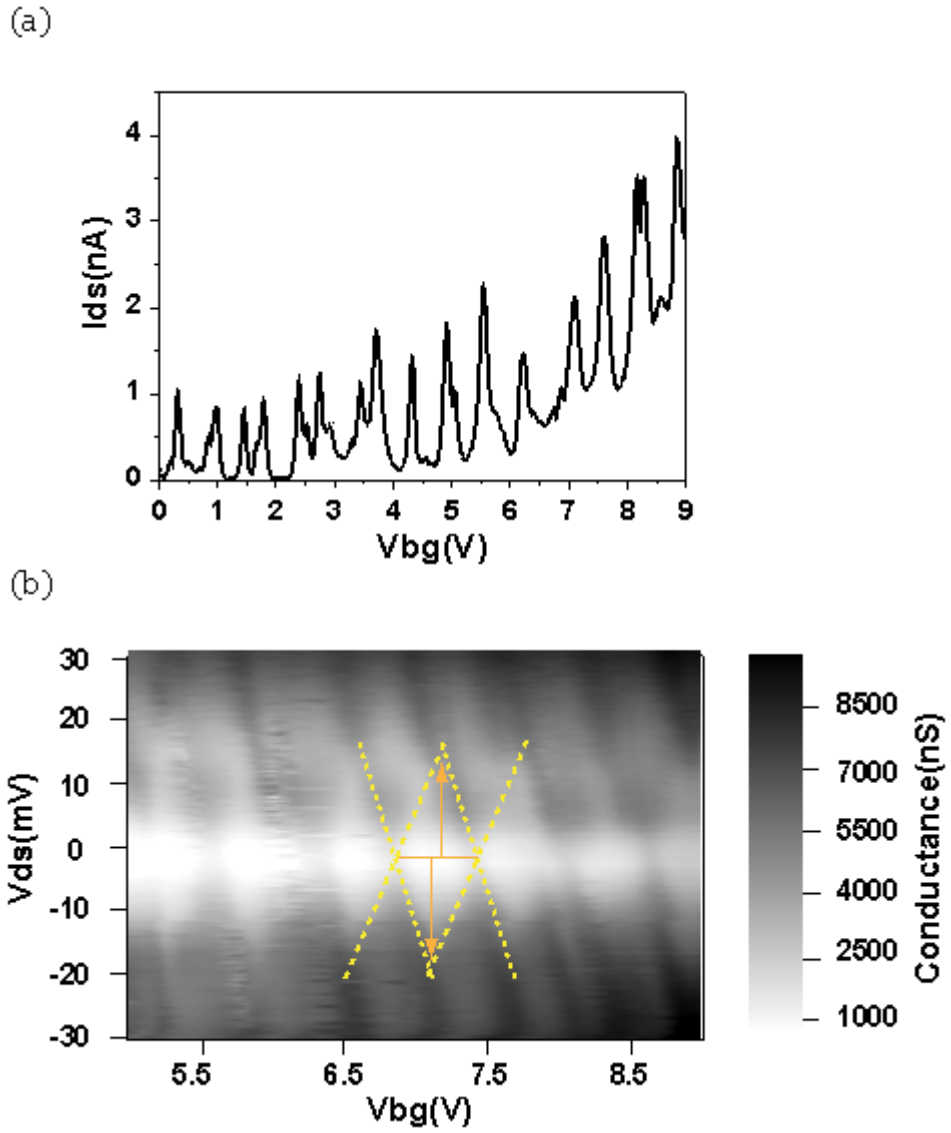

Figure 4.7 (a) Coulomb blockade peak current as a function of back-gate voltage with bias voltage = 100μV at 6K. (b) Conductance map of Coulomb blockade oscillations as a function of bias voltage (Vds) and back-gate voltage (Vbg). Yellow dotted lines for guiding to the eyes of Coulomb diamond, with orange arrow indicating charging energy scale. The dot charging energy is $E_C \approx 17.6$meV.

4.2.5.2 Metal diffusion during annealing process

Thus, we also performed control experiments with as prepared MoS_2 devices having 280nm SiO_2 gate dielectric layer without the annealing step, however, Coulomb blockade behavior was not observed. Even MoS_2 transistors with channel lengths ~50nm did not show any coulomb blockade. Furthermore, we observed that source and drain shorted in MoS_2 devices with ~ 50nm channel separation at room temperature after the thermal annealing process indicating that metal diffusion plays a crucial role in inducing single electron tunneling features.

4.2.5.3 MoS_2 thickness dependent barrier height

We note that Coulomb blockade was observed only in single and bilayer MoS_2 FETs, and few-layered MoS_2 FETs with similar physical dimension did not show coulomb blockade at low temperatures (in Figure 4.8, and Figure 4.9). Also, few layer (>3 layers) MoS_2 FETs generally showed much higher conductance at room temperature compared to monolayer MoS_2 FETs. With increasing number of layers, the barrier height decreases, and this has been previously reported and is consistent with our result (*21*). This finding also supports the interpretation that leads made on few-layer MoS_2 form tunnel barriers which do not meet essential requirement of low conductance at the source and drain electrodes, G_{source}, $G_{drain} < e^2/h$, for the observation of Coulomb blockade at moderately low temperature, $k_BT < E_C$. In other words, only monolayer and bilayer MoS_2/Zn junction can fulfill this requirement for weakly coupled system between semiconductor dot to reservoirs via suitable barrier heights

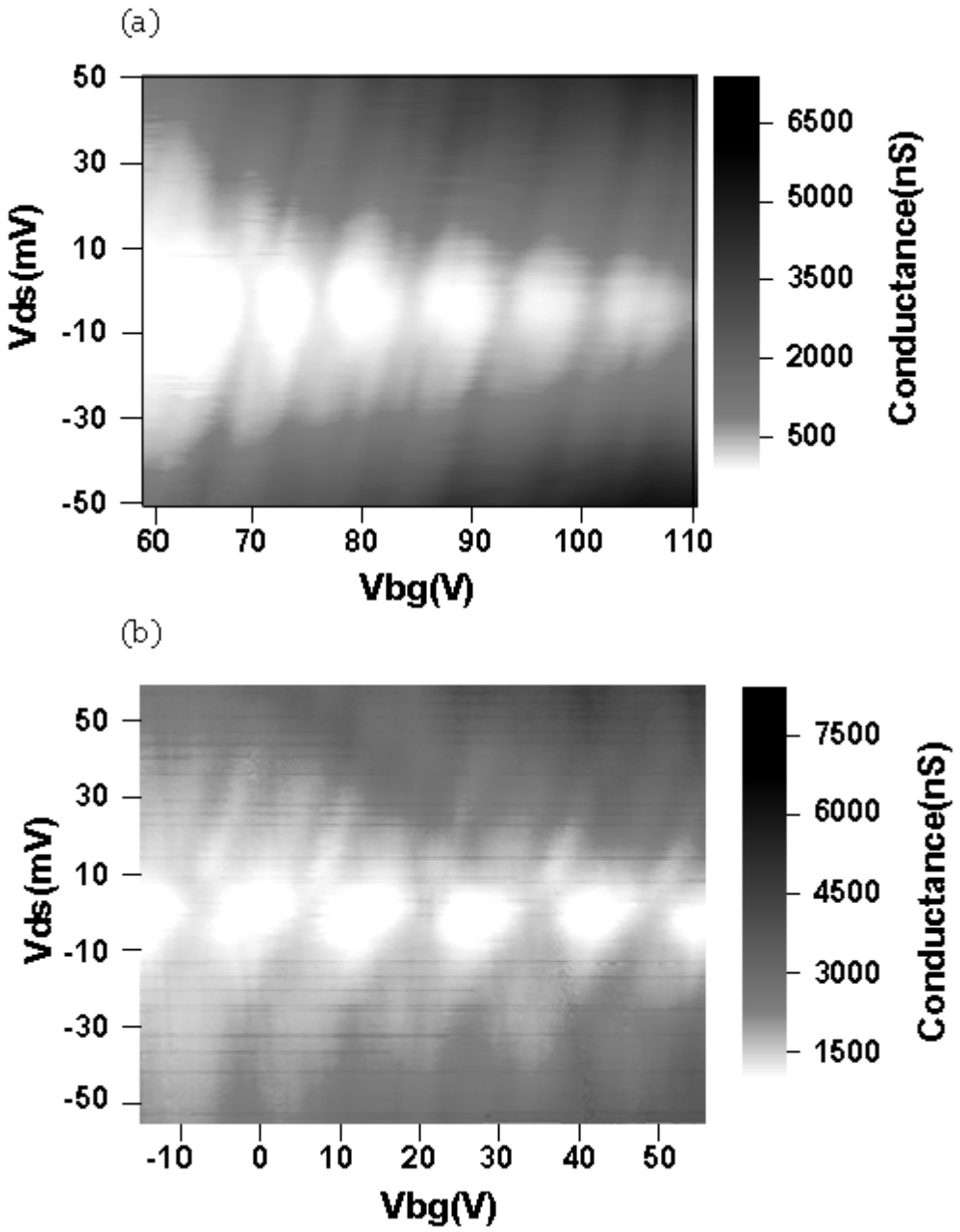

Figure 4.8 Conductance map of Coulomb blockade oscillations as a function of bias voltage (V_{ds}) and back-gate voltage (V_{bg}) in (a) monolayer MoS_2 FET with 200nm length and 1.5μm width dimension, and in (b) monolayer MoS_2 FET with 300nm length and 1.2μm width dimension.

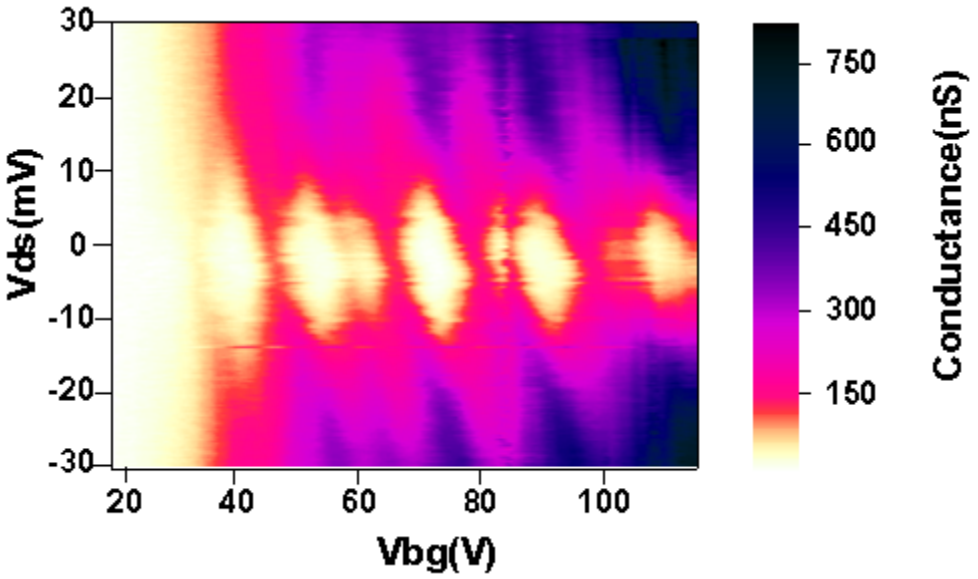

Figure 4.9 Coulomb blockade oscillations as a function of bias voltage (Vds) and back-gate voltage (Vbg) in bilayer MoS_2 FET with 250nm length and 700nm width dimension.

4.2.6 Classical Coulomb blockade regime

Temperature dependence of coulomb blockade can reveal fundamental information about nature of Coulomb blockade. Hence, we also investigated the temperature dependence of Coulomb oscillations as a function of gate voltage, as shown in Figure 4. 10a. The oscillating feature of our device remains discernible even at T = 30K. In addition, analysis of conductance peak linewidths (W) at temperatures ranging from 6K to 30K yield electrostatic gate coupling constant, α, depending upon the nature of Coulomb blockade, whether it is in the classical regime, or in the quantum regime. In classical regime, for $\Delta E < k_BT < E_C$ where ΔE is the single particle level spacing, and E_C is the Coulomb charging energy, the relation is described as $\alpha W = 3.52k_BT/e$ *(30)*. For quantum regime, $k_BT < \Delta E$, the relation is given by $\alpha W = 4.35k_BT/e$ *(30)*. Using the relation of classical regime, the

value α determined from temperature dependent peak linewidths is 0.0293, which is reasonably consistent with the value estimated directly from Coulomb diamond data in Figure 4.10c. These experimental results further support our interpretation that electron transport occurs by tunneling through an isolated single quantum dot in classical regime, which can be described by so called orthodox Coulomb blockade theory (*31*).

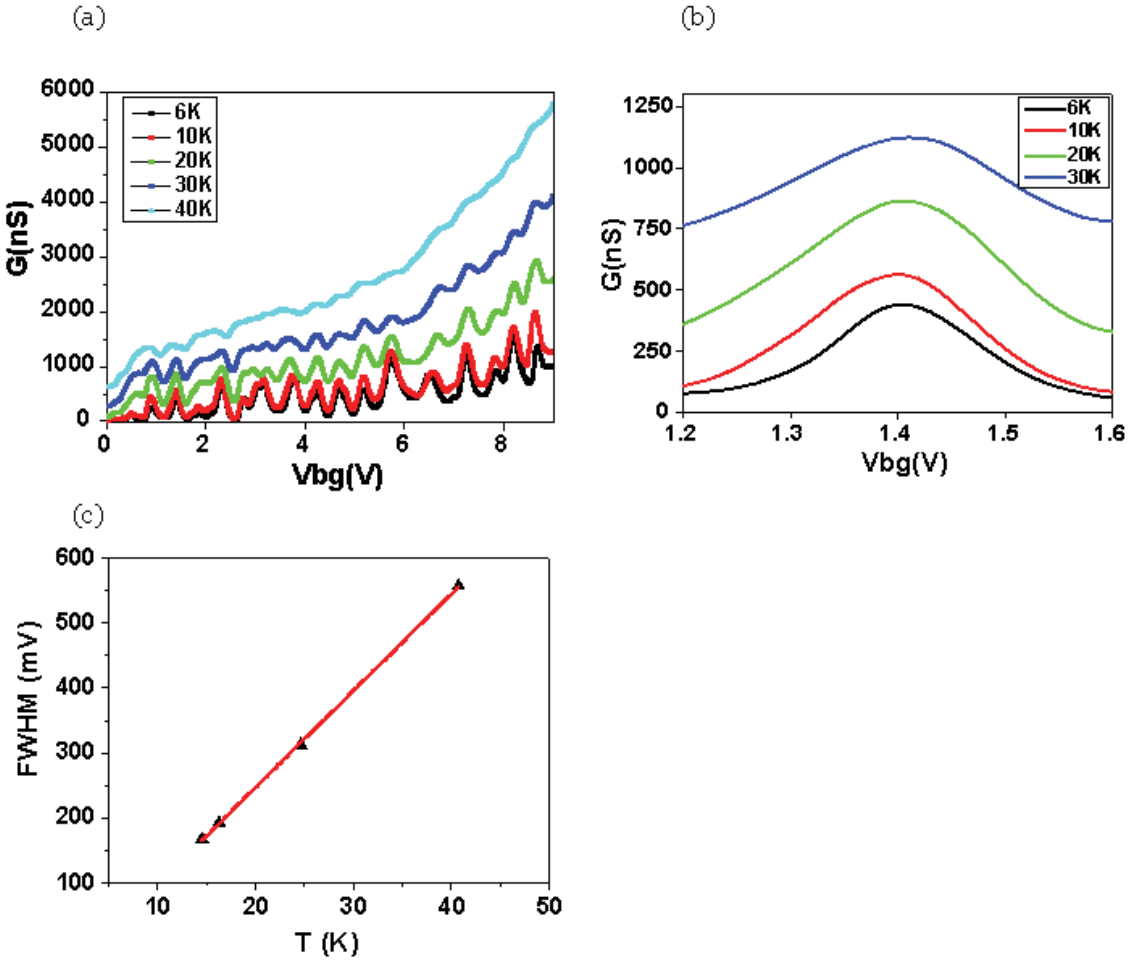

Figure 4.10 Temperature dependent conductance oscillations. (a) Conductance (G) versus back-gate voltage (Vbg) measured at different temperatures, at T = 6K (black line), at T = 10K (red line), at T= 20K (green line), at T = 30K (dark blue line), at T= 40K (blue line). (b) Temperature dependence of oscillation peak. (c) Full-width-half-maximum (FWHM) values of the peak as a function of temperature (T). The lever arm of back-gate, α, is determined to be 0.0293 from the slope of the plot by the formula, $\alpha W = 3.52 k_B T/e$, describing classical Coulomb blockade behavior.

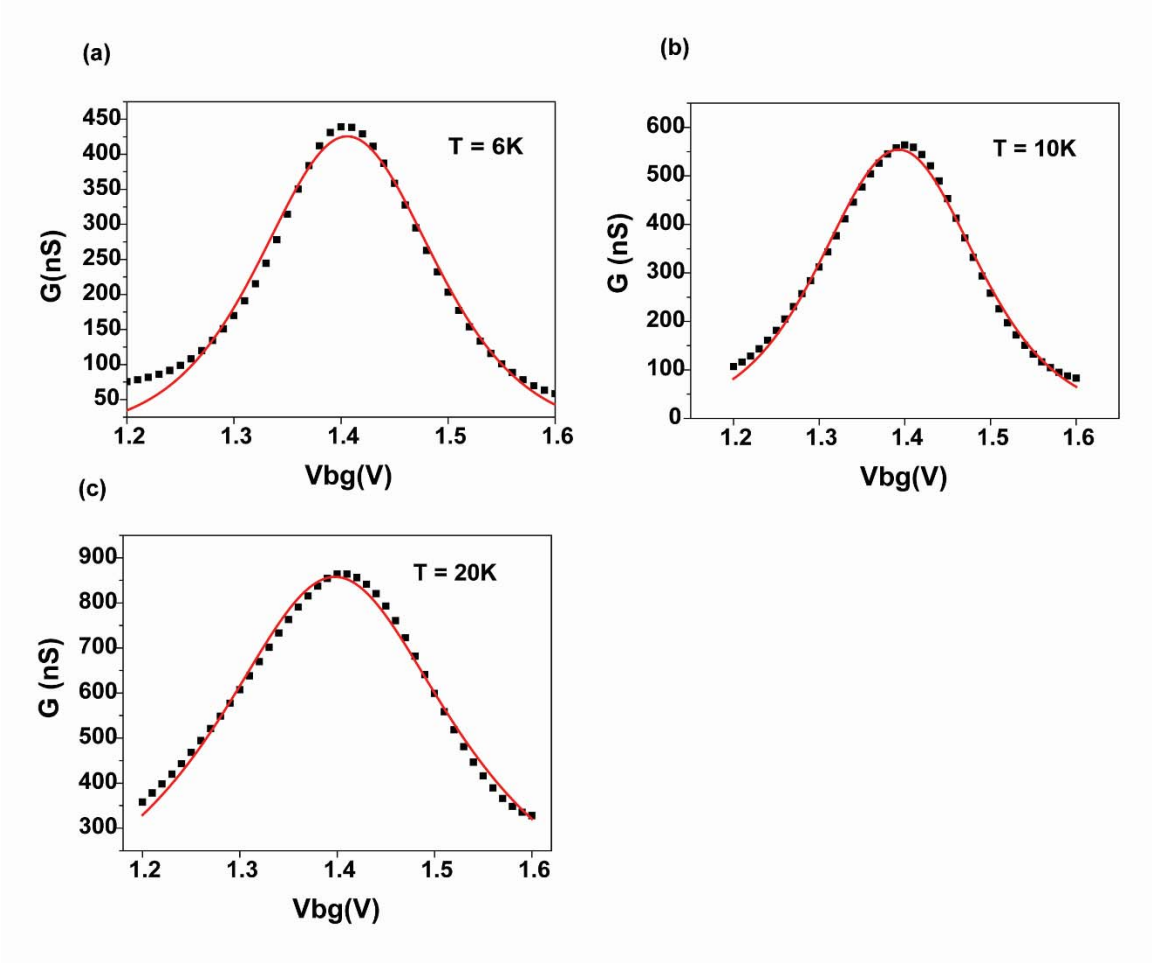

Figure 4.11 Electron temperatures are extracted by fitting measured Coulomb oscillations to the classical Coulomb blockade conductance expression (Appendix B) at different temperatures measurement: (a) $T_e \approx 11.65K$ (b) $T_e \approx 14.44K$ (c) $T_e \approx 23.89K$.

4.2.7 Conclusion

In conclusion, we have demonstrated high quality MoS_2 SET device that may pave the way for opportunities of observing novel quantum transport behaviours in atomically thin-layered TMDCs. We showed Coulomb blockade features from monolayer MoS_2 FETs at low temperature measurement by selecting low work function metal, Zinc, as source/drain metal contact, and by utilizing metal diffusion process essential for quantum

dot formation. In addition, our findings indicate that a suitable barrier height can be carefully designed by controlling barrier height with thickness of MoS_2 for realizing SET. Recently, quantum dot (QD) formed from TMDCs has been proposed as a suitable platform for realizing quantum bits (qubits) systems due to strong intrinsic spin-orbit splitting states from theoretical predictions(*8*). Along these lines, our initial result of quantum transport in atomically thin layered TMDCs could serve as a technological framework as demonstrated here for investigating novel quantum effects such as manipulation of qubit systems.

References

1. A. Splendiani, L. Sun, Y. Zhang, T. Li, J. Kim, C.-Y. Chim, G. Galli, F. Wang, Emerging Photoluminescence in Monolayer MoS2. *Nano Letters* **10**, 1271-1275 (2010); published online Epub2010/04/14 (10.1021/nl903868w).
2. A. Kuc, N. Zibouche, T. Heine, Influence of quantum confinement on the electronic structure of the transition metal sulfide TSS${}_{2}$. *Physical Review B* **83**, 245213 (2011).
3. H. Zeng, J. Dai, W. Yao, D. Xiao, X. Cui, Valley polarization in MoS2 monolayers by optical pumping. *Nat Nano* **7**, 490-493 (2012)http://www.nature.com/nnano/journal/v7/n8/abs/nnano.2012.95.html#supplementary-information).
4. T. Cao, G. Wang, W. Han, H. Ye, C. Zhu, J. Shi, Q. Niu, P. Tan, E. Wang, B. Liu, J. Feng, Valley-selective circular dichroism of monolayer molybdenum disulphide. *Nat Commun* **3**, 887 (2012).
5. K. F. Mak, K. He, J. Shan, T. F. Heinz, Control of valley polarization in monolayer MoS2 by optical helicity. *Nat Nano* **7**, 494-498 (2012); published online Epub08//print (http://www.nature.com/nnano/journal/v7/n8/abs/nnano.2012.96.html#supplementary-information).
6. K. F. Mak, K. L. McGill, J. Park, P. L. McEuen, The valley Hall effect in MoS2 transistors. *Science* **344**, 1489-1492 (2014); published online EpubJune 27, 2014 (10.1126/science.1250140).
7. SuzukiR, SakanoM, Y. J. Zhang, AkashiR, MorikawaD, HarasawaA, YajiK, KurodaK, MiyamotoK, OkudaT, IshizakaK, AritaR, IwasaY, Valley-dependent spin polarization in bulk MoS2 with broken inversion symmetry. *Nat Nano* **9**, 611-617 (2014)10.1038/nnano.2014.148

http://www.nature.com/nnano/journal/v9/n8/abs/nnano.2014.148.html#supplementary-information).

8. A. Kormányos, V. Zólyomi, N. D. Drummond, G. Burkard, Spin-Orbit Coupling, Quantum Dots, and Qubits in Monolayer Transition Metal Dichalcogenides. *Physical Review X* **4**, 011034 (2014).
9. D. Xiao, G.-B. Liu, W. Feng, X. Xu, W. Yao, Coupled Spin and Valley Physics in Monolayers of ${\mathrm{MoS}}_{2}$ and Other Group-VI Dichalcogenides. *Physical Review Letters* **108**, 196802 (2012); published online Epub05/07/ (
10. X. Qian, J. Liu, L. Fu, J. Li, Quantum spin Hall effect in two-dimensional transition metal dichalcogenides. *Science* **346**, 1344-1347 (2014); published online EpubDecember 12, 2014 (10.1126/science.1256815).
11. D. C. Elias, R. V. Gorbachev, A. S. Mayorov, S. V. Morozov, A. A. Zhukov, P. Blake, L. A. Ponomarenko, I. V. Grigorieva, K. S. Novoselov, F. Guinea, A. K. Geim, Dirac cones reshaped by interaction effects in suspended graphene. *Nat Phys* **7**, 701-704 (2011)http://www.nature.com/nphys/journal/v7/n9/abs/nphys2049.html#supplementary-information).
12. A. S. Mayorov, R. V. Gorbachev, S. V. Morozov, L. Britnell, R. Jalil, L. A. Ponomarenko, P. Blake, K. S. Novoselov, K. Watanabe, T. Taniguchi, A. K. Geim, Micrometer-Scale Ballistic Transport in Encapsulated Graphene at Room Temperature. *Nano Letters* **11**, 2396-2399 (2011); published online Epub2011/06/08 (10.1021/nl200758b).
13. S. Lee, K. Lee, Z. Zhong, Wafer Scale Homogeneous Bilayer Graphene Films by Chemical Vapor Deposition. *Nano Letters* **10**, 4702-4707 (2010); published online Epub2010/11/10 (10.1021/nl1029978).
14. G. Fiori, F. Bonaccorso, G. Iannaccone, T. Palacios, D. Neumaier, A. Seabaugh, S. K. Banerjee, L. Colombo, Electronics based on two-dimensional materials. *Nat Nano* **9**, 768-779 (2014); published online Epub10//print (10.1038/nnano.2014.207).
15. Q. H. Wang, K. Kalantar-Zadeh, A. Kis, J. N. Coleman, M. S. Strano, Electronics and optoelectronics of two-dimensional transition metal dichalcogenides. *Nat Nano* **7**, 699-712 (2012); published online Epub11//print (
16. F. Schwierz, Graphene transistors. *Nat Nano* **5**, 487-496 (2010).
17. A. K. Geim, I. V. Grigorieva, Van der Waals heterostructures. *Nature* **499**, 419-425 (2013)10.1038/nature12385).
18. RadisavljevicB, RadenovicA, BrivioJ, GiacomettiV, KisA, Single-layer MoS2 transistors. *Nat Nano* **6**, 147-150 (2011)http://www.nature.com/nnano/journal/v6/n3/abs/nnano.2010.279.html#supplementary-information).
19. H. Liu, A. T. Neal, P. D. Ye, Channel Length Scaling of MoS2 MOSFETs. *ACS Nano* **6**, 8563-8569 (2012); published online Epub2012/10/23 (10.1021/nn303513c).
20. S. Das, H.-Y. Chen, A. V. Penumatcha, J. Appenzeller, High Performance Multilayer MoS2 Transistors with Scandium Contacts. *Nano Letters* **13**, 100-105 (2013); published online Epub2013/01/09 (10.1021/nl303583v).

21. S.-L. Li, K. Komatsu, S. Nakaharai, Y.-F. Lin, M. Yamamoto, X. Duan, K. Tsukagoshi, Thickness Scaling Effect on Interfacial Barrier and Electrical Contact to Two-Dimensional MoS2 Layers. *ACS Nano* **8**, 12836-12842 (2014); published online Epub2014/12/23 (10.1021/nn506138y).
22. B. W. H. Baugher, H. O. H. Churchill, Y. Yang, P. Jarillo-Herrero, Intrinsic Electronic Transport Properties of High-Quality Monolayer and Bilayer MoS2. *Nano Letters* **13**, 4212-4216 (2013); published online Epub2013/09/11 (10.1021/nl401916s).
23. X. Cui, G.-H. Lee, Y. D. Kim, G. Arefe, P. Y. Huang, C.-H. Lee, D. A. Chenet, X. Zhang, L. Wang, F. Ye, F. Pizzocchero, B. S. Jessen, K. Watanabe, T. Taniguchi, D. A. Muller, T. Low, P. Kim, J. Hone, Multi-terminal transport measurements of MoS2 using a van der Waals heterostructure device platform. *Nat Nano* **advance online publication**, (2015); published online Epub04/27/online (10.1038/nnano.2015.70
http://www.nature.com/nnano/journal/vaop/ncurrent/abs/nnano.2015.70.html#supplementary-information).
24. R. Kappera, D. Voiry, S. E. Yalcin, B. Branch, G. Gupta, A. D. Mohite, M. Chhowalla, Phase-engineered low-resistance contacts for ultrathin MoS2 transistors. *Nat Mater* **13**, 1128-1134 (2014); published online Epub12//print (10.1038/nmat4080
http://www.nature.com/nmat/journal/v13/n12/abs/nmat4080.html#supplementary-information).
25. L. Yu, Y.-H. Lee, X. Ling, E. J. G. Santos, Y. C. Shin, Y. Lin, M. Dubey, E. Kaxiras, J. Kong, H. Wang, T. Palacios, Graphene/MoS2 Hybrid Technology for Large-Scale Two-Dimensional Electronics. *Nano Letters* **14**, 3055-3063 (2014); published online Epub2014/06/11 (10.1021/nl404795z).
26. W. Liang, M. Bockrath, H. Park, TRANSPORT SPECTROSCOPY OF CHEMICAL NANOSTRUCTURES: The Case of Metallic Single-Walled Carbon Nanotubes. *Annual Review of Physical Chemistry* **56**, 475-490 (2005)doi:10.1146/annurev.physchem.56.092503.141226).
27. L. Marty, V. Bouchiat, C. Naud, M. Chaumont, T. Fournier, A. M. Bonnot, Schottky Barriers and Coulomb Blockade in Self-Assembled Carbon Nanotube FETs. *Nano Letters* **3**, 1115-1118 (2003); published online Epub2003/08/01 (10.1021/nl0342848).
28. W. Liang, M. Bockrath, D. Bozovic, J. H. Hafner, M. Tinkham, H. Park, Fabry - Perot interference in a nanotube electron waveguide. *Nature* **411**, 665-669 (2001); published online Epub06/07/print (
29. P. A. Anderson, The Contact Difference of Potential Between Barium and Zinc The External Work Function of Zinc. *Physical Review* **57**, 122-127 (1940); published online Epub01/15/ (
30. Z. Zhong, Y. Fang, W. Lu, C. M. Lieber, Coherent Single Charge Transport in Molecular-Scale Silicon Nanowires. *Nano Letters* **5**, 1143-1146 (2005); published online Epub2005/06/01 (10.1021/nl050783s).
31. D. V. Averin, K. K. Likharev, Coulomb blockade of single-electron tunneling, and coherent oscillations in small tunnel junctions. *J Low Temp Phys* **62**, 345-373 (1986); published online Epub1986/02/01 (10.1007/BF00683469).

Chapter 5

Summary and Conclusion

5.1 Summary of completed work

5.1.1 Wafer scale homogeneous bilayer graphene synthesis

In this thesis work, I demonstrated the first ever CVD growth of homogeneous bilayer graphene films over at least square inch area (*1*). Our grown bilayer graphene was synthesized by chemical vapor deposition on copper foil and subsequently transferred to arbitrary substrates. Bilayer coverage of over 99% is confirmed by spatially resolved Raman spectroscopy. The result is further supported by electrical transport measurements on bilayer graphene transistors with dual-gate configuration, where field induced bandgap opening is observed in 98% of the devices. The size of our bilayer graphene film is only limited by the synthesis apparatus and can be readily scaled up.

The discovery of electric field induced tunable bandgap opening in bilayer graphene (*2-4*) paves the way for making semiconducting graphene without aggressive size scaling (*5*), or using expensive substrates (*6*). Despite intensive research, synthesizing homogeneous bilayer graphene in large size has proven extremely challenging (*7*), and the size of bilayer graphene was limited to micrometer scale by exfoliation. In this respect, our success in wafer scale synthesis would be a significant

step towards realizing bilayer graphene as a promising electronic material in an upcoming post-silicon era.

5.1.2 Chiral transport in bilayer graphene

Arising from combined features of masslessness and chirality, quasiparticles in graphene behave differently from charge carriers in conventional semiconductors, exhibiting novel phenomena such as anomalous quantum Hall effect (*8-10*) and Klein tunneling effect (*11, 12*). These two exotic transport features have been studied extensively, and proven experimentally. In contrast to the monolayer graphene, Bilayer graphene is an exciting system to study chirality related features because chiral quasiparticles of bilayer graphene have a finite effective mass. Hence, after successfully demonstrating wafer scale reproducible growth of graphene, next I studied chiral properties of charge carriers using our CVD bilayer graphene.

In this work, I demonstrated electronic Anti-Klein tunneling with cloaking effect as a manifestation of chirality in transport by probing phase coherent transport behavior in CVD bilayer graphene nanostructure. Our findings shed light on the importance of chirality in carrier motion, and may hold promise for the realization of pseudo-spintronics based on bilayer graphene.

5.1.3 Single electron tunneling in monolayer MoS_2 transistor

Similar to graphene (*13, 14*), other 2D materials also have huge promise (*15, 16*) and are playgrounds for rich condensed matter physics. However, till now researchers have not been able to access the intrinsic properties due to poor junction barrier (*17, 18*). In the final phase of my thesis work, I focused on electron transport study in 2D MoS_2 device at

low-temperature. I demonstrated monolayer MoS_2 single electron transistor, which is achieved by adopting low work function metal Zinc for the contact. Coulomb blockade is observed at low temperatures, and is attributed to the quantum dot formation through a rapid thermal annealing assisted metal diffusion. Our results shed light promise the study of novel quantum transport phenomena in 2D semiconductor materials.

5.2 Conclusion and Future Directions

The prospect for applications in the electronic and computer industry is an important motivation for understanding the transport properties of atomically thin two-dimensional materials (*13, 15, 16, 19-21*). The electron transport study is also interesting from a fundamental point of view, since many phenomena that originate from the quantum nature of matter can be revealed in 2D materials (*9, 13, 22-26*). Examples of such phenomena in graphene are anomalous quantum hall effect (*8-10*), topologically protected current (*27, 28*), and Klein tunneling (*11, 12*), etc.; and in 2D TMDC materials novel quantum effects such as coupling of spin-valley physics (*23, 24*) and quantum spin-Hall-effect (*26*), etc. are expected.

The focus of my thesis work was to understand and exploit the unique and novel electronic properties of atomically thin two-dimensional materials of bilayer graphene and MoS_2. Wafer scale homogeneous bilayer graphene was firstly demonstrated by developing the synthesis method, and utilized for investigating the importance of coupling of pseudospin and carrier motion via chirality in electron transport. Finally, transport study of MoS_2 was conducted to realize theoretically predicted novel quantum effects in experiment. Based on the accumulated knowledge of contact junction transparency dependent quantum

transport, I observed single electron tunneling behavior via Schottky barrier with mono- and bilayer- MoS_2 field effect transistor. Our work opens up new possibilities for novel quantum electronic device made from both bilayer graphene and 2D TMDCs.

Two dimensional materials are a very active area for a various potential applications. One of the interesting applications is to use quantum-spin-hall (QSH) effect device, called topological field effect transistor (TFET) (*26*). Quantum spin hall effect device have insulating bulk states, but conducting edge state protected from back-scattering by time-reversal symmetry. The main advantage of TFET would enable very high density on a chip, and low power consumption, promising for potential applications in post-silicon electronics. The prototype of TFET is proposed based on vdW (van-der-Waals) heterostructures, having a single layer 2D material sandwiched by two layers of 2D-boron nitride (*26*). In this device scheme, the QSH can be switched on and off easily by applying an electric field to the sandwiched single layer 2D material to induce band-gap opening and closing in edge state.

Unlikely most-studied 2H-MX_2 semiconducting TMDCs, 1T-MX_2 metallic state 2D TMDCs materials are needed to realize TFET according to proposed theoretical result. However, the 1T-polytype MX_2 has been known to be unstable in free-standing condition, and in the air. Thus, realization of QSH device from 2D TMDCs materials has several challenges: (i) preparation of 1T-phase monolayer MoS_2, (ii) fabrication of vdW structure using unstable state 1T MoS_2, and (iii) development of measurement scheme. To achieve monolayer MoS_2 QSH device, most effort would be devoted to the implementation of vdW heterostructure using MoS_2 in the first stage of my future work. To obtain 1T-MoS_2, lithium-based intercalation method will be adopted for the formation of 1T metallic MoS_2

from exfoliated monolayer MoS_2 (*29*). Finally, I will conduct transport measurement on our device to confirm and distinguish helical edge state dominant current from bulk state dominant current (*30*). Based on the work presented in this thesis including characterization of 2D materials, nanofabrication skills, and quantum transport knowledge, this new type of QSH electronic devices would be investigated. If we demonstrate QSH device made from atomically thin 2D layers, this would open doors the possibility of 2D TMDCs materials for a new type of quantum electronic device.

REFERENCES

1. S. Lee, K. Lee, Z. Zhong, Wafer Scale Homogeneous Bilayer Graphene Films by Chemical Vapor Deposition. *Nano Letters* **10**, 4702-4707 (2010); published online Epub2010/11/10 (10.1021/nl1029978).
2. E. V. Castro, K. S. Novoselov, S. V. Morozov, N. M. R. Peres, J. M. B. L. dos Santos, J. Nilsson, F. Guinea, A. K. Geim, A. H. C. Neto, Biased Bilayer Graphene: Semiconductor with a Gap Tunable by the Electric Field Effect. *Physical Review Letters* **99**, 216802 (2007).
3. J. B. Oostinga, H. B. Heersche, X. Liu, A. F. Morpurgo, L. M. K. Vandersypen, Gate-induced insulating state in bilayer graphene devices. *Nat Mater* **7**, 151-157 (2008); published online Epub02//print (http://www.nature.com/nmat/journal/v7/n2/suppinfo/nmat2082_S1.html).
4. Y. Zhang, T.-T. Tang, C. Girit, Z. Hao, M. C. Martin, A. Zettl, M. F. Crommie, Y. R. Shen, F. Wang, Direct observation of a widely tunable bandgap in bilayer graphene. *Nature* **459**, 820-823 (2009)http://www.nature.com/nature/journal/v459/n7248/suppinfo/nature08105_S1.html).
5. M. Y. Han, B. Özyilmaz, Y. Zhang, P. Kim, Energy Band-Gap Engineering of Graphene Nanoribbons. *Physical Review Letters* **98**, 206805 (2007).
6. S. Y. Zhou, G. H. Gweon, A. V. Fedorov, P. N. First, W. A. de Heer, D. H. Lee, F. Guinea, A. H. Castro Neto, A. Lanzara, Substrate-induced bandgap opening in epitaxial graphene. *Nat Mater* **6**, 770-775 (2007); published online Epub10//print (http://www.nature.com/nmat/journal/v6/n10/suppinfo/nmat2003_S1.html).
7. X. Li, W. Cai, J. An, S. Kim, J. Nah, D. Yang, R. Piner, A. Velamakanni, I. Jung, E. Tutuc, S. K. Banerjee, L. Colombo, R. S. Ruoff, Large-Area Synthesis of High-Quality and Uniform Graphene Films on Copper Foils. *Science* **324**, 1312-1314 (2009); published online EpubJune 5, 2009 (10.1126/science.1171245).

8. Y. Zhang, Y.-W. Tan, H. L. Stormer, P. Kim, Experimental observation of the quantum Hall effect and Berry's phase in graphene. *Nature* **438**, 201-204 (2005); published online Epub11/10/print (http://www.nature.com/nature/journal/v438/n7065/suppinfo/nature04235_S1.html).
9. K. S. Novoselov, Z. Jiang, Y. Zhang, S. V. Morozov, H. L. Stormer, U. Zeitler, J. C. Maan, G. S. Boebinger, P. Kim, A. K. Geim, Room-Temperature Quantum Hall Effect in Graphene. *Science* **315**, 1379 (2007); published online EpubMarch 9, 2007 (10.1126/science.1137201).
10. K. S. Novoselov, E. McCann, S. V. Morozov, V. I. Fal'ko, M. I. Katsnelson, U. Zeitler, D. Jiang, F. Schedin, A. K. Geim, Unconventional quantum Hall effect and Berry/'s phase of 2[pi] in bilayer graphene. *Nat Phys* **2**, 177-180 (2006); published online Epub03//print (http://www.nature.com/nphys/journal/v2/n3/suppinfo/nphys245_S1.html).
11. M. I. Katsnelson, K. S. Novoselov, A. K. Geim, Chiral tunnelling and the Klein paradox in graphene. *Nat Phys* **2**, 620-625 (2006); published online Epub09//print (http://www.nature.com/nphys/journal/v2/n9/suppinfo/nphys384_S1.html).
12. A. F. Young, P. Kim, Quantum interference and Klein tunnelling in graphene heterojunctions. *Nat Phys* **5**, 222-226 (2009); published online Epub03//print (http://www.nature.com/nphys/journal/v5/n3/suppinfo/nphys1198_S1.html).
13. A. K. Geim, K. S. Novoselov, The rise of graphene. *Nat Mater* **6**, 183-191 (2007); published online Epub03//print (
14. S. Das Sarma, S. Adam, E. H. Hwang, E. Rossi, Electronic transport in two-dimensional graphene. *Reviews of Modern Physics* **83**, 407-470 (2011); published online Epub05/16/ (
15. Q. H. Wang, K. Kalantar-Zadeh, A. Kis, J. N. Coleman, M. S. Strano, Electronics and optoelectronics of two-dimensional transition metal dichalcogenides. *Nat Nano* **7**, 699-712 (2012); published online Epub11//print (
16. G. Fiori, F. Bonaccorso, G. Iannaccone, T. Palacios, D. Neumaier, A. Seabaugh, S. K. Banerjee, L. Colombo, Electronics based on two-dimensional materials. *Nat Nano* **9**, 768-779 (2014)10.1038/nnano.2014.207).
17. S. Das, H.-Y. Chen, A. V. Penumatcha, J. Appenzeller, High Performance Multilayer MoS2 Transistors with Scandium Contacts. *Nano Letters* **13**, 100-105 (2012); published online Epub2013/01/09 (10.1021/nl303583v).
18. X. Cui, G.-H. Lee, Y. D. Kim, G. Arefe, P. Y. Huang, C.-H. Lee, D. A. Chenet, X. Zhang, L. Wang, F. Ye, F. Pizzocchero, B. S. Jessen, K. Watanabe, T. Taniguchi, D. A. Muller, T. Low, P. Kim, J. Hone, Multi-terminal transport measurements of MoS2 using a van der Waals heterostructure device platform. *Nat Nano* **advance online publication**, (2015); published online Epub04/27/online (10.1038/nnano.2015.70
http://www.nature.com/nnano/journal/vaop/ncurrent/abs/nnano.2015.70.html#supplementary-information).
19. A. K. Geim, Graphene: Status and Prospects. *Science* **324**, 1530-1534 (2009); published online EpubJune 19, 2009 (10.1126/science.1158877).
20. F. Schwierz, Graphene transistors. *Nat Nano* **5**, 487-496 (2010).

21. S. Z. Butler, S. M. Hollen, L. Cao, Y. Cui, J. A. Gupta, H. R. Gutiérrez, T. F. Heinz, S. S. Hong, J. Huang, A. F. Ismach, E. Johnston-Halperin, M. Kuno, V. V. Plashnitsa, R. D. Robinson, R. S. Ruoff, S. Salahuddin, J. Shan, L. Shi, M. G. Spencer, M. Terrones, W. Windl, J. E. Goldberger, Progress, Challenges, and Opportunities in Two-Dimensional Materials Beyond Graphene. *ACS Nano* **7**, 2898-2926 (2013); published online Epub2013/04/23 (10.1021/nn400280c).
22. S. Tongay, J. Zhou, C. Ataca, K. Lo, T. S. Matthews, J. Li, J. C. Grossman, J. Wu, Thermally Driven Crossover from Indirect toward Direct Bandgap in 2D Semiconductors: MoSe2 versus MoS2. *Nano Letters* **12**, 5576-5580 (2012); published online Epub2012/11/14 (10.1021/nl302584w).
23. H. Zeng, J. Dai, W. Yao, D. Xiao, X. Cui, Valley polarization in MoS2 monolayers by optical pumping. *Nat Nano* **7**, 490-493 (2012)http://www.nature.com/nnano/journal/v7/n8/abs/nnano.2012.95.html#supplementary-information).
24. SuzukiR, SakanoM, Y. J. Zhang, AkashiR, MorikawaD, HarasawaA, YajiK, KurodaK, MiyamotoK, OkudaT, IshizakaK, AritaR, IwasaY, Valley-dependent spin polarization in bulk MoS2 with broken inversion symmetry. *Nat Nano* **9**, 611-617 (2014)10.1038/nnano.2014.148
http://www.nature.com/nnano/journal/v9/n8/abs/nnano.2014.148.html#supplementary-information).
25. X. Xu, W. Yao, D. Xiao, T. F. Heinz, Spin and pseudospins in layered transition metal dichalcogenides. *Nat Phys* **10**, 343-350 (2014); published online Epub05//print (10.1038/nphys2942).
26. X. Qian, J. Liu, L. Fu, J. Li, Quantum spin Hall effect in two-dimensional transition metal dichalcogenides. *Science* **346**, 1344-1347 (2014); published online EpubDecember 12, 2014 (10.1126/science.1256815).
27. L. Ju, Z. Shi, N. Nair, Y. Lv, C. Jin, J. Velasco Jr, C. Ojeda-Aristizabal, H. A. Bechtel, M. C. Martin, A. Zettl, J. Analytis, F. Wang, Topological valley transport at bilayer graphene domain walls. *Nature* **520**, 650-655 (2015); published online Epub04/30/print (10.1038/nature14364).
28. A. F. Young, J. D. Sanchez-Yamagishi, B. Hunt, S. H. Choi, K. Watanabe, T. Taniguchi, R. C. Ashoori, P. Jarillo-Herrero, Tunable symmetry breaking and helical edge transport in a graphene quantum spin Hall state. *Nature* **505**, 528-532 (2014); published online Epub01/23/print (10.1038/nature12800).
29. R. Kappera, D. Voiry, S. E. Yalcin, B. Branch, G. Gupta, A. D. Mohite, M. Chhowalla, Phase-engineered low-resistance contacts for ultrathin MoS2 transistors. *Nat Mater* **13**, 1128-1134 (2014); published online Epub12//print (10.1038/nmat4080
http://www.nature.com/nmat/journal/v13/n12/abs/nmat4080.html#supplementary-information).
30. Y. Xu, I. Miotkowski, C. Liu, J. Tian, H. Nam, N. Alidoust, J. Hu, C.-K. Shih, M. Z. Hasan, Y. P. Chen, Observation of topological surface state quantum Hall effect in an intrinsic three-dimensional topological insulator. *Nat Phys* **10**, 956-963 (2014); published online Epub12//print (10.1038/nphys3140
http://www.nature.com/nphys/journal/v10/n12/abs/nphys3140.html#supplementary-information).

Appendix A

Fourier transform technique to extract each interference component along two different combinations of gate voltages

Fourier analysis technique is a useful tool to analyze signals arising from mixing components of different contribution. We use this general concept to analyze our measured complex interference patterns which have different gate dependency upon top-gate voltage (Vtg) and back-gate voltage (Vbg)(*1*). According to our physical design of double gate bilayer graphene device structure, there are two spatial regions which is affected by different combination of top-gate voltage and back-gate voltage.

For example, carrier density in graphene lead region is controlled almost entirely by back-gate voltage, and not by top-gate voltage. In contrast, carrier density under the top-gated region is tuned by both top-gate, and back-gate voltage through capacitive coupling such that: n_{GL} = aVbg, n_{TG} = aVbg + a'Vtg, where a, and a' are capacitive coupling coefficients.

The conductance G = G(Vtg, Vbg), which is a linear sum of two unknown functions.

$$G = f_1(\vec{n}_1 \cdot \vec{v}) + f_2(\vec{n}_2 \cdot \vec{v}) \qquad \text{Equation A-1}$$

where $\vec{v} = (Vtg, Vbg)$ is a two-dimensional vector in Vtg, and Vbg coordinate. Two individual functions, f_1 and f_2 are both scalar function which depends upon different two combinations of two gate voltages along each direction, $\vec{n}_1$, and $\vec{n}_2$.

By taking the Fourier transform of the first term,

$$\tilde{G}_1 = \int d^2\,\vec{v} f_1(\vec{n}_1 \cdot \vec{v}) e^{-i\tilde{k}\cdot\tilde{v}} \qquad \text{Equation A-2}$$

This integral gives us the decomposition of the function f into its constituent frequency k. And the $f_1(\vec{n}_1 \cdot \vec{v})$ can be separated into two components that are parallel $v_{\parallel}^1$, and $v_{\perp}^1$ perpendicular to the direction $\vec{n}_1$

$$\tilde{G}_1 = \int d^2\,\vec{v} f_1(\vec{n}_1 \cdot \vec{v}) e^{-i\tilde{k}\cdot\tilde{v}} = \int dv_{\parallel}^1 dv_{\perp}^1 f_1\left(|n_1| v_{\parallel}^1\right) e^{-i\tilde{k}_{\parallel}\cdot\tilde{v}_{\parallel} - i\tilde{k}_{\perp}\cdot\tilde{v}_{\perp}}$$

Equation A-3

The integral isolates the component of f_1 along only$\vec{n}_1$, by yielding a delta function of the perpendicular component of k.

$$\tilde{G}_1 = \tilde{f}_1\left(\frac{|k_{\parallel}^1|}{|n_1|}\right) 2\pi\delta^{(1)}(\tilde{k}_{\perp} \cdot \tilde{v}_{\perp}) \qquad \text{Equation A- 4}$$

where $\tilde{f}_1$ is a the Fourier transform of f_1. Using the linearity of the Fourier transform property, we can add two contributions of conductance to obtain the Fourier transform of G

$$\tilde{G} = \tilde{f}_1\left(\frac{|k_{\parallel}^1|}{|n_1|}\right) 2\pi\delta^{(1)}\left(\tilde{k}_{\perp}^1 \cdot \tilde{v}_{\perp}^1\right) + \tilde{f}_2\left(\frac{|k_{\parallel}^2|}{|n_2|}\right) 2\pi\delta^{(1)}(\tilde{k}_{\perp}^2 \cdot \tilde{v}_{\perp}^2) \qquad \text{Equation A- 5}$$

where f_1, and f_2, correspond to two different conductance component. Two terms are two different streaks (one along $\vec{n}_1$, the other along $\vec{n}_2$) in Fourier space in different directions, which can be separately masked and analyzed to extract individual contribution of f_1, and f_2.

Using Matlab code, we apply this Fourier analysis technique to mask either the diagonal streak, or horizontal streak.

Appendix B

Line shapes of Coulomb oscillation

There are two different temperature regimes in Coulomb blockade (*2*).

(i) $\Delta E << k_B T << e^2/C$, the *classical or metallic Coulomb blockade regime*, where many excited levels are existed by thermal fluctuation.

(ii) $k_B T << \Delta E << e^2/C$, *quantum Coulomb blockade regime,* where only one or a few levels are excited in transport.

where k_B is the Boltzmann's constant, T is the temperature.

In the high temperature, $e^2/C << k_B T$, the conductance oscillation behavior is not observed. And the conductance is determined by Ohmic sum of the two barrier conductances and channel conductance. $1/G = 1/G_{left} + 1/G_{right} + 1/G_{channel}$.

The line-shape of the coulomb-blockade oscillations can be fitted to the conductance expression:

In the quantum Coulomb blockade regime,

$$\frac{G}{Gmax} = cosh^{-2}\left(\frac{ea|V-V_{peak}|}{2k_B T}\right) \qquad \text{Equation B- 1}$$

And in the classical or metallic Coulomb blockade regime.

$$\frac{G}{Gmax} = cosh^{-2}\left(\frac{ea|V-V_{peak}|}{2.5k_B T}\right) \qquad \text{Equation B- 2}$$

Where $\alpha = C_g/C_\Sigma$ is determined from the slopes of Coulomb diamonds, V_{peak} is the back-gate voltage at resonance peak.

References

1. N. M. Gabor, J. C. W. Song, Q. Ma, N. L. Nair, T. Taychatanapat, K. Watanabe, T. Taniguchi, L. S. Levitov, P. Jarillo-Herrero, Hot Carrier–Assisted Intrinsic Photoresponse in Graphene. *Science* **334**, 648-652 (2011); published online EpubNovember 4, 2011 (10.1126/science.1211384).
2. C. W. J. Beenakker, Theory of Coulomb-blockade oscillations in the conductance of a quantum dot. *Physical Review B* **44**, 1646-1656 (1991); published online Epub07/15/